Integrated Transportation Monitoring System for Both Pavement and Traffic

Wenjing Xue

Dissertation submitted to the faculty of the Virginia Polytechnic Institute and State University in partial fulfillment of the requirements for the degree of

Doctor of Philosophy
in
Civil Engineering

Linbing Wang, Chair
Gerardo W Flintsch
Surot Thangjitham
Anbo Wang

April 22, 2013
Blacksburg, VA

Keywords: Pavement Monitoring, Traffic Monitoring, Weigh-In-Motion, Traffic Classification, Pavement Health Status.

Integrated Transportation Monitoring System for Pavement and Traffic

Wenjing Xue

ABSTRACT

In the passing decades, the monitoring of pavements and passing vehicles was developed vigorously with the growth of information and sensing technology. Pavement monitoring is an essential part of pavement research and plays an important role in transportation system. At the same time, the monitoring system about the traffic, such as Weigh-in-Motion (WIM) system and traffic classification system, also attracted lots of attention because of their importance in traffic statistics and management.

The monitoring system in this dissertation combines the monitoring for pavements and traffic together with the same sensing network. For pavement health monitoring purpose, the modulus of the asphalt layer can be back-calculated based on the collected mechanical responses under corresponding environmental conditions. At the same time, the actually strain and stress in pavements induced by each passing vehicle are also used for pavement distress prediction. For traffic monitoring purpose, the horizontal strain traces are analyzed with a Gaussian model to estimate the speed, wandering position, weight and classification of each passing vehicle. The whole system, including the sensing network and corresponding analysis method, can monitor the pavement and the traffic simultaneously, and is called transportation monitoring system. This system has a high efficiency because of its low cost and easy installation; multi-functionality to provide many important information of transportation system.

Many related studies were made to improve the prototyped transportation monitoring system. With the assistance of numerical simulation software ABAQUS and 3D-Move, the effect of many loading and environmental conditions, including temperature, vehicle speed, tire configuration and inflation pressure, are taken into consideration. A method was set up to integrate data points from many tests of similar environmental and loading conditions based on Gaussian model. Another method for consistent comparison of variable field sensor data was developed. It was demonstrated that variation in field measurement was due to uncontrollable environmental and loading factors, which may be accounted for by using laboratory test and numerical simulation based corrections.

ACKNOWLEDGEMENT

The author would like to thank her family for all the devotions they made during this research. The author would like to thank all her friends for their support and friendship during her study in Blacksburg.

The author would like to thank Prof. Linbing Wang, Prof. Gerardo Flintsch, Prof. Surot Thangjitham, and Prof. Anbo Wang for serving on the thesis committee. The author appreciates the advice and direction they offered in regards to both her research and future career endeavors. The author would like to thank all of the scholars and staffs in Virginia Tech Transportation Institution, Civil and Environmental Engineering Department for the help and support. The author would like to thank VDOT for the support on experiments and information collection.

The support to this work by Eisenhower Scholarship and MAUTC is gratefully acknowledged. The author would like to thank all the colleagues in Turner-Fairbank Highway Research Center for their hospitality during her guest visit there. Especially, the author would like to thank Eric Weaver for the tremendous help and support, and his instruction and guidance not only account for a major part of the work, but also fuel the author's interest in pavement engineering.

Finally, the author would like to thank Prof. Linbing Wang for providing her the opportunity to pursue this research full-time. Prof. Linbing Wang has been the author's Ph.D. advisor for five years, and he supports and guides the author's research and makes this work possible.

TABLE OF CONTENTS

List of Figures

List of Tables

INTRODUCTION

The importance of transportation system for economy and society is self-evident. In the past half century, tremendous efforts of worldwide scholars have been devoted for a socialized, intelligent, and durable transportation system.

This dissertation presents the effort devoted on a novel transportation monitoring system, which can monitor the traffic flow and infrastructure simultaneously and speed up the process of intelligent transportation system

Background

In 2009, a project named "Integrated Infrastructure Asset Monitoring, Assessment and Management" was initiated, which was a collaborative effort of the University of Virginia, Center for Transportation Studies, Virginia Tech and the Virginia Transportation Research Council.

This collaborative project would investigate the feasibility and potential benefits of the integration of pavement and bridge infrastructure monitoring systems into enterprise-scale transportation management system. A framework would be developed for the integration of project-level data into the distributed network-level traffic operation and asset management system. This project would also investigate how the monitoring information can be used to supplement, enhance and augment existing data collection activities and recommend how to use the enhanced information to support and improve VDOT's enterprise asset management business processes.

The philosophy that underlay the research methodology was for the research partners to prototype advanced monitoring systems, and then utilize the knowledge gained to investigate integration opportunities and benefits. In the cooperation, Virginia Tech would develop a prototype pavement monitoring system. The research planned to accomplish the objectives consisted of five tasks, each of which is described below.

1. Pavement Monitoring System Design

There were various sensing devices that could be used for monitoring the pavement responses including stresses, strains, moisture condition and temperature. It was important to choose suitable sensors to make sure that the whole system worked compatible and efficiently.

2. Pavement Monitoring System Deployment

Installation of the sensors in a real road wa crucial to the whole project, including traffic control and proper bonding the sensors to the hosting asphalt concrete.

3. Data Collection and Analysis

a. Structural health monitoring data analysis

Data processing and analysis consisted primarily of filtering, quality control, summarization, alarm routine reporting and archiving.

b. Weather and environmental data analysis

The weather data collected in the study would be used to supplement the existing RWIS data that is currently collected and archived by VDOT and Smart Travel Laboratory. The

micro-climate data would be used for statistical summaries which might be useful for deterioration models

c. WIM data analysis

SHM data would be configured and adapted to support WIM application. There were several approaches that could be taken including an adaptation of the system developed under the Weighing-in-Motion of Axels and Vehicles (WAVE) project completed in Europe or the further development of a specialized system based upon the application of artificial Neural Networks (ANN) as funded under the NCHRP IDEA Program. The objective was to detect, weigh and classify heavy vehicle and provide statistical summary.

d. Pavement data analysis

Data processing, analysis, reduction and interpretation were very important in making use of the monitored data including strains, stresses, moisture content and temperature. As asphalt concrete is a viscoelastic material at regular temperature and loading condition, the back calculation of various parameters would be feasible with a viscoelastic analysis of the pavement response. In addition to direct observations of strain concentrations of cracking and rutting, modulus and other parameters could be also calculated. These data might be used for performance predictions, model calibrations, MEPDG calibration, and optimal repairing and rehabilitation decision making.

Problem Statement

All the research in transportation can be categorized into two parts, operation system part (software) and infrastructure (hardware). Operation system targets at controlling traffic flows effectively and intelligently and infrastructure part targets at building up durable transportation infrastructures with good performance. Monitoring is necessary for both operation and infrastructure parts. For operation system, it is necessary to monitor the traffic flow of the count, speed, classification throughout the whole transportation network. For infrastructure, the distribution of mechanical response (stress and strain) in pavements is important for distress prediction and pavement management.

Recently, many monitoring and management systems have already been introduced. However, these systems have been developed and deployed to support specific elements of the transportation infrastructure, such as traffic control, bridge monitoring and management. The premise of this research is that there will be significant advantages that may be realized by the integration of transportation monitoring and management systems.

Objective

The objective of this dissertation is to develop a transportation monitoring system, which combines the monitoring for pavements and traffic together with the same sensing network. The health status of the pavement can be evaluated and future performance can be predicted for pavement health monitoring purpose. Various information of the traffic flow, including the speed, wandering position, weight and classification of each passing vehicle can be estimated for traffic monitoring purpose.

This monitoring system can monitor the traffic and the pavement simultaneously, and serve as an important part of transportation management system. The methodology of integrating different monitoring system together can be used for other comprehensive monitoring system.

Overview of the dissertation

Both the traffic monitoring and infrastructure monitoring have attracted lots of research interests in the recent decades. The research history of various monitoring systems in transportation system is reviewed in the chapter "Literature Review", common methods and techniques are discussed and compared, and the future trend of monitoring system for transportation is predicted.

To achieve a comprehensive monitoring system for both pavements and traffic, it is necessary to analyze the mechanical response distribution in pavements thoroughly before making good use of it. Two experiments were involved in this dissertation, as described in the chapter "Experiments". Data from Ohio SPS-8 experiment (1997) was used in this research for the strain response analysis, and Virginia Route 114 experiment (2011) was designed as a transportation monitoring system as proposed in this dissertation. These two experiments used different sensing devices, network design, and testing methodologies because of their different research purposes.

Based on the sensing network instrumented on Virginia Route 114, a pavement monitoring system was developed to track the health status of the pavement section. Various pavement response signals were checked for signal quality, and the sensors

which were broken during the installation or by excessive traffic load, could be found and excluded from the further analysis. Strain and stress responses obtained from different positions of the section were compared on magnitude and trend. The instrumented pavement section was modeled numerically with the Finite Element Method (FEM) based software ABAQUS, and the simulated strain response distribution was proved to be close to the field measurement on both trend and magnitude. Then ABAQUS simulation was used to derive the relationship between the current modulus and the ratio between stress and strain, which could be used for pavement modulus back-calculation. The MEPDG fatigue cracking and rutting models were modified, and the damage caused by each single pass could be calculated based on measured strain and stress and cumulated for pavement distresses prediction. A frame of pavement health monitoring system was set up based on the module of pavement modulus back-calculation and the module of pavement distresses prediction.

A traffic monitoring system was also developed based on the same sensing network on Virginia Route 114. This traffic monitoring system was designed to back-calculate the speed, configurations and weight of the passed vehicle and count traffic volume in real-time monitoring. The target of data analysis can be divided into temporal and spatial distribution based on the field of the collected data sets. Temporal distribution analysis focused on the pavement responses distribution in time domain, based on which traffic volume, number of axles, speed and distance between axles could be calculated. Spatial distribution analysis used the longitudinal strain distribution in the transverse plane of the pavement to calculate wandering position, distance between wheels, width of tire and

weight of the passed vehicle. A new Gaussian model was built up to describe the distribution of longitudinal strain response in the transverse plane of the pavement. The model can characterize the distribution of strain response accurately, and the parameters of this model represent important parameters of the loading condition which can be used to back-calculate the passing vehicles. The whole traffic monitoring system combined temporal and spatial analysis together and functions for traffic flow statistics, traffic classification, and weigh-in-motion purposes simultaneously.

The prototype of the transportation monitoring system was based on the basic and simplest condition: constant temperature, fixed speed, circular contact area and fixed pressure between tire and pavement. However, in the actual practice of the monitoring system, the environmental and loading conditions were changing all the time, and might induced various effects on the collected responses. The effects of temperature, vehicle's speed, tire configuration and inflation pressure were studied in this dissertation.

Asphalt concrete is usually treated as viscoelastic material because the dependence of its mechanical properties on temperature and loading rate. The effect of temperature and vehicle's speed on pavement responses is discussed in the chapter "Effect of Temperature and Speed". Linear viscoelasticity theory is introduced as the basic principle. Numerical simulations in ABAQUS were made with different temperature and passing velocity for comparison and analysis. The collected strain data points in the 3 testing runs with same temperature and speed were integrated together based on their back-calculated offset distance to form a whole distribution curve with more data points. The simulated and collected strain responses both followed the same trend with increasing magnitude when

temperature increased or vehicle's speed decreased. The Gaussian model was used to analyze the strain response distribution and the simulated parameters $\sum L$ and σ present certain linear relationships with temperature and speed in experiment outputs, but not as clear or obvious as in numerical simulation.

The effect of tire configuration and inflation pressure, which is important for the distribution of mechanical response in pavement, is discussed in the chapter "Effect of Tire Configuration and Inflation Pressure". Lots of environmental and loading conditions in the field experiments were uncontrollable, such as pavement temperature, offset distance, test vehicle speed and so on. It was demonstrated that these factors were responsible for the variation in field measurement, and may be accounted for by using laboratory tests and numerical analysis based corrections. A method for consistent comparison of variable field sensor data was developed to adjust the strain measurements to a universal temperature, zero offset distance and standard speed. The original and adjusted strain responses induced by tires of different configurations and inflation pressures were compared and analyzed to reveal the damage brought by different tires to pavements. It was important to choose road-friendly design of tires and adjust tire inflation pressure from the perspective of tire protection and pavement protection.

As introduced above, an integrated transportation monitoring system is described in this dissertation. This system can trace the health status of pavement and estimate various parameters of passed vehicles simultaneously based on the same instrumented sensing network. The sensors groups for different monitoring purposes were integrated together for the system's multiple functions. The design of the whole system is efficient with great

potential and value for the intelligent transportation system and socialized infrastructure management in future.

LITERATURE REVIEW

Pavement Management System (PMS) is a broad concept, and its strategies and decisions are based on various observations and measurements of the pavement. The accurate measurement of the strain and stress distributions in pavement is critical for understanding pavement behavior and modeling failures of pavements. As an essential part of pavement management, pavement health monitoring is critical to the socialized and integrated transportation system, and was improved via various advanced technologies and methodologies in the past decades.

The monitoring of pavement condition can be conducted by visual investigation, and various testing methods. Most of these methods can be used on any pavement interested, having the advantages of spatial flexibility. In contrast, monitoring systems with sensing devices installed in pavement has also been heavily investigated to achieve real-time monitoring, which has frequency superiority of pavement monitoring. The studies discussed in this dissertation only focuses on the in-situ pavement monitoring sensors, which are installed in pavements.

In-Situ Pavement Monitoring Sensors

Tremendous efforts have been devoted to in-situ monitoring by governments and transportation agencies around the world. After several decades' research and application, a wide variety of sensors has been developed for in-situ pavement monitoring, and most

of the sensors can be classified into two categories: electromagnetic sensor and optical fiber sensor.

Electrical Sensors

All the sensors that convert a physical parameter to an electrical signal are classified into this category. Devices Transducer in electrical sensors is used to convert the mechanical, thermal and other form of energy in pavements to electrical energy.

The application of electromagnetic sensors in pavement monitoring can be traced back to the 1960s[1]. In 1991, Sebaaly et al.[2] tested various types of pavement instrumentation, including pressure cell, deflectometer, strain gauge, thermocouple, moisture sensor, and transverse vehicle location sensor, for field evaluation under actual truck loading. In 1995, Sebaaly et al.[3] measured the tensile strains in flexible pavement using the Hall Effect sensor in an H-gage configuration. In 2001, commercial diaphragm-type stress cells were embedded in subgrade to compare the performance of two instrumented pavement test sections under linear traffic simulator[4]. In 2005, Huff et al.[5] investigated piezoelectric axle sensors to obtain dynamic pavement deflection data. In 2011, Xue and Weaver [6] explored the effect of wide-base tire on pavement strain response based on the data collected from SPS-8 on Ohio-SHRP U.S. 23 Test Road in 1997. In the same year, a novel self-powered wireless sensor was developed based on the integration of piezoelectric transduction with floating-gate injection, which is also capable of detecting strain and temperature simultaneously [7].

Optical Fiber Sensors

Fiber optics sensors have attracted lots of efforts in civil engineering infrastructure monitoring because of several of its positive attributes, including distributed sensing capabilities, small diameter, light weight, immunity to electromagnetic interference, strong survival ability and high sensitivity[8, 9].

In 1994, Navarrete and Bernabeu[10] described an interferometry system, which can detect changes in pressure on fiber and measure another external stimulus and changes simultaneously. In 1995, Signore and Roesler [11] used fiber-optic sensors to study the lateral strain behavior of axially loaded emulsified asphalt specimen and obtained its Poisson ratio. In 1996, polymide multimode fiber was braided for increased sensitivity. In 2005, Wang and Tang[12] developed a new high-resolution fiber Bragg grating (FBG) sensor consisting of a referenced FBG and a pair of fiber gratings, and provided the potential of simultaneous measurement of strain and temperature within pavements. Due to the increasing interest of the response and performance in the whole structure, 3-dimensional monitoring has gained more and more attention. In 2012, Zhou et. al set up a 3D optical fiber grating based sensor assembly [13].

Pavement Monitoring System

For better understanding of pavement, various pavement research facilities (test roads) have become an integral of pavement research and engineering, and the foremost was the AASHO Road Test conducted in Ottowa, Illinois from 1958 to 1960[14].As early as in 1989, Rollings and Pittman presented the result of instrumental model tests and full-scale traffic test on rigid pavement, which matched the Westergaard edge-loaded analytical

model well on design stresses[15]. In 2004, eight sections were fully instrumented to measure in situ pavement responses under load at the NCAT test track[14]. Timm et al.[16] presented the data collection and processing procedures for the NCAT test track instrumentation. MnROAD in Minnesota was heavily instrumented with 40 test cells; based on the monitored data Lukanen developed mechanistically based load equivalency factors (LEF) in 2005[17]. The Virginia Smart Road is another outdoor pavement research facility located in Blacksburg of Virginia, which has twelve instrumented sections [18]. In 2006, Loulizi et al. [19] used one section of the Virginia Smart Road to compare measured stress and strain, and obtained the difference between the stresses and strains measured in situ and calculated for a flexible pavement section.

Integrated Monitoring System

With the development of information technology and digitization, traditional pavement monitoring systems have been integrated with other monitoring systems, including bridge monitoring, Weigh-in-Motion (WIM), traffic classification and so on. Both electromagnetic and optical fiber optic sensors have been widely studied and used in various integrated pavement monitoring systems.

Bridge Monitoring

Many bridges worldwide are closely monitored because of their economic importance and vulnerability to extreme loading and harsh environmental conditions[4]. The monitoring of bridges is convenient to be integrated with pavement monitoring because of their similarity in structure and function. The monitoring system of Geumdang Bridge

in Korea using high-resolution wireless sensors are combined together with the two-lane passing test road which employed 1897 sensors to evaluate three types of pavement constructed along the road length[20]. In Hong Kong, the integrated monitoring system with more than 800 sensors permanently installed on the three long-span cable-supported bridges- the suspension Tsing Ma Bridge, the cable-stayed Kap Shui Mun Bridge, and the Ting Kau Bridge[21]. In United States, the Commodore Barry Bridge is instrumented using 77 sensors and 115 channels to track the loading environment and structural responses, and expected to be integrated with a WIM system in the future[22]. In 2012, Kim and Lynch[23] installed wireless sensors on both the bridge and moving vehicle and record the dynamic interaction between the bridge and vehicle.

WIM System

Weigh-in-Motion (WIM) is to obtain the static weight of a vehicle while the vehicle is in motion. Since the concept was brought up sixty years ago[24], WIM technologies have been used increasingly around the world for weight control of heavy vehicles, the protection and management of pavement and other infrastructures[25]. For example, there are more than 100 Weigh-in-Motion stations throughout California by 2002 [26]. Today there are several major types of sensors used for WIM stations: piezoelectric sensors, capacitive mats, bending plate, load cell and optic fiber[25, 27]. The original highway WIM system[28] used weighing devices in one lane of the road. As early as 1989[29], a high speed Weigh-in-Motion system which was manufactured and supplied by International Road Dynamics (IRD), was installed on Highway 1 near Regina of Canada.

During the past twenty years, each kind of WIM station has been widely studied and developed by worldwide scholars and transportation agencies. Due to the distributed sensing properties, high environment resistance, and other advantages, the studies and applications of optic fiber sensors in WIM systems increased significantly in the past 10 years [8, 30-33]. In 2007, Cheng et al.[34] presented the design of a new capacitive flexible weighing sensor for a vehicle WIM system. In the same year, Zhang et al[35] investigated a novel WIM system based on multiple low cost, light weight, small volume and high accuracy embedded concrete strain sensors.

Traffic Classification

Vehicle classification is another important category of traffic data collection. The study of vehicle classification can be traced back to 1976[36], and commercial detector equipment was used to measure some configuration parameters of a passing vehicle with rough estimation. As of today, lots of information and sensing technology have been devoted to improving the classification. Vehicle classification technologies in current use can be grouped into three major categories: axle based, vehicle length based, and machine vision (visual) based[37]. In recent years, the most popular sensing technologies used in vehicle detecting are piezoelectric sensor, inductive loops, and fiber optic sensors. Piezoelectric sensor is the most widely instrumented, and a lot of experience has been accumulated. In 1990s, cheaper inductive loops (usually single loop or dual loop detectors) were developed to replace the expensive piezoelectric sensors with high classification efficiency preserved [38-42]. Fiber grating sensor application in traffic classification increases because of its advantages and its wide application in pavement

health monitoring and Weigh-in-Motion system. Efforts of scholars throughout the world are devoted to improving its performance in vehicle classification [43-46]. At the same time, some other researchers devoted efforts to making use of traditional sensors for health monitoring to detect and classify vehicles. In 2008, Zhang et al.[47] delivered a new vehicle classification method and developed a traffic monitoring detector with embedded concrete strain gauges.

Traffic Data Collection

WIM systems and vehicle classification system mentioned above, together with vehicle speed measurement, are all parts of traffic data collection. "Truck data collection and reporting is an important program that state departments of transportation (DOTs) must maintain to comply with FHWA requirements"[37]. For example, the Florida Department of Transportation (FDOT) has approximately 350 traffic classification and WIM sites located throughout the state, including thousands of piezoelectric sensors [48]. Due to the low survival rate of piezoelectric sensors, FDOT was committed to the development of optical fiber sensors in traffic classification and WIM system because of its flexibility, corrosion resistance and immunity to electromagnetic interference[49]; in this project, Cosentino and Grossma developed a fiber optic traffic sensor (FOTS) in 1996[50]; they improved its sensitivity, validated its application in both flexible and rigid pavements, and exploreed its WIM accuracy in 1997[51]; finally they deployed the designed fiber optic traffic sensor in monitoring system for traffic classification and WIM system in 2000[52]. Since June 2008, an in situ measuring station has been used in Lenzburg, Switzerland[53]. This measuring station includes Weigh-in-Motion sensors, Stress-in-

Motion sensors, temperature sensors and acceleration sensors, and serves as a useful tool for both the statistical assessment of traffic and the loading condition of the pavement.

Summary

As a summary of the review, the described developments of in situ pavement monitoring systems, and other monitoring systems which can be integrated with pavement monitoring system are tabulated into Table 1 [54].

Table 1: Summary of recent development in monitoring systems in/for pavement

Purpose of Monitoring System	Year	Authors / Infrastructure	Measurement	Sensing Type	Sensor	Special Technology or Advantage
Pavement Health Status	1946[15]	Rollings and Pittman	Strain	EM	Strain gage	Full-scale, accelerated traffic tests
	1991[2]	Sebaaly et al.	Stress; deflection; strain; temperature; moisture; vehicle location.	EM		
	1994[17]	MnRoad, Minnesota	Stress, strain, applied loading	EM	WIM devices, temperature, moisture, thermal strain sensors	Both rigid and flexible pavements
	1995[3]	Sebaaly et al	Strain	EM	Strain gage	Hall-effect gage
	1995[11]	Signore and Roesler	Strain	FO		Laboratory test
	1997[6]	US 23 Test Road, Ohio	Strain	EM	Strain gage	
	1998[18, 19]	The Virginia Smart Road, Virginia	Stress, strain, temperature, moisture, frost	EM	Pressure cell, strain gauges, thermocouple, reflectometry and resistivity	

			penetration		probes.	
	2001[55]	Goncalves et al.	Stress	EM	diaphragm-type stress cell	Full-scale, accelerated traffic tests
	2004[14, 16]	NCAT	Strain, stress, moisture and temperature	EM	Strain gage, pressure cell, moisture probes and thermistor	
	2005[5]	Huff et al.	Digitized current	EM	Piezoelectric axle sensor	
	2005[12]	Wang and Tang	Strain and temperature	FO	Fiber Bragg Grating Sensor	Measure strain and temperature simultaneously
	2011[7]	Lajnef et al.	Strain and temperature	EM	Piezoelectric transduction	Self-powered piezo-floating-gate array
	2012[13]	Tailai Highway, China	Strain	FO	OFBG	3D monitoring
Bridge Monitoring	2000[56]	Tsing Ma Bridge, Kap Shui Mun Bridge and Ting Kau Bridge, Hong Kong	Strain/stress, displacement, acceleration, temperature, wind, axle load	EM		Wind and Structural Health Monitoring System (WASHMS)
	2000[22]	Commodore Barry Bridge, New Jersey	Wind, strain and acceleration.	EM	strain gages, piezoelectric accelerometers and ultrasonic anemometer	
	2006 [57, 58]	Alamosa Canyon Bridge, New Mexico	Acceleration	EM		
	2006[20]	Geumdang Bridge, Korea	Acceleration	EM	piezoelectric and capacitive	Traditional tethered and wireless
	2012[23]	Yeondae Bridge, Korea	Acceleration and tactility	EM	capacitive accelerometer and piezoelectric tactile sensor	Vehicle-bridge interaction

WIM	1986[29]	Highway 1, Canada	Load, speed	EM	IRD-WIM-5000 system and radar	
	1994[10]	Navarret and Bernabeu	Pressure	FO		Mach-Zehnder interferometer
	2004[30]	Yuan et al.	Pressure	FO		Michelson interferometer
	2007[27]	Cheng et al.	Strain	EM	Capacitive sensor	Light weight, small volume and portability.
	2008[8]	Malla et al.	Load	FO		Two concentric light guiding regions
Vehicle Classification	2001[38]	Gajda et al.	Inductive voltage	EM	Inductive loop detector	Cheap
	2002[44-46]	Interstate 84 in Oregon	Amplitude of optical signal	FO		
	2003[41]	Interstate 710 in California	Traffic volume, vehicle length and speed	Em	Single inductive loop detector	
	2009[39]	I-70 and I-71, OHIO	Inductive voltage	EM	Single-loop, Dual-loop and Piezoelectric detector	
Integrated Monitoring	2000[49-52]	Cosentino and Grossman	WIM; vehicle classification	FO	Fiber optic traffic sensor (FOTS)	Microbend fiber-optic sensing technology
	1988[48]	Florida	WIM and vehicle classification	EM	Piezoelectric sensor, loop detector, and bending plate	More than 300 continuous monitoring sites
	2008[53]	A1 motorway, Switzerland	Vehicle weight, traffic classification, temperature, acceleration	EM	WIM, Stress-in-Motion, temperature and acceleration sensors	Footprint measuring station
	2008[35, 47]	Zhang et al.	WIM and vehicle classification	EM	strip strain sensor	Simple and efficient

EXPERIMENTS

Two experiments are involved in this dissertation: Ohio SPS-8 experiment in 1997 and Virginia Route 114 experiment in 2011. The data from Ohio experiment is for the analysis of strain distribution in pavements. Experiment in Virginia is designed as a comprehensive transportation monitoring system for the potential benefit of monitoring system combination.

Ohio SPS-8 Experiment

Background

In 1989 the FHWA conducted a study at the Accelerated Loading Facility (ALF) to compare flexible pavement damage induced by Goodyear 11R22.5 dual tires and the Goodyear 425/65R22.5 wide-base single tire. The study found that the single tire produced higher pavement, base and sub-grade strains, resulting in twice the rut depth and one quarter of the fatigue life induced by the dual tires [59]. Several studies since then have found similar results with respect to predicted and measured pavement damage for the earlier wide-base tire designs used in the FHWA study. However, for newer and wider tires, such as the 445 mm (17.5-in.) and 455 mm (17.9-in.), less of a difference in pavement response was seen; especially for thick pavements. However, even among the new wide-base tire designs, less pavement damage was predicted and measured with the widest tires available [60, 61].

At the 2006 meeting of the Technical Advisory Committee of Transportation Pooled Fund Study TPF-5(127) "Consortium of Accelerated Pavement Testing (CAPT) and Technical Exchange Partnership" a recommendation was made that an international workshop be conducted to exchange information on related research efforts regarding wide-base tires. So, in 2007, FHWA hosted the International Workshop on the Use of Wide-Base Tires in cooperation with the Asphalt Research Consortium [62] when this experiment was presented at the workshop.

In addition to the pavement response and performance aspects related to wide-base tires, several other beneficial aspects of new wide-base tire designs were discussed at the workshop. First, wide-base tires can save fuel by reducing the total weight of the truck, reducing rolling resistance and therefore reducing vehicle emissions as a result. Secondly, it is more convenient to check for proper inflation pressure with wide-base tires, which minimizes rolling resistance while maximizing tread life and safety [63]. For these reasons, the latest wide-base tires have been endorsed as part of the United States Environmental Protection Agency's Smartway Transport Partnership [64].

The outcome of the workshop was a recommendation that a study of National scope be conducted with international collaboration to examine pavement, environmental and economic aspects of wide-base tires. The study should build upon the work that has already been completed, and fill gaps not addressed by other efforts, such as pavement structure variation. Since then, the Illinois Department of Transportation initiated the Transportation Pooled Fund Study TPF-5(197) "The Impact of Wide-Base Tires on Pavement Damage: A National Study." This FHWA-led study intends to provide state

highway agencies a tool for evaluating the impacts of existing and emerging tires on their pavement networks. The data set generated from the experiment described in this paper may be an asset to the study efforts and goals.

The data presented in this paper was meant to validate the effect of tire configuration and inflation pressure on pavement strain responses. The analysis result could be taken into consideration in the back-calculation of the monitoring system in the future.

Pavement Section and Sensor Distribution

During the fall 1997, sections of the Ohio-SHRP U.S. 23 Test Road were placed. Provisions were made to instrument additional sections for further testing. Two sections on the SPS-8 experiment, including a four inch thick and a seven inch thick Asphalt Concrete (AC) sections, were chosen as shown in Figure 1. Two hundred feet of the seven inch AC section were modified to an eight inch thick section with uniform materials throughout the depth.

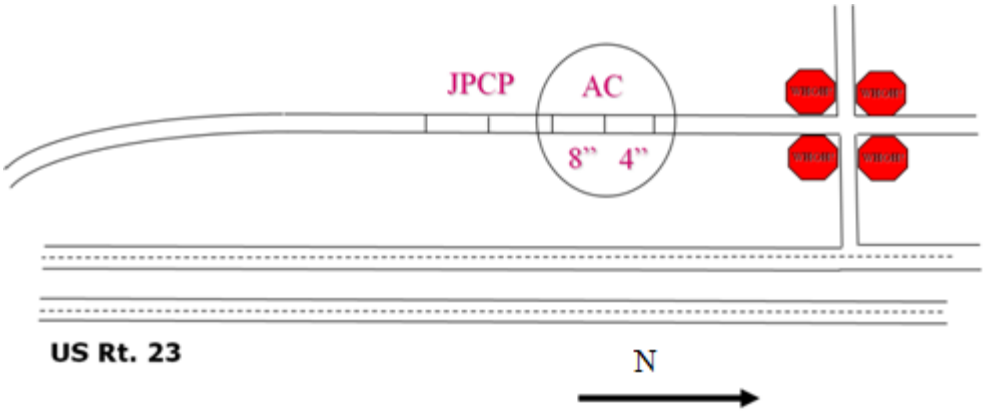

Figure 1: Plane View of the Experimental Sections of SPS-8

Controlled load test was performed on the four inch and eight inch AC sections of the SPS-8 replacement sections: sections 39A803 and 39A804. These sections were

constructed over six inches of dense graded aggregate base at the SPS-8 Ohio SHRP Test Road. During construction, several layers of Dynatest H-shaped gauges and Canadian Strain Gauges were placed, and after construction, strain gages Rossettes were retrofitted into 4-inch square holes cut through the AC surface layer, as shown in Figure 2. One set of Rossettes was placed 1-inch below the surface and another 1-inch above the bottom of the AC layer, both in the direction of, and transverse to, the direction of traffic. The detailed positions of Rossette are shown in Figure 3. The Rossettes were affixed to the existing pavement; not to the material removed from the hole.

In addition to the strain gauge instrumentation, cables were placed in the base at specific location for future use. Four inch square holes were created above the location of the buried wires, and strain gauge rosettes were attached to the side of the holes, as shown in Figure 3[6]. In addition to the strain gauges, thermocouples were placed in the pavement sections at 1 inch, 3 inch and 7 inch depths in this project.

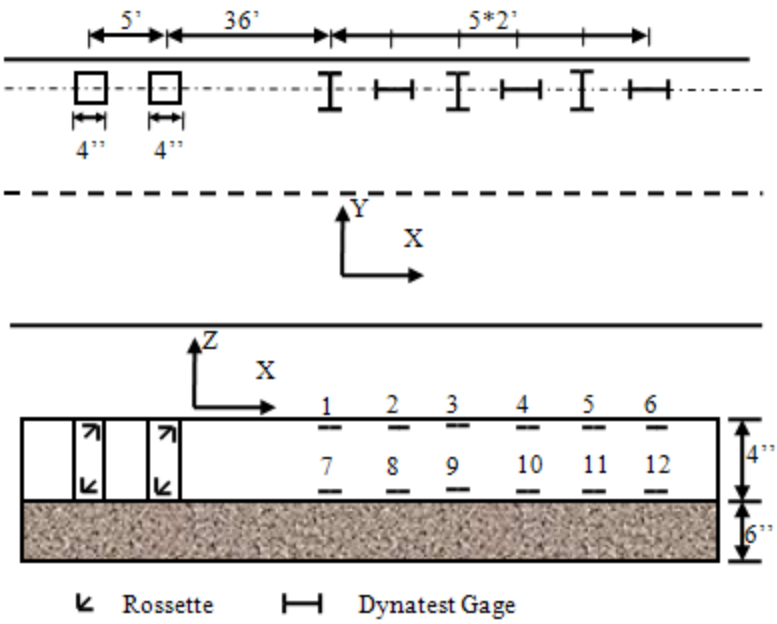

(a) 4 inch pavement

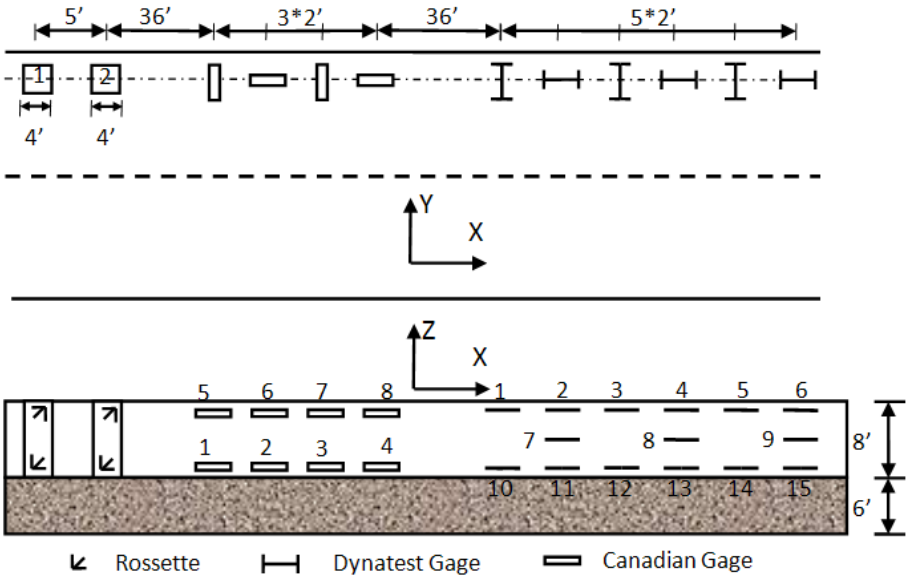

(b) 8 inch pavement

Figure 2: Pavement Sections and Sensor Distribution

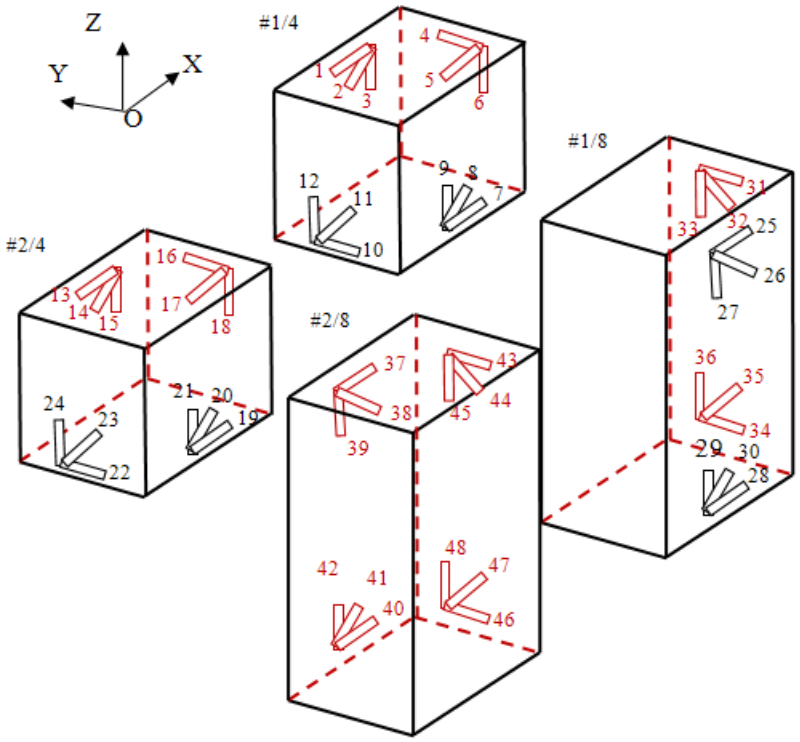

Figure 3: Positions of Rossettes

Traditionally, pavement strain gages were placed during construction and strains were measured only in the X-Y plane. In this study, the square holes where chosen to measure strains in the X-Z and Y-Z planes and to reduce orientation error. The rosettes are a two dimensional (2D) representation of strain behavior and they are defined as being on one of the X or Y planes. The direction of a single gage would be a single subscript X, Y or Z, for example, $\varepsilon_Y^{(X)}$, $\varepsilon_Z^{(X)}$, and $\varepsilon_X^{(Y)}$, $\varepsilon_Z^{(Y)}$. The normal strain in 45 degree orientation is defined with the plane as $\varepsilon_{45^\circ}^{(X)}$ and $\varepsilon_{45^\circ}^{(Y)}$. The shear strain at the 2D point in a X and Y plane is expressed as $\gamma^{(X)}$ and $\gamma^{(Y)}$. For instance, $\varepsilon_Y^{(X)}$ is the strain in the Y direction measured in the X-plane.

Test Truck and Tires

The truck used to conduct the load tests was the "Kenis Dynamic Test Truck", which was a single unit two axle truck instrumented with sensors to collect vehicle dynamics and road profile, as shown in Figure 4.

Figure 4: FHWA Heavy Vehicle Test Truck

Table 2: Geometry and Load Limits of Test Vehicle

Wheel Base	6.48 m (21.25 ft)
Wheel Track	2.05 m (6.71 ft)
Truck Length	10.00 m (32.83 ft)
Bed Length	7.39 m (24.25 ft)
Bed Width	2.44 m (8.0 ft)
Gross Vehicle Weight	150,677 N (33,680 lb)
Empty Weight	71,067 N (15,970 lb)
Manufacturer Allowable Load	79,611 N (17,890 lb)
DOT Allowable Load	50,018 N (14,890 lb)

Four different sets of tires were used in the experiment: two wide base tires and two sets of dual tires. FHWA supplied the M445 wide base tires and both G159 and M275 dual TIRES. Ohio University supplied the G286 wide base tires. Tire changes were conducted

on-site as necessary. Table 3shows the detailed profile information of the 4 kinds of test tires.

Table 3: Profile Information of Testing Tires

	Manufacture	Name	Type	Profile	Width of Tire		Width of Footprint	
					(mm)	(inch)	(mm)	(inch)
A	GoodYear	G286	Wide base	65R22.5	425	16.73	330	13.00
B	GoodYear	G159	Dual	75R22.5	295	11.61	222	8.75
C	Michelin	MXDA	Wide base	45R22.5	495	19.49	438	17.25
D	Michelin	MXZA	Dual	80R22.5	275	10.83	229	9.00

Tire Inflation Pressure = 120 psi

Data Collection

This experiment included three speeds, three tire inflation pressures, and two pavement thicknesses for each tire. Each test series was repeated at least three times or until three different tire prints around the gauges were achieved. For each tire, the test runs are summarized in Table 4.

Table 4: Test Runs Summary

Test Series	Speed (mph)	Tire Inflation Pressure (psi)	Pavement Section (inch)	Test Series	Speed (mph)	Tire Inflation Pressure (psi)	Pavement Section (inch)
1	5	70	4	10	5	70	8
2	25	70	4	11	25	70	8
3	55	70	4	12	55	70	8
4	5	100	4	13	5	100	8
5	25	100	4	14	25	100	8
6	55	100	4	15	55	100	8
7	5	120	4	16	5	120	8
8	25	120	4	17	25	120	8
9	55	120	4	18	55	120	8

During the dynamic loading tests, the truck was loaded with 19.25-kips (85.63-kN) for all test series, producing 9650 lbf (42.94-kN) for wide-base tire GoodYear G286 and Michelin MXDA, 4200 lbf (18.69-kN) for dual tire GoodYear G159 and 5050 lbf (22.47-kN) for dual tire Michelin MXZA. The timeline of the whole experiment process is listed in Table 5.

Table 5: Timeline of the Experiment

Task	7/19	7/20	7/21	7/22	7/23	7/24
	Sun.	Mon.	The.	Wed.	Thu.	Fri.
Travel / Arrival	xxxx					
Change tires from G159 to G286		xx				
Preliminary Profile and Dynamic Test		xxxx				
Truck strain gage cal.			xx			
Test G286 and collect Prof. and Dyn. data			xxx			
Change G286 to G159				xx		
Test G159 and collect Prof. and Dyn. data				xxx		
Change G159 to MXDA					xx	
Test MXDA and collect Prof. and Dyn. Data					xxx	
Change MXDA to MXZA					xx	
Test MXZA and collect Prof. and Dyn. Data					xxx	
Change the tire from MXDA to G159						xx
Drive IH Truck to Athens						xx
Departure / Travel						xxx

Virginia Route 114 Experiment

Background

This experiment is part of the project named “Integrated Infrastructure Asset Monitoring, Assessment and Management”, which is a collaborative effort of the University of Virginia, Center for Transportation Studies, Virginia Tech and the Virginia Transportation Research Council.

To build up a prototype pavement monitoring system, a wireless sensing network was designed, and installed on Virginia Route 114. Dr. Cristian Druta explored the available commercial sensing devices and provided an effective and efficient way to combine different sensors together into network. The author designed the layout of the sensing network to fulfill the multi-functionalities of the system. VDOT provided the opportunity to install the sensing devices into the public pavement, Virginia Route 114, during a reconstruction gap. Virginia Tech Transportation Institute provided the vehicles for test runs in experiments.

Sensing Devices

The final monitoring system contains two parts: sensors and wireless nodes. There are four kinds of sensors involved in the experiment, including strain gage, load cell, thermo couple and moisture sensors. Each of them comes from different company and will be described in detail in the following sections. All the specifications are attached in the Appendix A.

Horizontal and vertical strain gages used in the experiment are from CTL Company. CTL Asphalt Strain Gage is a field proven design to ensure accurate long-term data collection. It uses durable materials to withstand the high temperature and compaction loads in pavement construction. The strain gauges are shown in Figure 5.

a 

Figure 5: CTL Horizontal and Vertical Strain Gages

The calibration of all the strain gages used here is done with the strain wizard, coming with the software "MicroStrain Node Commander 2.4.0". The necessary parameters for strain wizard are listed in Table 6.

Table 6: Parameters in Software "MicroStrain Node Commander 2.4.0"

Bridge Type	Full Bridge
Number of Active Gauges	4
Gauge Factor	2.00
Gauge Resistance	350 ohm
Shunt Resistance	499000 ohm

The KDE-PA Soil Pressure Gauge (Figure 6) from Tokyo Sokki Kenkyujo Company is used in the experiment as load cell.

Figure 6: KDE-PA Soil Pressure Gauge

The load cell can be calibrated as in Eq.(1). Same calculation is executed on all the load cells, and the results are summarized in Table 7.

$$\text{Calibrated Slope} = \frac{\text{Sensor Capacity}}{\text{Rated Output} \times \text{Excitation Voltage} \times \text{Gain} \times \text{Transition Rate}}$$
$$= \frac{145 \text{ psi}}{484 \ \frac{\mu v}{v} \times 3 \ v \times 210 \times \frac{4096 \ bits}{3 \text{ v}}} = 0.348292 \text{ psi/bit} \qquad \text{Eq. (1)}$$

Table 7: Calculation results for all the load cells

Sensor	Serial No.	Rated Output	Calibrated Slope
A1	KDE-1MPA-EBJ100014	484	0.348292
A2	KDE-1MPA-EBJ110034	620	0.271892
B1	KDE-1MPA-EBJ110035	575	0.293171
B2	KDE-1MPA-EBJ110036	584	0.288621

The thermo couple TMTSS-125-6 from Omega Company is used to measure the temperature in the experiment. It makes of environmentally friendly cadmium-free liquid crystal polymer.

Figure 7: Thermo couple TMTSS-125-6

The thermo couple was calibrated with mercury thermo meter in water. Testing results are summarized in Figure 8, and the linear trend line is used for future temperature measurement.

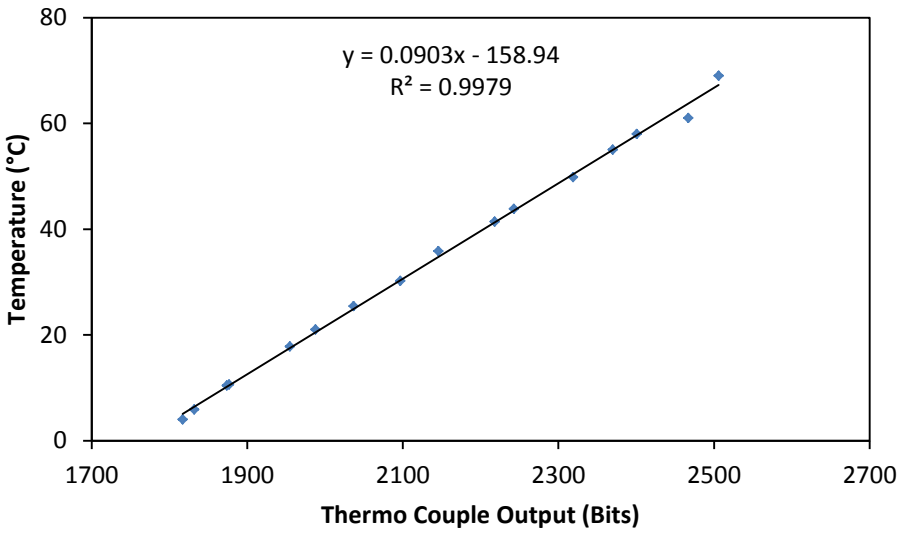

Figure 8: Calibration of Thermo Couple tmtss-125-6

VH400 Soil Moisture Sensor Probe, used in the experiment for moisture is from Vegetronix Company. It measures the dielectric constant of the soil using transmission line techniques. It is insensitive to water salinity, and will not corrode over time as conductivity based probes.

Figure 9: VH400 Soil Moisture Probe

The moisture sensor was calibrated with samples of increasing moisture content. The relationship between the output reading (bits) and the moisture content (%) is plotted in Figure 10.

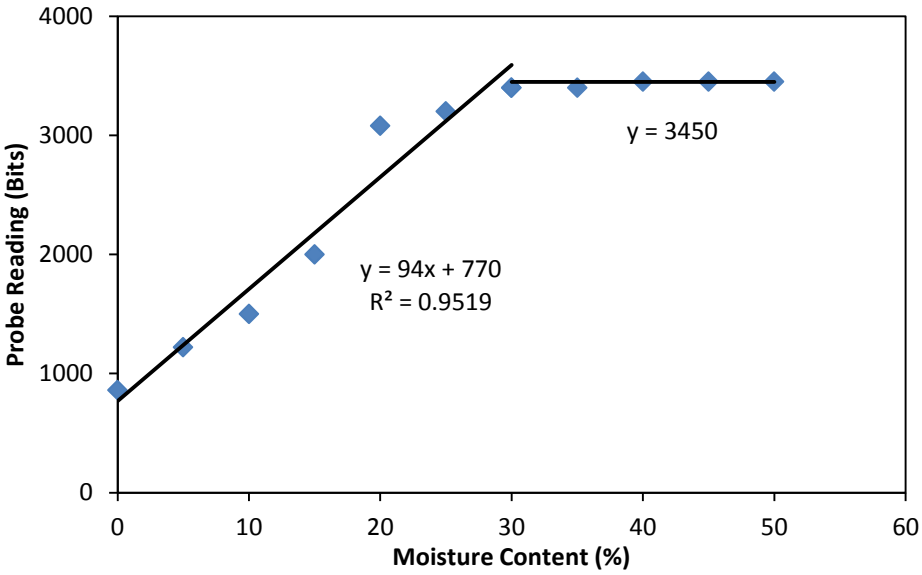

Figure 10: Calibration of VH400 Soil Moisture Probe

V-Link wireless voltage nodes are used as part of a high speed wireless sensor network. In the monitoring process, data was wirelessly transferred from the node to the base station. The maximum voltage the V-Link node can provide is 3 V. The V-Link node and the USB base station used in the project are shown in Figure 11, and the specifications are listed in the Appendix A.

Figure 11: V-Link Wireless Voltage Node and USB base station

Pavement Section and Sensor Distribution

The experiment section is located on Virginia State Route 114. Some archived plans show that this section of pavement predates the 1940's, and has been manipulated several

times with the opening of the Radford Arsenal, the opening of the second New River bridge and various maintenance activities that might have taken place over the past 70 – 100 years. It is nearly impossible to tell the existing pavement structure accurately without coring the pavement. According to the nearest cores (approximately 1 mile away) that VDOT provided, the thickness of the top layer is set to be 3 inch, and the basement is 7 inch thick in the future numerical simulation of pavement loading process. The statement of the overlay material is attached in Appendix B.

The installation must be finished in a gap of an overlay project of VDOT. It last for 3 hours on Oct 30th of 2012 and more than 5 hours on the Oct 31th with traffic under control. The total installation can be divided into 6 steps:

a. Marking the locations and shapes of the sensors on the pavement as in Figure 12(a);
b. Cut on the edge of the designed hole and vacate the asphalt concrete remains as in Figure 12(b);
c. Put the sensors in vacated holes and fix them at the designed positions with hot mixed asphalt concrete from the paver. Settle the cables in the pavement following the designed layout;
d. Cover the fixed sensors and cables with hot mixed asphalt concrete and compact.
e. The paver passes by, compact the asphalt concrete and leaves a 3 inch thick overlay, as shown in Figure 12(c);
f. Neaten and storage the output cables in a box by the side of the pavement, as in Figure 12(d).

Step 1-2 were finished on Oct 30th and steps 3-5 on Oct 31th. Several days later, the step 6 was finished.

Figure 12: Installation process
(a. marking, b. cutting, c. paver passing, d. output cable management)

Due to the funding limits, sensor distribution is designed to cover all necessary points of the back calculation with fewest sensors. Several groups of sensors are arranged on the important position of the transverse plane. Each group includes load cell, vertical strain gauge, horizontal strain gauge in longitudinal plane, and horizontal strain gauge in transverse plane, with 1 foot apart from each other. Five horizontal strain gauges are arranged in a straight line to make sure of the vehicle passing position in the transverse plane. The final layout is shown in Figure 13.

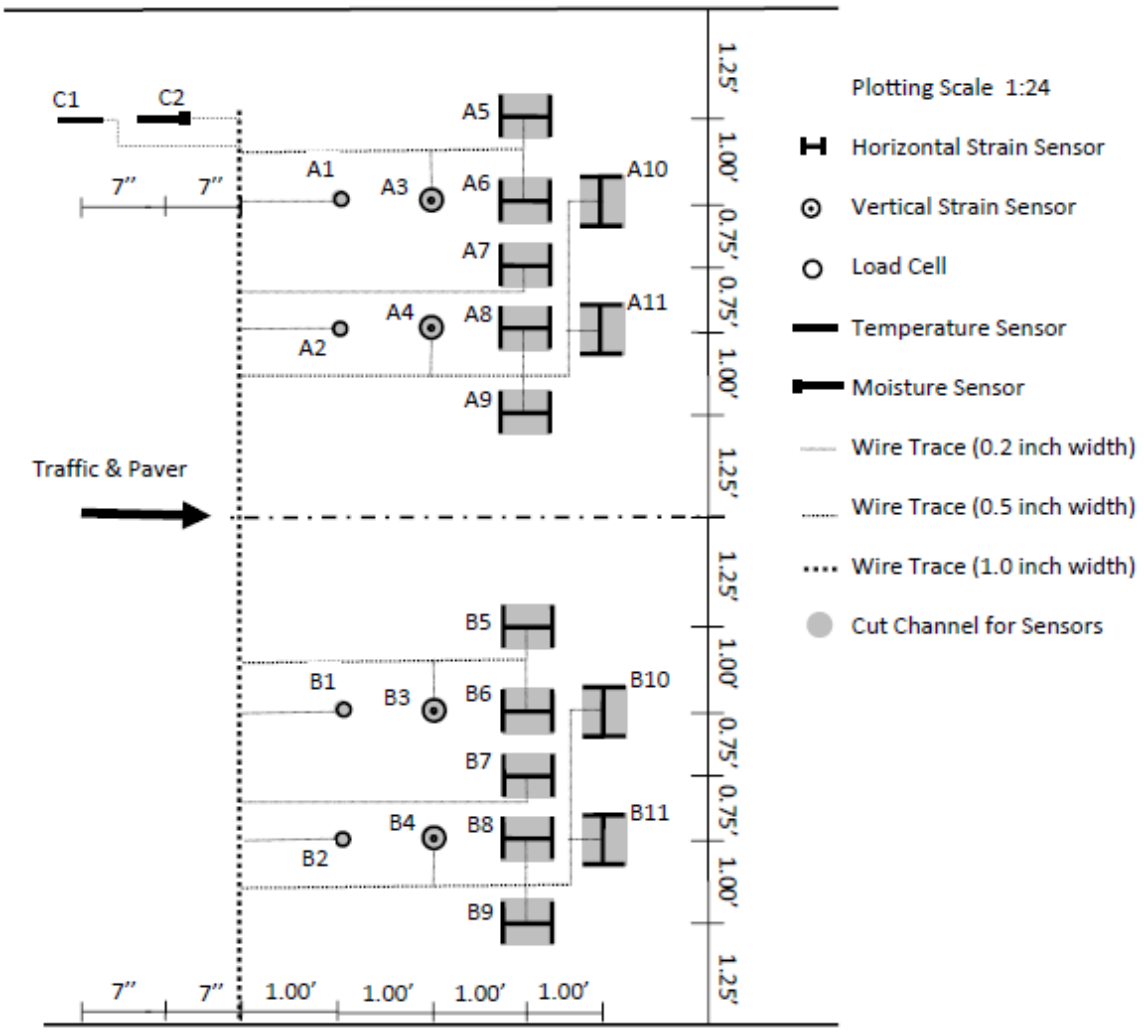

Figure 13: Sensor Distribution and Layout

Data Collection

After the installation, several checks were made to make sure that most of the devices work well. Lap top, base station and wireless nodes are necessary for the data collection in the experiment site. The collection of data logging can be prosecuted as the following steps:

a. Connect the wireless nodes and the output cables with minigrabbers, which are prepared in advance;

b. Run the software “Node Command”, developed for the V-Link wireless node, on the laptop with base station plugged in;
c. Include all the wireless nodes in the network;
d. Calibration and configuration for each wireless node;
e. Start streaming and obtain data logging

During tests, the test vehicle passed the experimental section with a constant speed, and all the pavement responses were recorded for the back calculations. The obtained strain, stress, temperature and moisture data were stored in the laptop and ready to be used for the further analysis. The data logging obtained by wireless node was stored with the sweep numbers, and the sweep rate was necessary to the calculation of time interval and specific time points. The sweep rate for different wireless nodes was different for continuous streaming mode.

In the most experiments, a van (Chevrolet Express 3500) was used in the experiment to provide a fixed loading condition. According to the truck scale in Virginia Tech Transportation Institute, the weight of the van is 6340 lb (±20 lb) with half tank of gas and back two benches removed. Considering the driver’s weight 150 lb and the weight of additional experimental devices 30 lb, the final weight used in the data analysis was 6520 lb, divided equally on the four single tires. However, to provide certain variations on axle load and vehicle configurations, three of other testing vehicles were also used. All the four involved testing vehicles are tabulated in Table 8.

Table 8: Summary of Testing Vehicles in Virginia Experiment

Vehicle	Manufacture	Year	Model	Weight (lb)	Distance between Axles (inch)	Distance between Wheels (inch)	Width of Tire (mm)
1	Chevrolet	1999	Express 3500	6603	160	67.5	245
2	Ford	1997	Taurus LX	3753	108.5	61.5	205
3	GMC	1998	Sierra	4724	132.5	64	225
4	Ford	2001	Escape	3730	103	60.5	235

NOTE: 1 lb = 0.454 kg; 1 inch = 25.4 mm. Weight listed includes the weight of the vehicle, one drivers and one passenger.

PAVEMENT HEALTH STATUS MONITORING

As one of the most important and expensive investments/assets in the modern society, asphalt concrete pavement ages and deteriorates with time as a result of asphalt mixture aging, excessive use, overloading, environmental conditions, and inadequate maintenances. All of these factors contribute to the deterioration process which is very complicated. Various pavement distresses, including cracking, rutting, wear, deflection and so on, are important indicators of pavement performance. In this project, a pavement health monitoring system was developed based on embedded wireless sensing network.

Pre-investigation of signal traces

The shape and magnitude of the collected traces are the objective of the signal analysis, and the monitoring system works well only if the collected signal is clear and reliable. It is important to judge whether the signal traces are useful and reliable for the following back calculation. Figure 14 shows the responses from different sensors for the same passing vehicle.

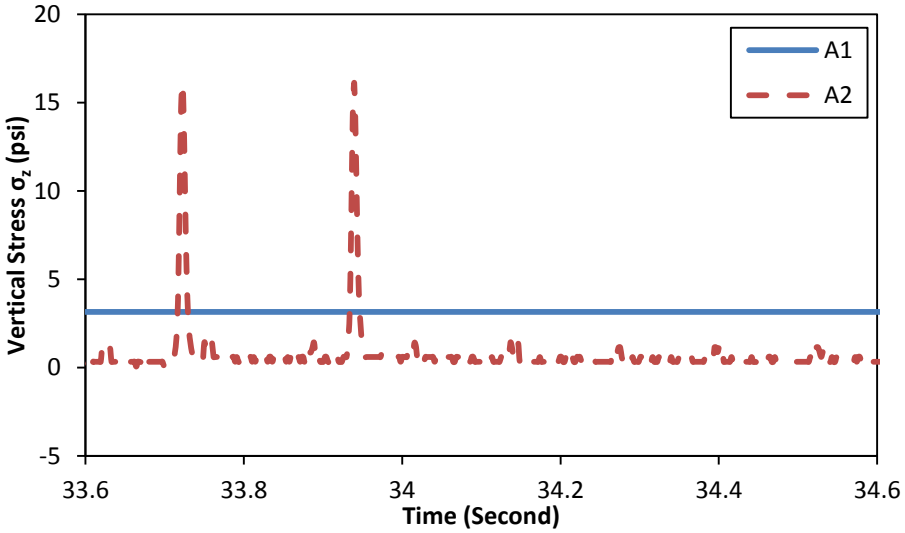

(a) Signals from Load Cells

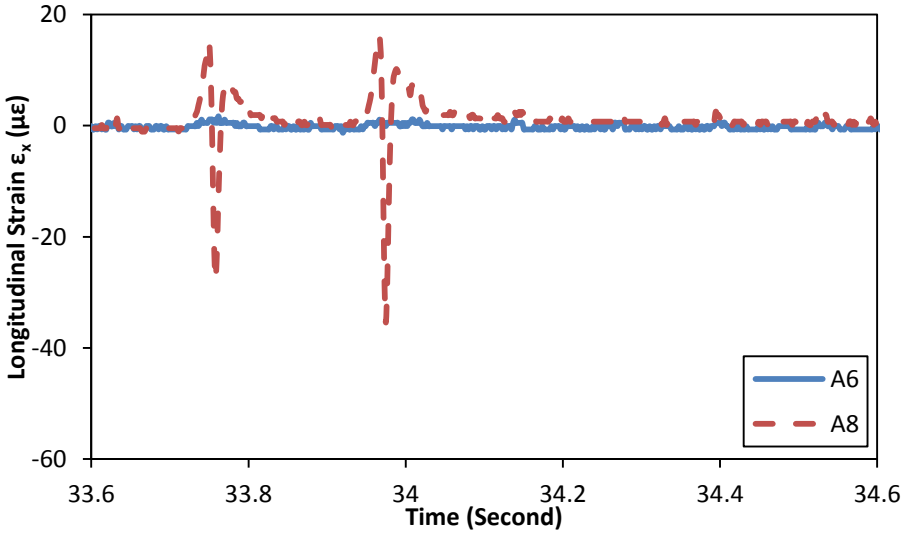

(b) Signals from Longitudinal Strain Gages

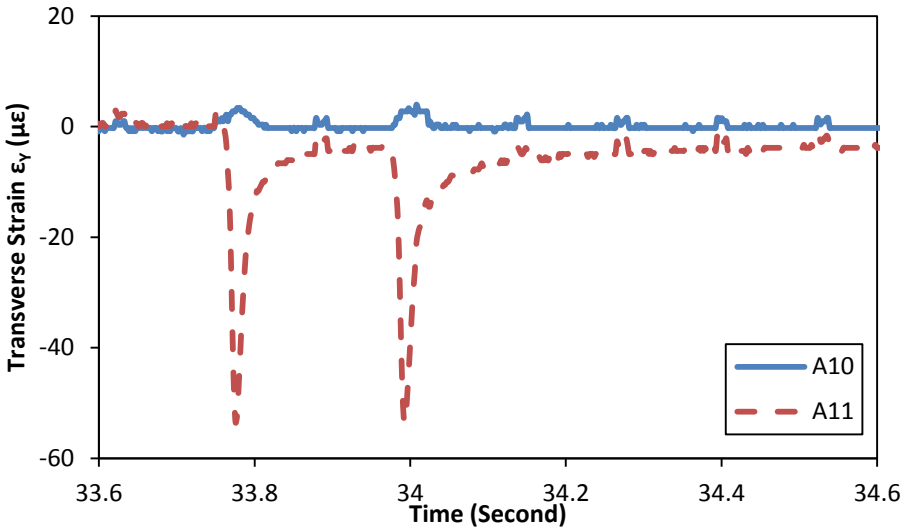

(c) Signals from Transverse Strain Gages

Figure 14: Samples of Signals collected in an on-site experiment

Sep 13 2012, Series 1, Run #7

As shown in Figure 14, the signals from sensor A2, A8 and A11 were continuous, clear and reasonable, and obvious responses showed up with corresponding loading from front and rear axles. The obvious response from these three sensors told that the tire passed just over or very close to these three sensors, and induced obvious strain fluctuations.

For the sensor A6 and A10, the responses corresponding to axles were blurred and almost submerged in the background noise. The neglectable responses of A6 and A10 told that the tire passed the experimental sections far from these two sensors, and induced little response.

There wasn't any response from the sensor A1, not even the background noise, and it was because that either this sensor had been broken after the installation or it was not connected well to the data logger. Some other sensors were also damaged, including all

the vertical strain gages and some horizontal strain gages. The reason might include the harsh environment, extreme load or improper installation.

Such analysis was prosecuted on many cases to pre-investigate the signals, and useful conclusion can be driven out of them.

a. The strain and stress response is quite small and neglectable when the tire doesn't pass on it or close to it.
b. Sensors in various directions have different coverage, and obtain signals for the same passing vehicle with differential quality.

The pre-investigation of the obtained signal is very important for the whole monitoring system. Only the signals with clear and reliable information can be used in the following back calculation. To realize an intelligent transportation monitoring system, such pre-judgment will be programmed as a normal procedure for each passing vehicle.

Strain and Stress Distribution

The traces of strain and stress are the basis of the following analysis of pavement health status and traffic information. It is necessary to fully understand the distribution of strain and stress in the pavement. So for a typical run, traces collected are categorized as in Figure 15.

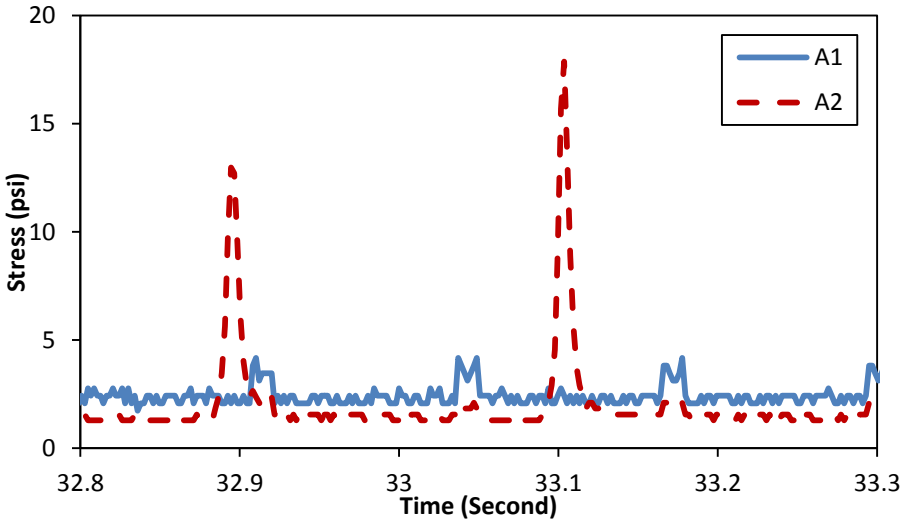

(a) Vertical Stress

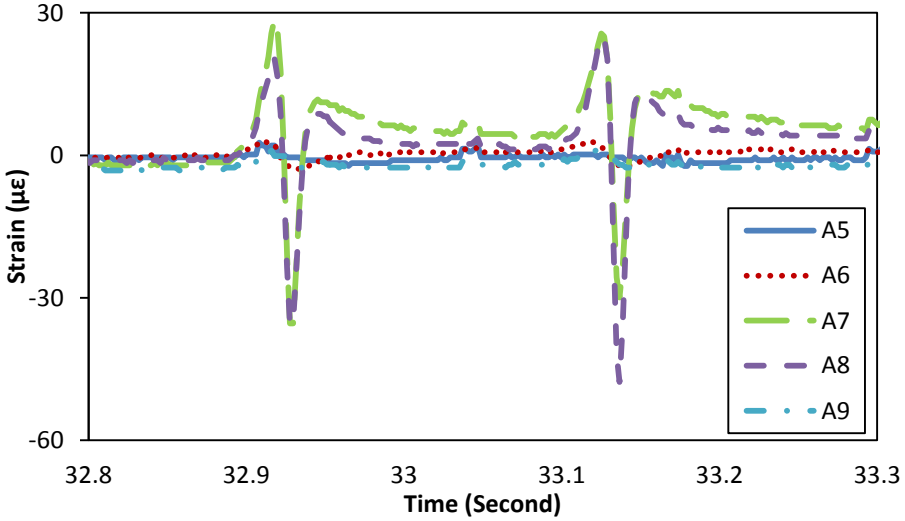

(b) Longitudinal Strain

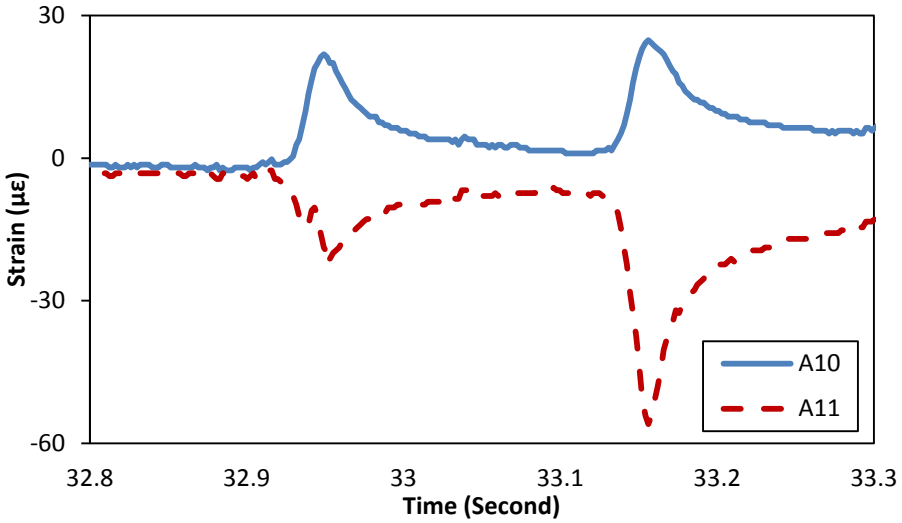

(c) Transverse Strain

Figure 15: Typical strain and stress traces collected in Virginia experiment

June 25 2012, Run #2

As shown in Figure 15, the magnitude of strain and stress response was highly related to the passing position of the vehicle. The stress from A2, as shown in Figure 15 (a), was much than that from A1 because the tire passed close to A2. In Figure 15 (b), the response from A7 and A8 were much bigger than those of A5, A6 and A9, which told that the center of the tire passed between A7 and A8. In Figure 15 (c), the signal of A11 was negative, which meant that the sensor A11 was in tension, and just under the tire; the response of A10 was positive because the sensor A10 was out of the loading range, and compressed for the compensation effect. In general, the response close to the tire is quite obvious, and the one far away from the tire is almost neglectable.

Numerical Simulation

Asphalt concrete exhibits both linear elastic and viscoelastic properties, and is considered a linear viscoelastic material in this study. This means that the material modulus and

therefore strain, is affected by both temperature and loading frequency. With the principle of time temperature superposition, reduced frequency can be calculated from temperature and absolute frequency, on which material property only depends instead of temperature and absolute frequency separately. The reduced frequency and the reduced time are defined in Eq. (2-3).

$$\omega_R = \omega \times \alpha(T) \qquad \text{Eq.(2)}$$

$$t_R = \frac{t}{\alpha(T)} \qquad \text{Eq.(3)}$$

where ω is the actual loading frequency, $\alpha(T)$ is temperature shift factor, T is temperature, $\omega(R)$ is reduced frequency; t is the actual loading time, t_R is reduced time. Based on the dynamic test results provided by VDOT, the dynamic master curve of the target asphalt concrete layer under the reference temperature 70ºF after placement is shown in Figure 16, together with the shift factors under different temperatures.

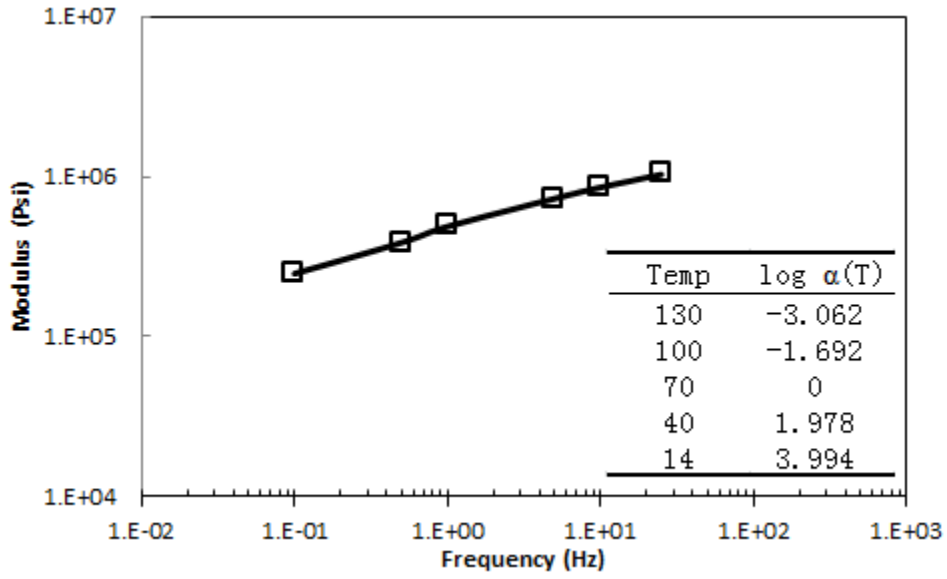

Figure 16: Original dynamic master curve of the surface layer

Finite Element Method (FEM) based software ABAQUS was used to perform mechanical analysis of the pavement section theoretically. Viscoelastic property present in Figure 16 was for the surface layer of asphalt mixture, and the sub-layers were treated as linear elastic materials. It was simulated that a wheel passes the experimental section at the measured speed under the corresponding temperature. The numerical model is shown in Figure 17. The comparison between the calculated horizontal strain response and field measurements is shown in Figure 18.

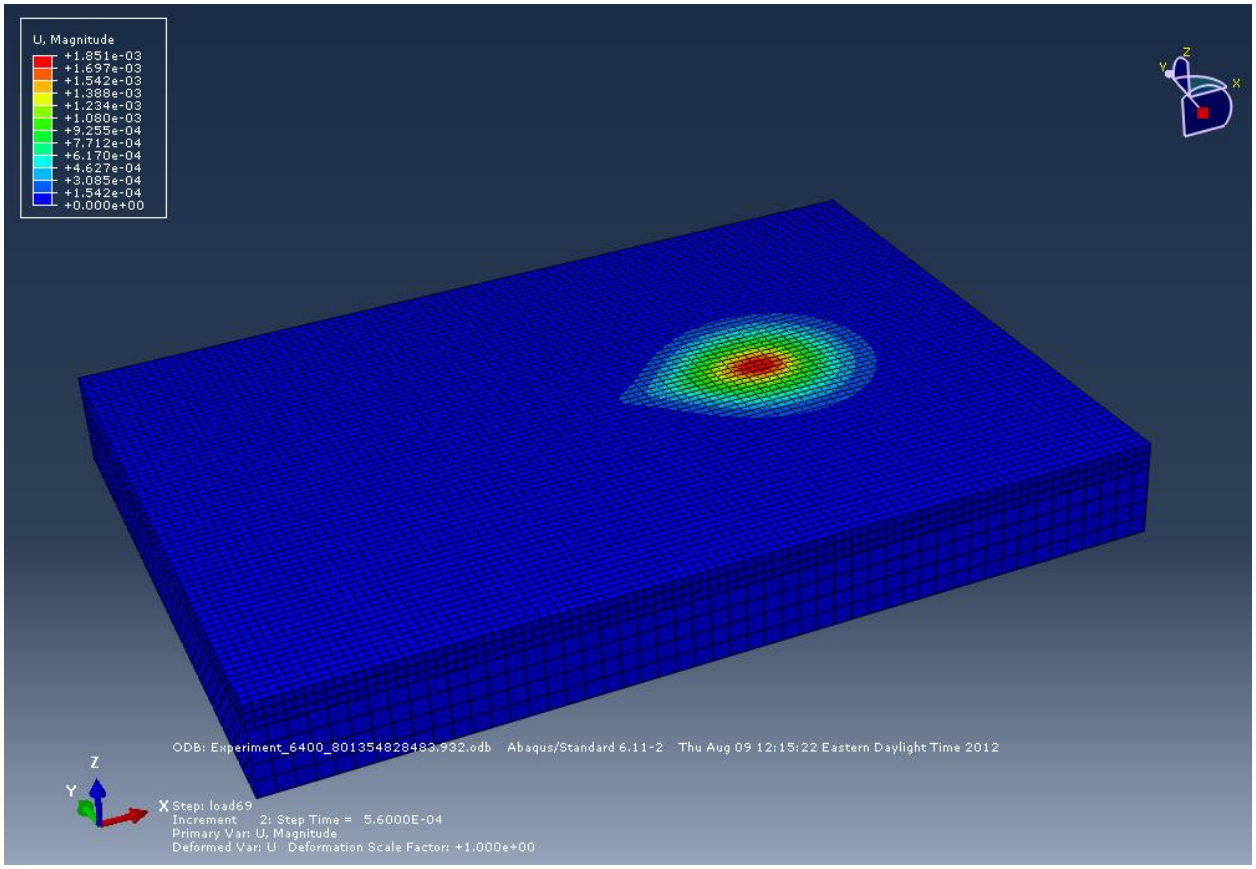

Figure 17: Numerical simulation with ABAQUS

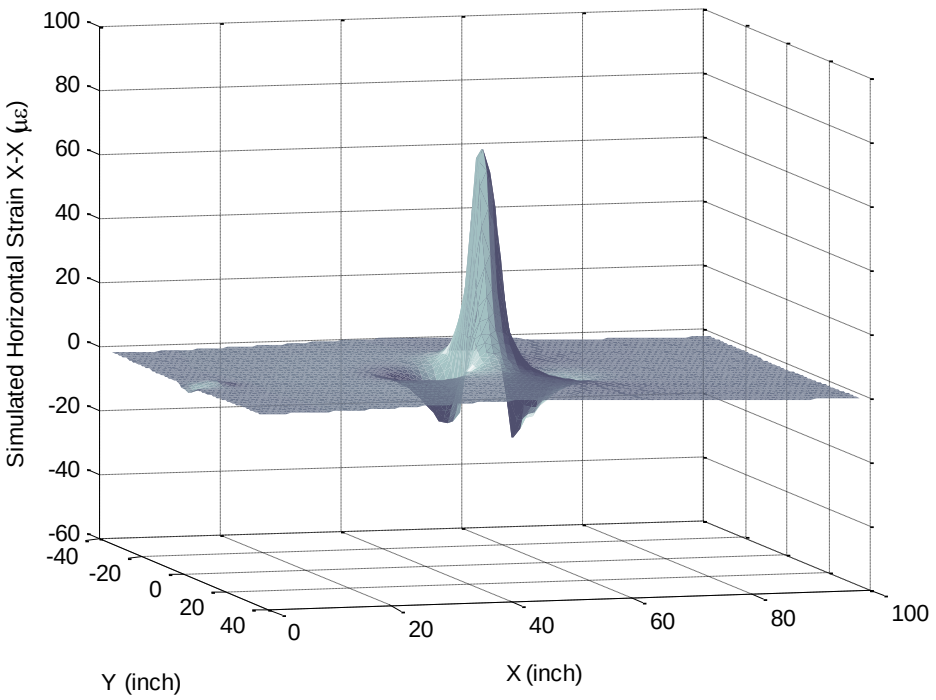

(a) ABAQUS simulation

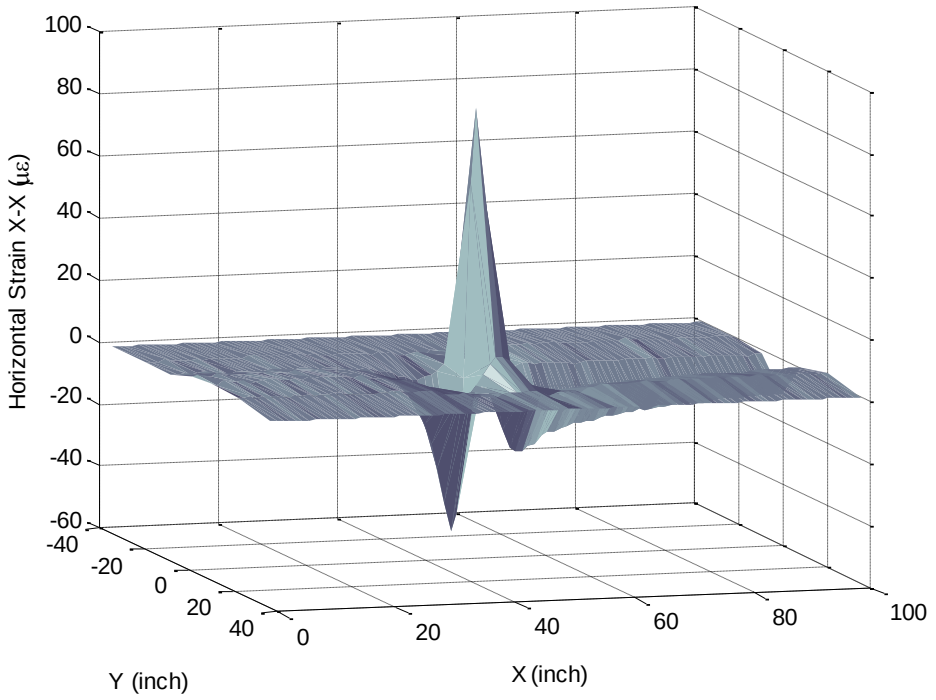

(b) Field measurement

Figure 18: Distribution of horizontal strain response X-X

X is the horizontal longitudinal direction, parallel to the traffic; Y is the horizontal transverse direction, transverse to traffic.

As shown in Figure 18, the simulated strain distribution matched with field strain measurement very well in the shape. Though some error in the magnitude, it was understandable considering the localized pavement structure, variation of material property, and other factors. The precision of 3-dimensional figure in Figure 18(b) is low because only 5 strain gages were used.

Back Calculation of Asphalt Concrete Layer

To estimate the structural strength is an important objective of structural evaluation. "For asphalt pavements, it may be expressed in terms of in situ layer elastic moduli, layer thickness, inter-layer bond conditions and anomaly characterization"[65]. Using the proposed pavement health monitoring system, the modulus of asphalt concrete can be back calculated every three or six months based on the policy. The ratio between σ_A (normal stress in direction A) and ε_B (normal strain in direction B) was used to back calculate the elastic modulus of asphalt concrete layer as defined in Eq.(4):

$$R_{AB} = \frac{\sigma_A}{\varepsilon_B} \qquad \text{Eq.(4)}$$

The original intention while designing the sensing network was to use collected vertical stress and vertical strain for the modulus back-calculation. However, the vertical strain gauges installed were all out of service due to the harsh environment and improper installation. Currently, horizontal strains collected were used for modulus back-

calculation instead of vertical strain. The relationship between vertical stress and vertical/horizontal strain was explored by ABAQUS simulation shown in Figure 19.

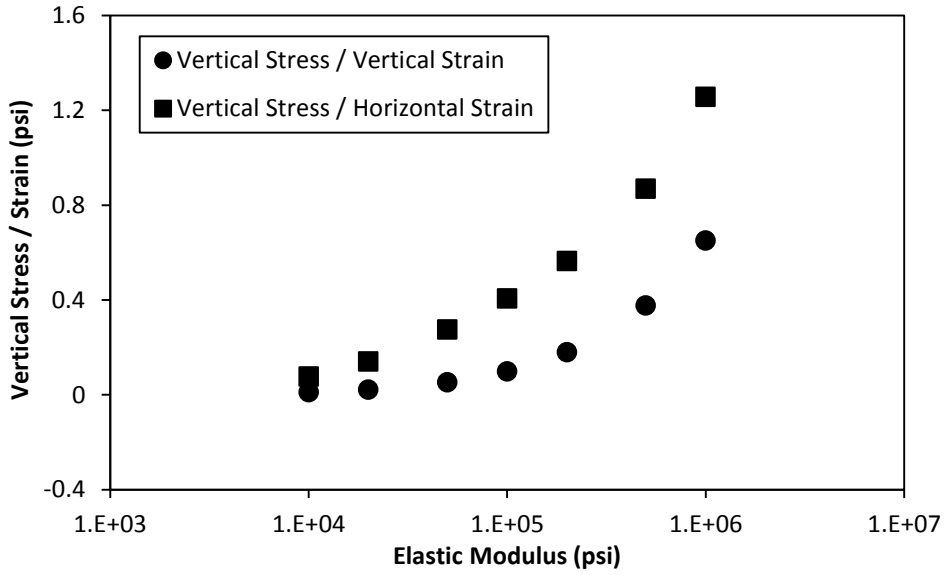

Figure 19: Simulated Relationship between the Parameter R and the Modulus

As shown in Figure 19, the ratio between vertical stress and horizontal strain R_{ZX} was related with the elastic modulus of the asphalt concrete layer with a similar trend as R_{ZZ} and can be used to back calculate the modulus of the layer.

For example, the traces with testing vehicle passing directly on sensor A6 and A8 were chosen to demonstrate the back-calculation process of pavement dynamic modulus. The parameter R_{ZX} was calculated from the collected strains and stresses with changing temperature and two speeds, as shown in Figure 20.

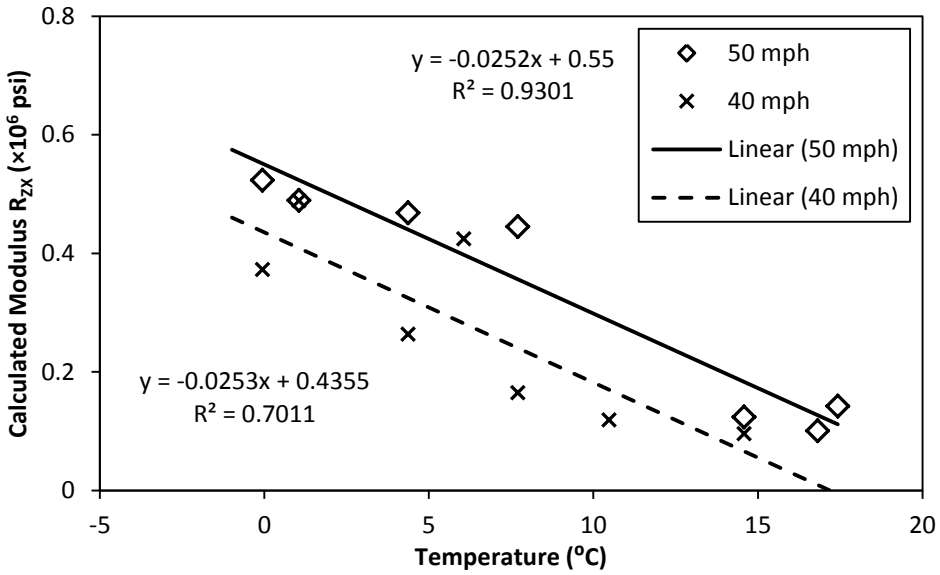

Figure 20: Back Calculated Parameter R_{XZ} with Changing Temperature and Speed

As seen in Figure 20, the calculated parameter R_{ZX}, which was proved to be related to pavement modulus in Figure 19, decreased with temperature and increased with testing vehicle velocity. The trend present made a lot of sense for asphalt concrete which is usually treated as viscoelastic. The vehicle speed in the finished testing runs was limited to 40 and 50 mph to avoid traffic disruption, and in the actual pavement monitoring system, the testing velocity can be set from 5 mph to 80 mph to build up the dynamic modulus of the experimental section similar as Figure 16.

Pavement Distress Prediction

Based on the intention of this research, various pavement distresses can be predicted based on the pavement responses. However, due to the limited scope and distribution of sensing network in the project, only fatigue cracking and rutting were taken into consideration.

Fatigue Cracking

The cumulative damage concept has been widely used to predict fatigue cracking. It is generally agreed that the allowable number of load repetitions is related to the tensile strain at the bottom of the asphalt layer. The major difference in the various design methods is the transfer functions that relate the tensile strains in asphalt concrete layer to the allowable number of load repetitions.

For comparison purposes, current Mechanistic-Empirical Pavement Design Guide [66](MEPDG) fatigue cracking model is used, and the fatigue damage of each tire to the experimental section is calculated in Eq. (5-7).

$$N_f = 0.00432C\left(\frac{1}{\varepsilon_t}\right)^{3.291}\left(\frac{1}{E}\right)^{0.854} \quad \text{Eq.(5)}$$

$$C = 10^M \quad \text{Eq.(6)}$$

$$M = 4.84\left(\frac{V_b}{V_a + V_b} - 0.69\right) \quad \text{Eq.(7)}$$

Where N_f = the allowable number of load repetitions for fatigue cracking; ε_t = the tensile strain at the critical location, which is the bottom of asphalt concrete layer; E = the stiffness of asphalt mixture; V_b = the effective binder content (8.4%) and V_a = the air voids of the asphalt mixture (7.4%).

To calculate the fatigue cracking damage brought to the pavement by each run, Eq.(5) can be converted into Eq.(8).

$$D_{fc} = 231.48\frac{1}{C}(\varepsilon_t)^{3.291}(\mathrm{E})^{0.854} \quad \text{Eq.(8)}$$

where D_{fc} is the fatigue cracking damage brought by each passing vehicle to the pavement section. In the target pavement monitoring system, the parameter $D_{fc,i}$ can be calculated after each passing vehicle, and added into the total D_{fc} as an index of fatigue cracking. When D_{fc} equals to 1, theoretically the pavement section is totally damaged because of fatigue cracking.

Rutting

Permanent deformation is another factor for flexible pavement design and maintenance. "With the increase in traffic load and tire pressure, most of the permanent deformation occurs in the upper layer rather than in the subgrade"[67]. Since only the strain in the asphalt concrete layer is measured in the experiment, then the rutting depth calculated in the paper is only for the asphalt concrete layer of the experimental sections.

The Mechanistic-Empirical Pavement Design Guide (MEPDG) rutting model is used to estimate the rutting depth of experimental sections. This model is derived from statistical analysis of the relationship between plastic and elastic compressive strain in experiments.

$$\frac{\varepsilon_p}{\varepsilon_r} = k_1 \cdot 10^{-3.4488} T^{1.5606} N_r^{0.479244} \quad \text{Eq.(9)}$$

where $\varepsilon_p =$ accumulated plastic strain at N repetition of load; $\varepsilon_r =$ resilient strain of the asphalt material; $N_r =$ number of load repetitions; $T =$ Pavement Temperature, and k_1 is

the function of total asphalt layer(s) thickness (H_{ac}) and depth to computational point, as defined in Eq.(10-12).

$$k_1 = (C_1 + C_2 \cdot depth) \cdot 0.328196^{depth} \quad \text{Eq.(10)}$$

$$C_1 = -0.1039 \cdot H_{ac}^2 + 2.4868 \cdot H_{ac} - 17.342 \quad \text{Eq.(11)}$$

$$C_2 = 0.0172 \cdot H_{ac}^2 - 1.7331 \cdot H_{ac} + 27.428 \quad \text{Eq.(12)}$$

Then the overall permanent deformation can be computed as sum of permanent deformation for each individual sub-layer in Eq.(13).

$$PD = \sum_{1}^{NS} \varepsilon_p^i \cdot h^i \quad \text{Eq.(13)}$$

where PD = pavement permanent deformation; NS = number of sub-layers; ε_p^i = total plastic strain in sub-layer i; and h_i = thickness of sub-layer i.

In this project, all the sensors were installed at the same depth, and the whole asphalt concrete layer was treated as one sub-layer, and 12.5 mm rutting depth was used as a failure criterion $PD_{failure}$. Then the rutting damage induced by each vehicle can be calculated based on the allowable number of load repetition for vertical rutting depth.

$$D_r = \frac{1}{N_r} = \left(k_1 \varepsilon_r \frac{h}{PD_{failure}}\right)^{2.086620} T^{3.256379} 10^{-7.196335} \quad \text{Eq.(14)}$$

where D_r is the rutting damage brought by each passing vehicle to the pavement section. D_r can be computed for each passing axle and summed up as an index of rutting depth.

When D_r equals to 1, theoretically the section is totally damaged because of vertical rutting.

The calculations in this section can be performed easily in the real-time monitoring process. In the current prototype period, real-time continuous monitoring for a long time has not been tried to provide an example.

Health Monitoring System Prototype

According to the studies above, it is feasible and practical to build up a pavement health monitoring system based on the instrumented sensing network. The prototype of this monitoring system is present in Figure 21.

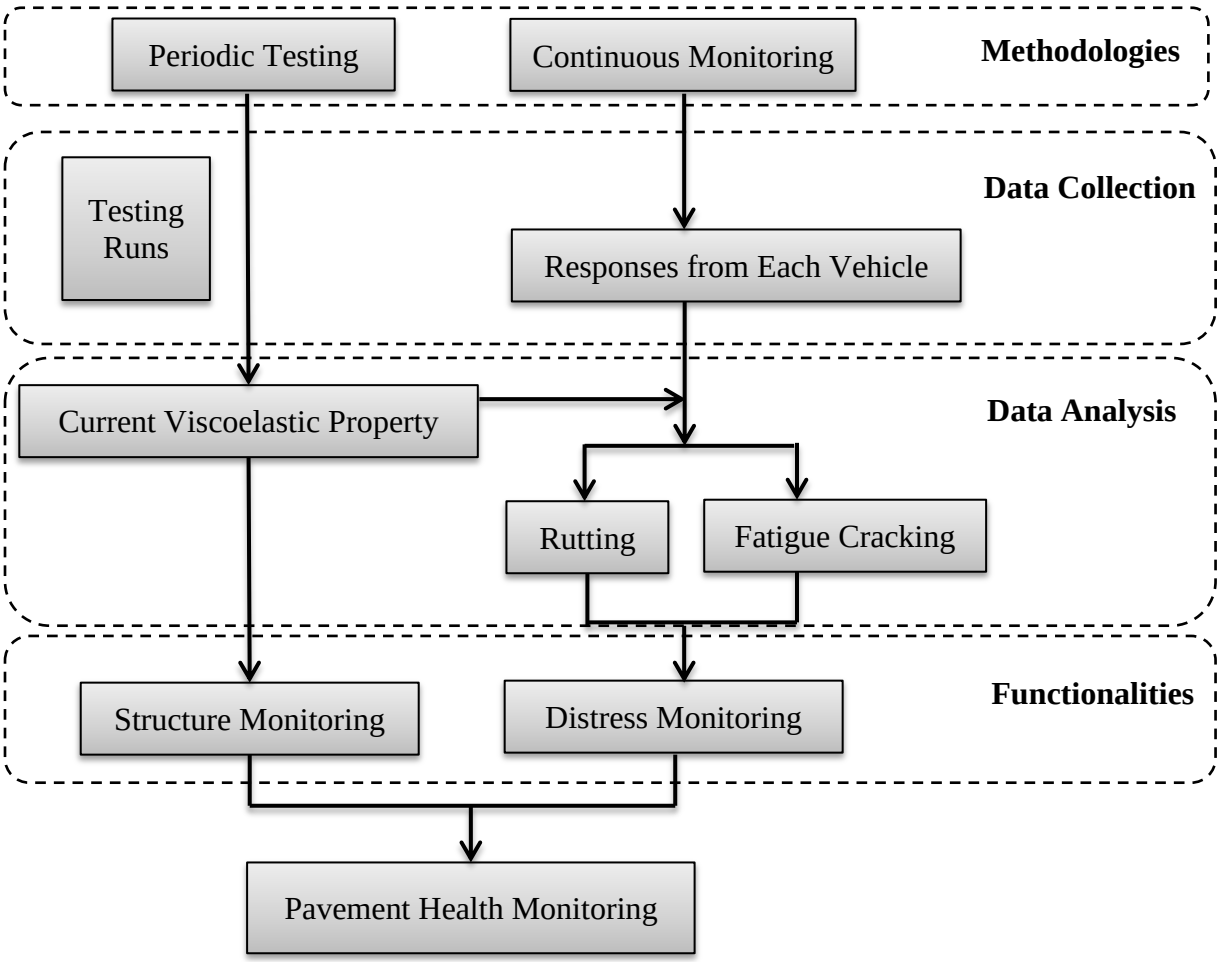

Figure 21 Prototype of the Pavement Health Monitoring System

As shown in Figure 21, the routine monitoring contents of this system include periodic testing and continuous monitoring. The periodic testing can be conducted every year or other fixed period with testing runs, and the back-calculated dynamic modulus can be used to evaluate the health status of the pavement structure. At the same time, the strain/stress responses in pavement are collected in continuous real-time monitoring for each passing vehicle. Pavement distresses can be predicted with the collected mechanical response with different pavement distress prediction model, used for pavement management system.

Discussion and Conclusion

In this chapter, a complete pavement health monitoring system was proposed based on common commercial pavement sensors. A well-designed sensing network was designed and connected to the corresponding computer via wireless data loggers. Four physical measurements based on different pavement sensors were exploited, including temperature, moisture, strain and stress. The FEM simulation of strain distribution using viscoelastic material model for asphalt concrete agreed well with those experimental measurements. The ratio between vertical stress and longitudinal horizontal strain was demonstrated to be related to the strength of pavements in numerical simulation, and can be used to back-calculate pavement modulus. The MEPDG fatigue cracking and rutting models were written into the damage brought by each passing axle, and taken into the prediction of pavement distresses for the health monitoring system. A working prototype of pavement health monitoring system was set up to clarify the routine monitoring content, data analysis process and final functionalities.

In general, this monitoring system is based on the in-situ pavement sensors, and has a high feasibility and practical value to be carried out for pavement management and research purposes because of the following advantages:

(1) Low cost for installation and maintenances;

(2) Taken the actual strain response in pavements into the distress prediction;

(3) Valuable for the validation of pavement distress models;

(4) Can be integrated with other pavement instrumentation (Weigh-In-Motion, Energy Harvesting and Traffic Classification systems) easily.

TRAFFIC MONITORING

The experiment on Virginia Route 114 was designed to be a comprehensive transportation monitoring system. The monitoring targets include not only the pavement health status, but also the information of the traffic. The traffic monitoring here means that the system will monitor the passing traffic about the related aspects using collected signal traces.

The analysis of pavement responses can be categorized into two groups: temporal and spatial depending on the distribution of the pavement response. The following two sections are going to talk about the methodologies and back-calculation method used in the monitoring system. A flow chart is present in the third section to show the frame of the whole traffic monitoring system.

Temporal Distribution

Data analysis in this section focuses on the pavement responses distribution via time. The time interval between response fluctuations were extracted and analyzed for further information about the passing vehicle and the traffic flow.

Involved mechanical responses

As shown in Figure 13 of the chapter “Experiments”, the instrumented sensing devices in this project were located all over the whole section. To study the spatial distribution of strain response, the strain gauges in different directions and load cell were arranged straight in the direction of traffic and treated as pavement responses in different

directions at the same point. To clarify the spatial positions of the ten horizontal strain gauges, related part of Figure 13 was enlarged and adjusted as in Figure 22.

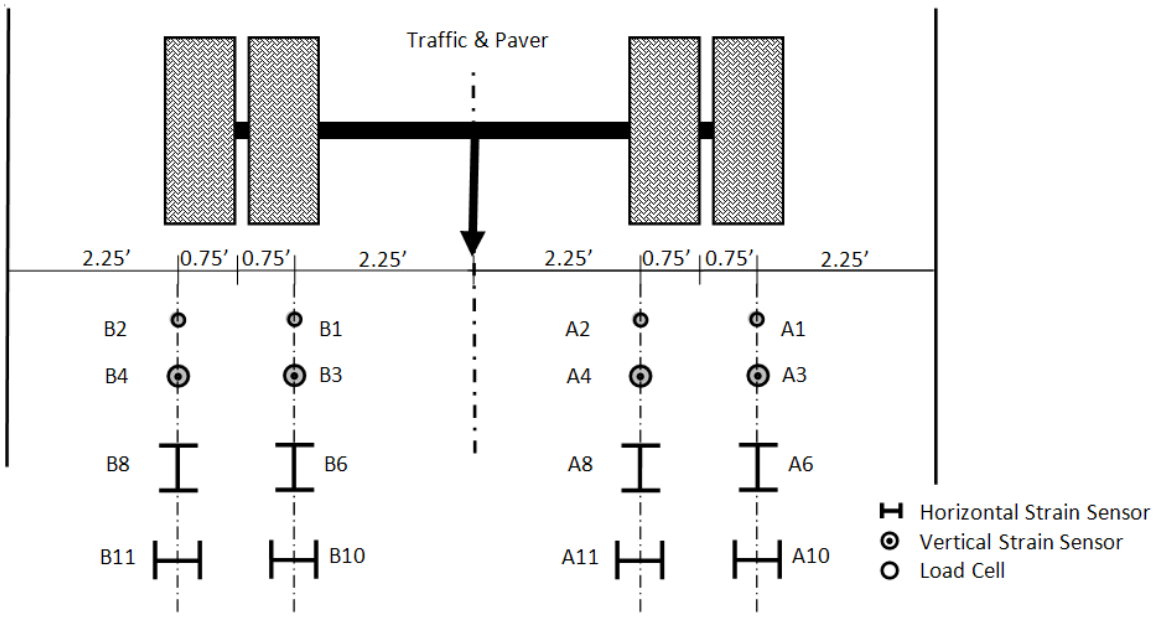

Figure 22: Layout of the sensing devices for temporal analysis.

As shown in Figure 22, each sensor distribution group included 4 sensors: 1 load cell, 1 vertical strain gauge, 2 horizontal strain gauges (longitudinal and transverse directions). The responses from a sensing group in a test run are displayed in Figure 23.

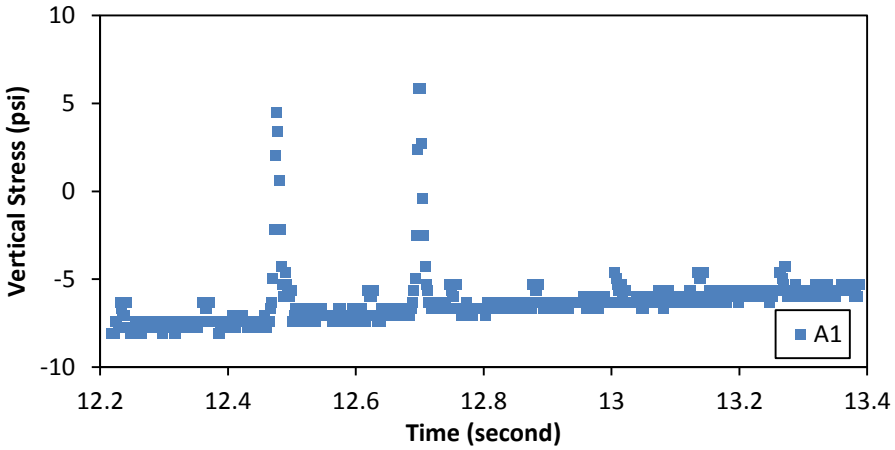

(a) Signals from load cell A1

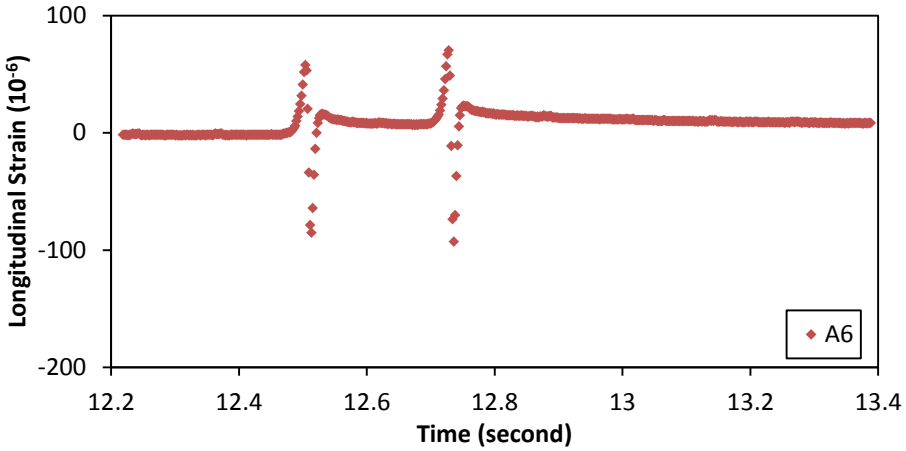

(b) Signals from horizontal strain gauge A6 in longitudinal direction

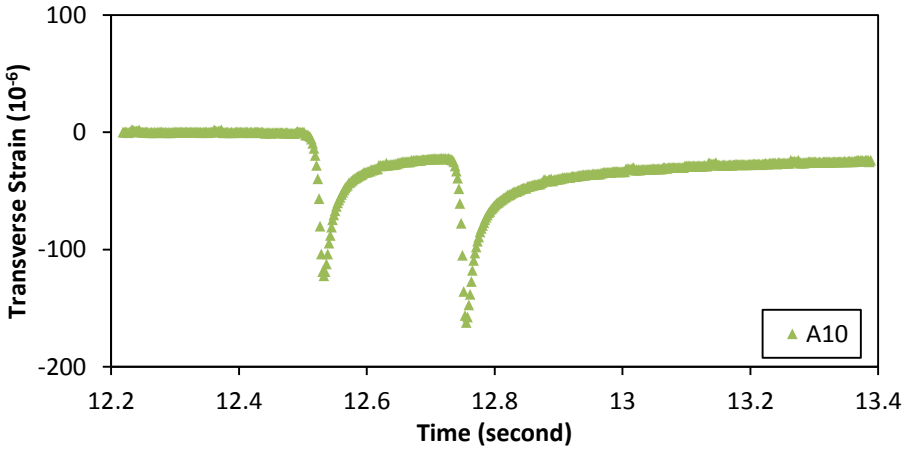

(c) Signals from horizontal strain gauge A10 in transverse direction

Figure 23: Responses from the sensor A1, A6, A10 in a typical testing run.

As seen in Figure 23, the strain and stress responses in various directions had different shapes in the same test run. The following analysis was based on the temporal distribution of pavement's mechanical responses.

Traffic Volume

Traffic volume is a necessary statistics for traffic flow control and management, which is usually a responsibility for various Departments of Transportation for public study of traffic flow. In this study, the traffic volume can be obtained by counting and grouping

the fluctuations of strain responses in continuous monitoring. Since there were five horizontal strain gages distributed in either wheel path, the signals can be combined together to cover the whole path. A simple but efficient way can be used to count the number of passing vehicle based on the sum of strain responses. The sum of collected strain responses in transverse plane can be calculated as in Eq.(15).

$$SS = S_{A5} + S_{A6} + S_{A7} + S_{A8} + S_{A9} \; or \; S_{B5} + S_{B6} + S_{B7} + S_{B8} + S_{B9} \qquad \text{Eq.(15)}$$

Where S_{Ai} and S_{Bi} represent the strain response signal from the left and right wheel path, as labeled in Figure 13. As an index of traffic flow, SS changed obviously with each axle of load on pavements. The fluctuation from each vehicle can be recognized as shown in Figure 24.

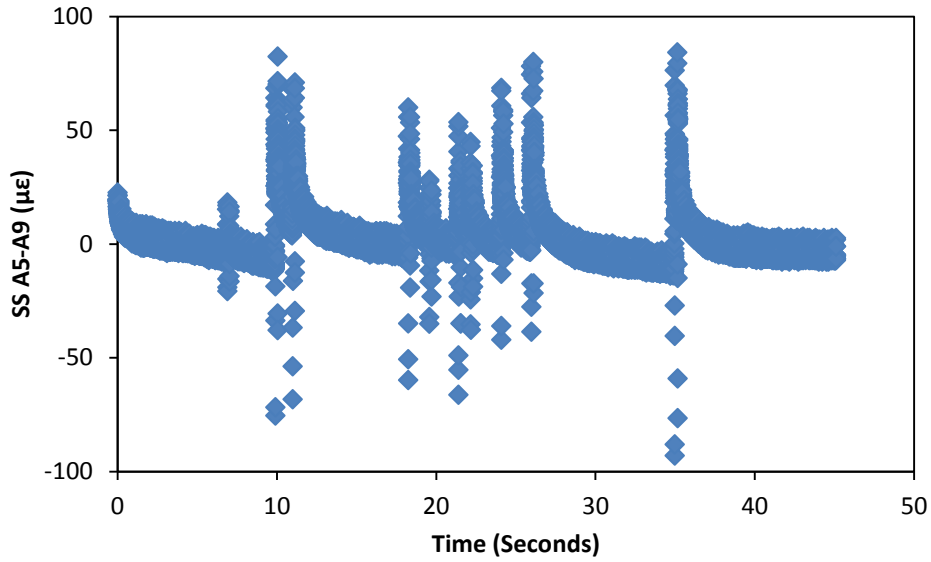

Figure 24 Sum of strain A5-A9 in 45 seconds

Aug 8 2012, Series 1, Run 2

As shown in Figure 24, the strain fluctuations from each passing vehicle can be recognized from the continuous signal in real-time monitoring. In the 45 seconds, it can

be told from the signal that two vehicles passed around the 10th second; 6 vehicles passed between the 15th and 30th second compactly; a vehicle passed around the 35th second and total 10 vehicles passed in the whole period. The information provided by this vehicle counting method was compared with the field observation and video record many times, and has been verified to be very reliable.

With this back calculation method, the number of axles and vehicles can be easily obtained at the same time of the traffic flow with a very low calculation cost. Since the horizontal strain gages A5-A9 cover the whole wheel path, all the passing vehicle in this lane can be captured without considering their positions.

Number of axles

The number of axles is a necessary parameter for traffic classification, and can also be recognized with the same method described in the previous section. The recognition of vehicle number and axle number of each vehicle are both based on counting the response fluctuations, and the only difference is the interval between the fluctuations. The response fluctuations close to each other were grouped and recognized as a vehicle. The fluctuations in each group were counted as the number of axles for this vehicle. For example, the collected signal in Figure 24 is localized between 21st and 27th second as in Figure 25.

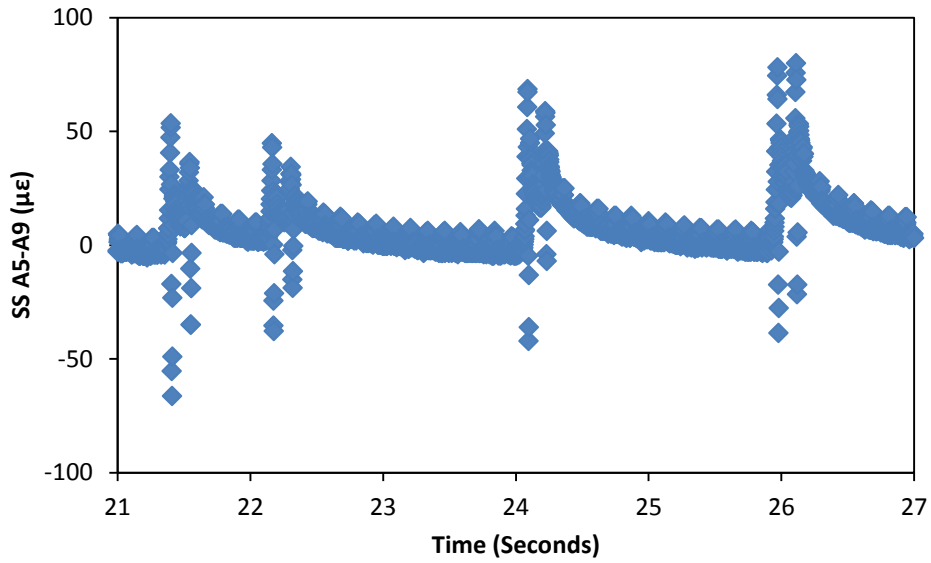

Figure 25 Localized signal between 21st and 27th second

Aug 8 2012, Series 1, Run 2

As shown in Figure 25, the separate fluctuations caused by axles can be recognized and counted for the four vehicles passed between the 21st and 26th second. The strain fluctuations with time interval less than a specific length were usually grouped into the same vehicle. The determination of the criterion depends on the calculated speed of the vehicle.

Speed

The vehicle speed is a necessary parameter for the back-calculation because the speed of the passing vehicle can affect the viscoelastic properties of the pavement and traffic counting. At the same time, speed is also an important objective for the traffic monitoring because the speed of the traffic can be an index for both safety control and the efficiency of the traffic flow. There are two methods present in this section to calculate the speed of the passing vehicle.

If the model of the passing vehicle is known, then the distance of the wheels is fixed, and then the speed can calculated with the time interval of the two fluctuations caused by the front and rear tires separately in Eq.(16).

$$SP = \frac{D_{Axles}}{T_2 - T_1} \qquad \text{Eq.(16)}$$

where SP is the speed of the passing vehicle; D_{Axles} is the longitudinal distance between axles; T_1 and T_2 are the corresponding time coordinates for front and rear fluctuations. This equation is theoretically accurate, and proved in our experiment. For example, the signal present in Figure 26 was collected for a passing vehicle, whose speed is controlled at 50 mph manually.

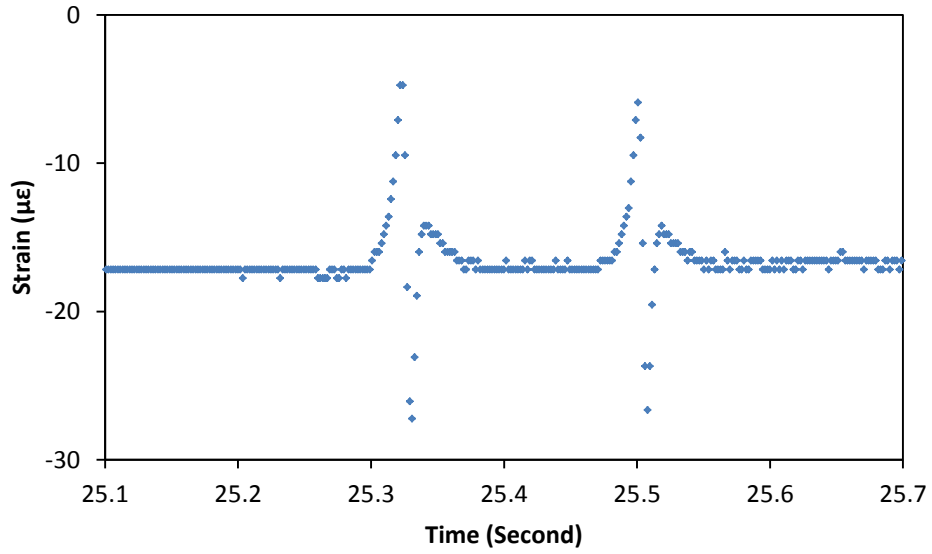

Figure 26: Signal Sample Collected in an On-Site Experiment

Data collected from B5 on June 6 2012.

This method is very easy and convenient, and feasible when only one or two traces of strain or stress are captured. However, the disadvantage is also very obvious, because the distance between the axles has to be known.

In fact, the models of the running vehicles on the pavement were unknown to the researchers, and the first present method can't be used. In this case, the velocity can be calculated with the traces of different sensors. Since the sensors were installed with different x (longitudinal coordinates, in the direction of traffic), the velocity can be calculated with the time interval between different sensors. With two sensors installed along the direction of traffic, the velocity can be obtained by dividing the distance with time interval of the two sensors, as shown in Eq. (17).

$$SP = \frac{D_{ij}}{T_j - T_i} \qquad \text{Eq.(17)}$$

where SP is the speed of the passing vehicle; D_{ij} is the longitudinal distance between the sensor i and j; T_i and T_j are the corresponding time coordinates for the same peak point in this fluctuation.

For example, sensor B1 and B10 were placed along the traffic direction, and the time interval between their fluctuations, shown in Figure 27, can be used to calculate the speed of the vehicle. System error might exist because of the installation, and can be adjusted by a system constant. Lots of runs were made, and the back calculated speeds were compared to the measurement of speed gun in Figure 28 for statistical analysis.

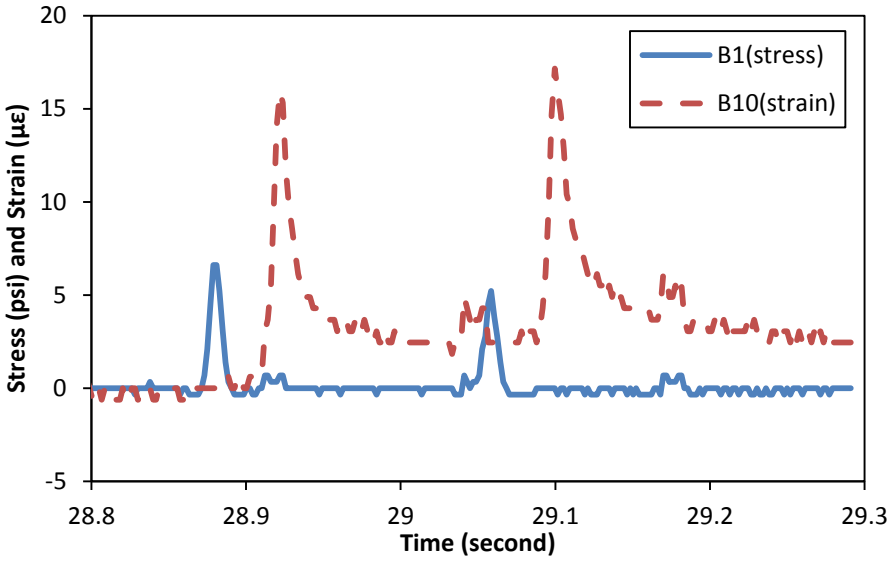

Figure 27: Traces of B1 and B10 for the same run.

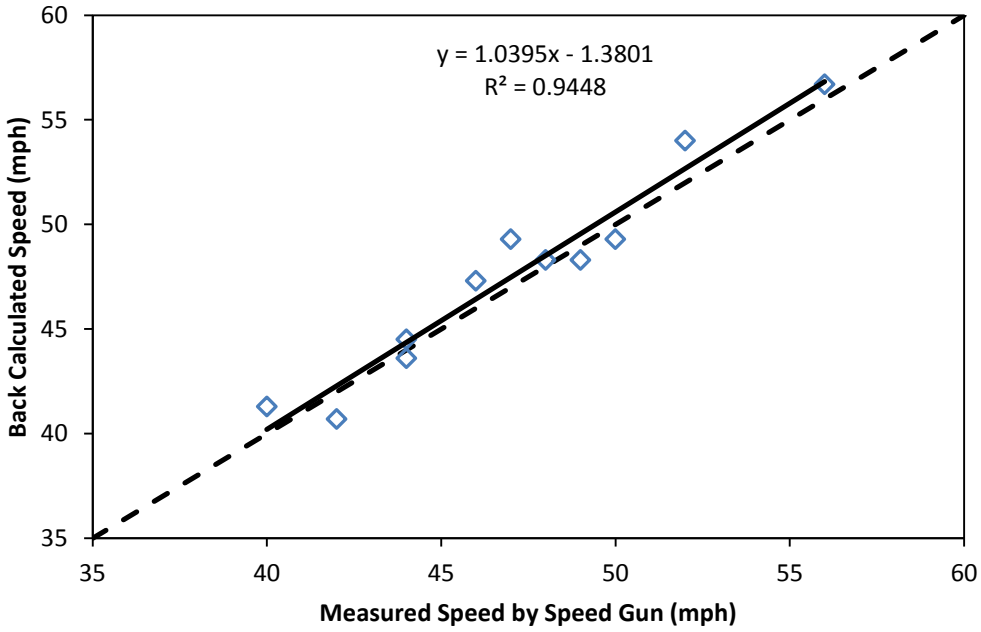

Figure 28: Back calculated speed compared with the measurement of speed gun.

NOTE: 1 mph = 1.61 km per hour

The calculated speed matched well with manual measurement with a speed gun. The deviation was understandable because the speed of actual traffic keeps changing all the

time, and error exists in the speed reading which is based on personal judgments. Other sources of error include the sensor installation, the streaming frequency of data collection, measuring error of the speed gun and so on.

Distance between Axles

With the speed of the passing vehicle known, the distances between the front and rear axles can be calculated with Eq. (18).

$$D_{axle} = SP \times (T_r - T_f) \qquad \text{Eq.(18)}$$

where D_{axle} is the distance between the front and rear axles of the vehicle; T_r and T_f are the time of the maximum tensile strain caused by rear and front tires.

The distance between axles were calculated for all the testing runs, and compared to the static manual measurements in Figure 29.

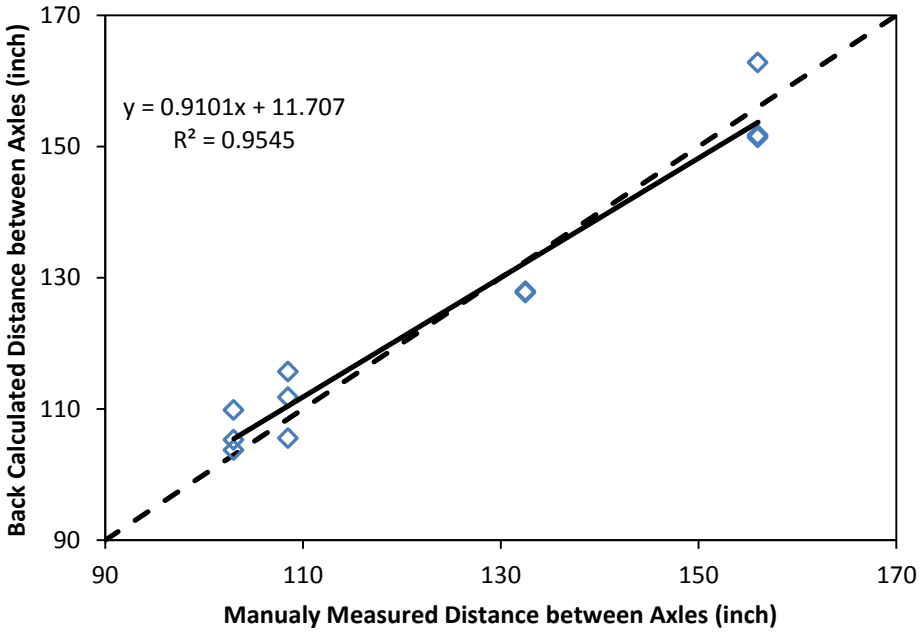

Figure 29: Back calculated distance between axles.

NOTE: 1 inch = 25.4 mm.

From the comparisons in Figure 29, the back calculated distance between axles was very accurate, and its distribution was very similar with back calculated speed. The dependency was understandable, because the calculation process is based on the speed results.

Spatial Distribution

In addition to temporal distribution, the spatial distribution of strain/stress signals can be analyzed for the other aspects, including offset distance, width of tire, wheel load and the distance between wheels. Spatial distribution analysis in this dissertation refers to the data analysis based on the signal collected at different transverse position (A5-A9, B5-B9).

Involved mechanical responses

As shown in Figure 13 in the chapter "Experiments", five kinds of sensing devices were installed in the pavement section, including thermal couples, moisture sensors, load cells, vertical and horizontal strain gauges. To study the spatial distribution of strain response, the 10 strain gauges placed in the direction of the traffic were used to detect the distribution of pavement strain responses via offset distance. To clarify the spatial positions of the ten horizontal strain gauges, related part of Figure 13 was enlarged and redrawn as in Figure 30.

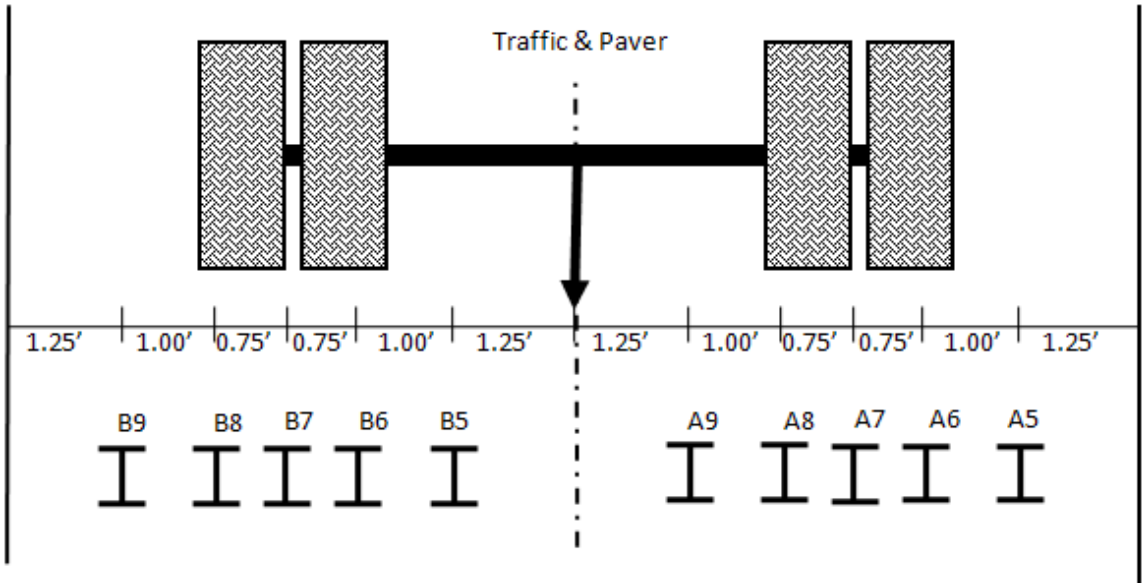

Figure 30: Layout of the sensing devices for spatial analysis.

The strain responses obtained from the five strain gauges distributed in each wheel path were different based on the wandering position of the wheel. The collected strain responses from sensor A5 to A9 in a normal testing run are displayed in Figure 31.

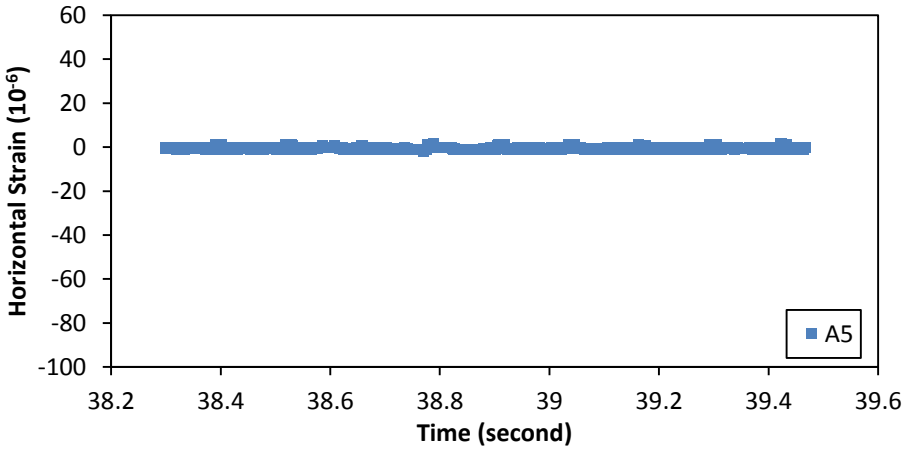

(a) Signals from horizontal strain gauge A5

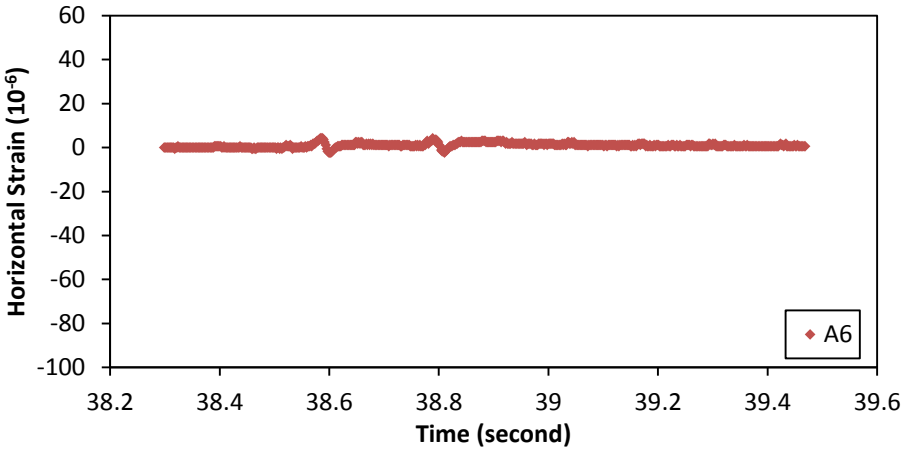

(b) Signals from horizontal strain gauge A6

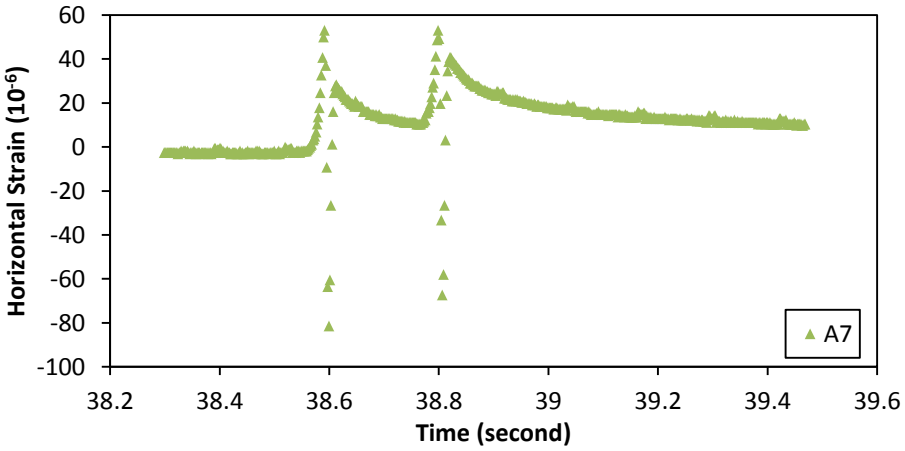

(c) Signals from horizontal strain gauge A7

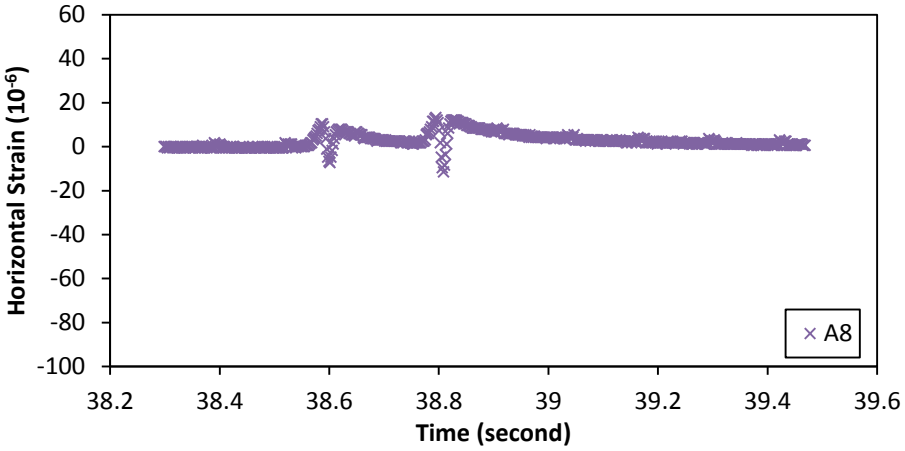

(d) Signals from horizontal strain gauge A8

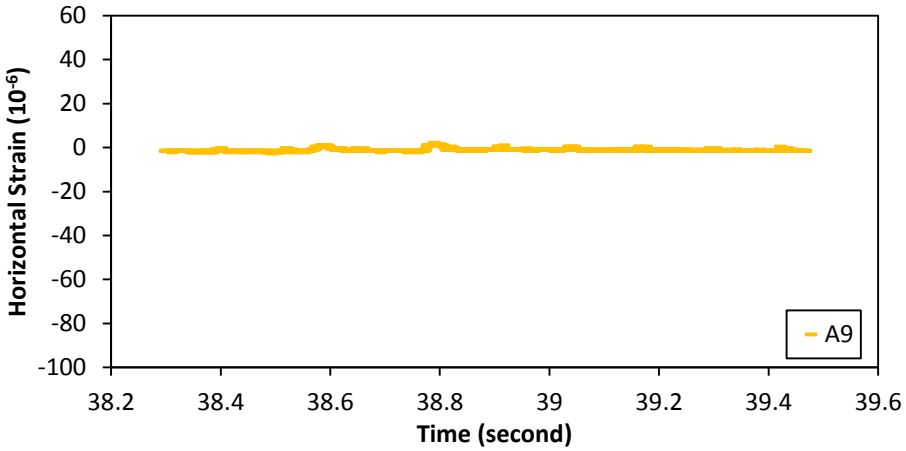

(e) Signals from horizontal strain gauge A9

Figure 31: Strain responses from horizontal strain gauges A5-A9.

Comparing the subfigures in Figure 31, the strain signal obtained by the strain gauge A7 was the strongest, followed by those from A6 and A8, and the signals from A5 and A9 were the weakest. Considering the spatial position of the gauges in Figure 30, the wheel probably passed the section close to the position of A7. The farther the strain gauge was from the wheel, the smaller the captured strain response was. At the same time, it was also found that the heavier the passing vehicle was, the bigger the captured strain responses were.

Based on the principles, efforts were made to estimate various information of passing vehicles based on the collected strain signals, as described in the following sections.

Simulation with Gaussian Function

When a vehicle passed by, every gauge recorded a strain trace corresponding to its location. Peak response was extracted from each trace for the following analysis. Without additional instructions, all the strain mentioned later refers to the measurement from sensor A5-A9 and B5-B9.

Considering only one tire moving across the instrumented section, the viscoelastic dynamic process was modeled with the Finite Element Method based software ABAQUS. The maximum strain response corresponding to each tire of the vehicle were measured in the first trial test runs, and compared with the corresponding numerical simulation in Figure 32.

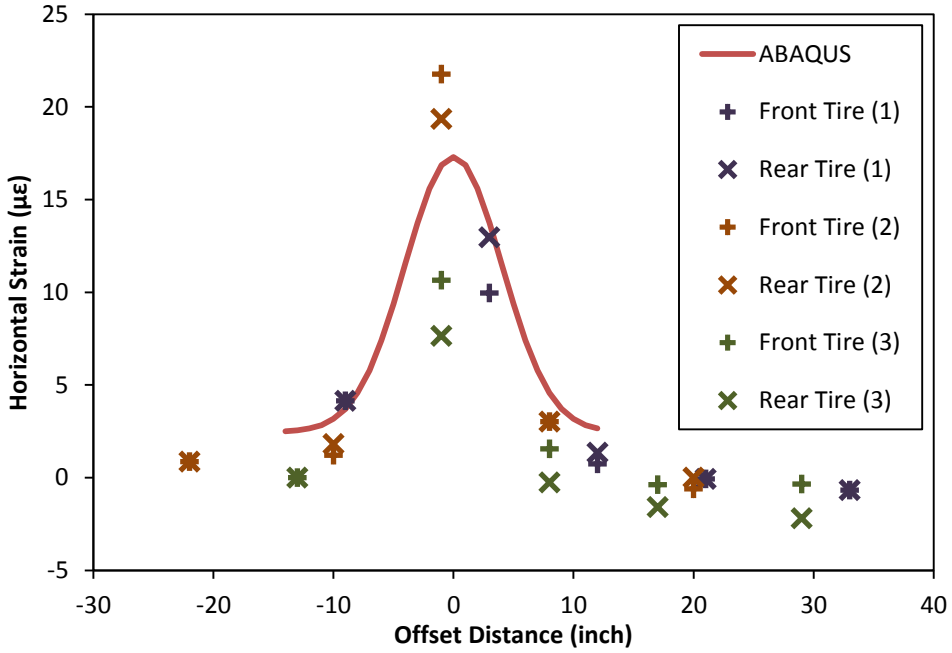

Figure 32: Comparison between ABAQUS calculation and measured horizontal strain.

NOTE: 1 inch = 25.4 mm.

As shown in Figure 32, the ABAQUS calculated responses matched the actual measurement well with some deviation. Considering the changing temperature and speed, the ABAQUS model worked quite well and will serve in the following analysis.

In the data analysis, it was found that the spatial distribution of the horizontal strain was similar to normal distributions, and Gaussian function was adopted to model the spatial distribution of horizontal strain as a result. With two additional parameters, A and b, the

original expression of normal distribution was modified to Eq.(19) to match the strain distribution better.

$$\varepsilon = \frac{A}{\sigma\sqrt{2\pi}} e^{-\frac{1}{2}\left(\frac{x-\mu}{\sigma}\right)^2} + b \quad \text{Eq.(19)}$$

where ε represent horizontal strain; A, μ, σ, and b are all the parameters which are going to be simulated by the SOLVER in EXCEL. These parameters have their specific meanings in the strain distribution of pavement:

- μ -- The distance between the center of the strain distribution and the reference line in the transverse plane, related to the wandering position of the passing tire;
- σ -- The width of the strain spread in pavement, related to the width of the passing tire;
- b -- The up and down shift of the whole strain distribution;
- A -- The area under the strain distribution curve when b=0.

As shown in Figure 32, the whole structure, not only the part under the tire, stand the total load. For simplification and efficiency, it is assumed that only the area [μ-3σ, μ+3σ] contribute to the load standing. Then another two integrated parameter L and s are defined as in Eq.(20-21):

$$L = A + 6\sigma b \quad \text{Eq.(20)}$$

$$s = b / A \quad \text{Eq.(21)}$$

where L represents the total area under the strain distribution curve between μ-3σ and μ+3σ, and is related to the load applied by the passing tire. The modified Gaussian distribution function can be expressed in Eq.(22).

$$f = \frac{L}{\sqrt{2\pi}\sigma(1+6\sigma s)} e^{-\frac{1}{2}\left(\frac{x-\mu}{\sigma}\right)^2} + \frac{Ls}{1+6\sigma s}, \qquad \text{Eq.(22)}$$

Replacing A and b with L=A+6b and s=b/A makes L the only parameter that represents the passing load. In this expression, lots of useful information about the passing vehicle can be obtained. The procedures necessary for Gaussian model include the follows.

- The five strain gauges across the wheel path record strain traces via time for each wheel of passing vehicles;
- Five peak points are extracted from traces and constitute a distribution curve for the wheel;
- Gaussian model is used to analyze each distribution curve in transverse plane and four parameters are obtained, which is used for the following back calculation.

To validate the specific meanings of Gaussian parameters, single tire passing process was modeled in ABAQUS with the different loading conditions. Each predicted strain distribution was simulated with Gaussian function separately, and the parameters were summarized in Table 9.

Table 9: Gaussian parameters of the strain distributions calculated in ABAQUS

Series	Load (lb)	Width of Loading Area (inch)	Offset Distance (inch)	L	σ	μ	s
1	5600	4	0	184.1	4.044	0.001	0.01644
2	6400	4	0	210.4	4.044	0.001	0.01643
3	7200	4	0	236.6	4.044	0.001	0.01643

4	6400	3	0	211.9	3.795	0.003	0.01741
5	6400	5	0	210.8	4.293	0.002	0.01460
6	6400	4	-1	209.9	4.010	-1.001	0.01709
7	6400	4	1	210.7	4.099	1.002	0.01514

18.1 ºC

Offset Distance – the transverse distance between the centerline of the loading area to the middle of the wheel path. It is positive when wheel is on the left side of wheel path.

As shown in Table 9, the Gaussian parameters related with their corresponding loading conditions closely. When the tire passed the experimental section at different wandering position (series 2, 6 and 7), the simulated parameter μ changed correspondingly, and the difference of other 3 parameters was neglectable. So the parameter μ might indicate the offset distance of the passing tire to the reference line.

Based on the comparison of series 2, 4 and 5, when the width of the loading area increased with other parameters constant, σ was the only parameter that has an obvious response. It could be assumed that σ represents the width of the loading area in the simulation.

According to the simulated parameter of series 1, 2 and 3, L increased linearly with load, and the other 3 parameters σ, μ, and s kept constant. The relationship between L and load is very important for weight back calculation.

In the experiment designed for traffic back-calculation, four different vehicles, as listed in Table 8, were used for test runs. Gaussian model was used to simulate the spatial distribution of strain responses in each run with the same procedures, and the simulated parameters of each test run were summarized in Table 10. These parameters are going to

be used for back calculation of vehicle configuration and axle load, as described in the following sections.

Table 10: Gaussian parameters of measured strain distributions

Run	Vehicle	Speed (mph)	Left Tire				Right Tire			
			L	σ	μ	*s*	*L*	σ	μ	*s*
1	1	42	688	5.43	-4.48	0.0013	749	4.21	-9.96	-0.0014
			774	5.62	-6.15	0.0007	826	4.59	-11.74	-0.0015
2	1	43	1080	4.69	7.68	-0.0010	608	4.82	4.01	-0.0017
			985	5.26	7.21	-0.0017	590	5.20	2.60	-0.0026
3	1	44	700	4.73	-3.42	-0.0003	840	4.02	-9.97	-0.0004
			640	4.94	-4.96	0.0001	750	3.89	-9.67	-0.0017
4	2	40	863	3.55	0.22	0.0039	556	4.00	3.10	0.0003
			425	2.60	1.12	0.0085	227	4.00	1.85	-0.0061
5	2	50	776	3.29	2.55	0.0045	655	2.90	5.16	0.0059
			417	3.03	2.81	0.0049	238	2.78	4.70	-0.0053
6	2	52	696	2.65	-4.29	0.0039	612	2.39	-3.93	0.0003
			377	2.34	-4.48	0.0069	328	2.17	-4.16	-0.0022
7	3	48	NA	NA	NA	NA	NA	NA	NA	NA
8	3	47	993	5.11	-9.56	0.0010	472	4.23	-9.56	-0.0004
			762	5.03	-9.91	0.0009	290	4.37	-10.00	-0.0023
9	3	48	610	3.99	-4.25	0.0037	733	4.22	-5.43	0.0002
			404	3.55	-4.53	0.0041	449	3.79	-6.43	-0.0010
10	4	53	544	4.87	-1.52	0.0014	311	4.78	-0.48	-0.0019
			282	4.33	-3.70	0.0040	262	5.19	-1.42	-0.0001
11	4	49	617	4.34	-0.97	0.0031	424	4.60	-1.41	-0.0003
			328	3.48	-3.33	0.0072	278	4.59	-0.62	-0.0025
12	4	40	728	3.64	-6.96	0.0040	416	3.30	-6.45	-0.0002
			606	4.68	-9.45	0.0027	418	4.67	-8.77	0.0025

NOTE: NA = not applicable, the signal is out of sensing range due to a big offset; 1 mph = 1.6 km per hour.

35~36°C

Wandering Position

Gaussian model was used in simulation based on the distribution of longitudinal horizontal strain, as shown in Figure 33. According to the simulated parameter μ, the tire passes the experimental section approximately 12 inch right of the centerline.

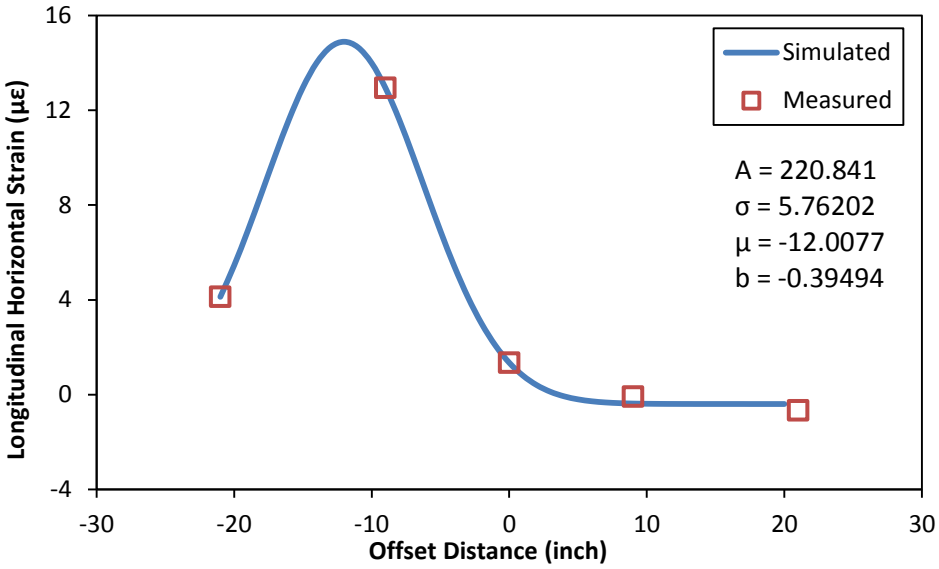

Figure 33: Simulation with Bell Curve model for a wheel load.

NOTE: 1 inch = 25.4 mm.

The wandering position calculated here might not be a parameter people care about as important information, but it is very important for the following back-calculation of vehicle configuration and axle load.

Distance between Wheels

Known the wandering position of the two wheels, the distance between wheels can be calculated as in Eq.(23).

$$D_{wheel} = 0.5WL + \mu_A - \mu_B, \qquad \text{Eq.(23)}$$

where D_{wheel} is the distance between the two wheels on the same axle; *WL* is the width of the lane, which is usually 144 inch; μ_A and μ_B is the calculated wandering position from gauge group A and B separately.

To verify the back calculation, the distance between the outer edges of the wheels was measured manually for each involved vehicle, as well as the distance between the wheel centers (as listed in Table 8). The measurements are compared to the back calculation results as shown in Figure 34.

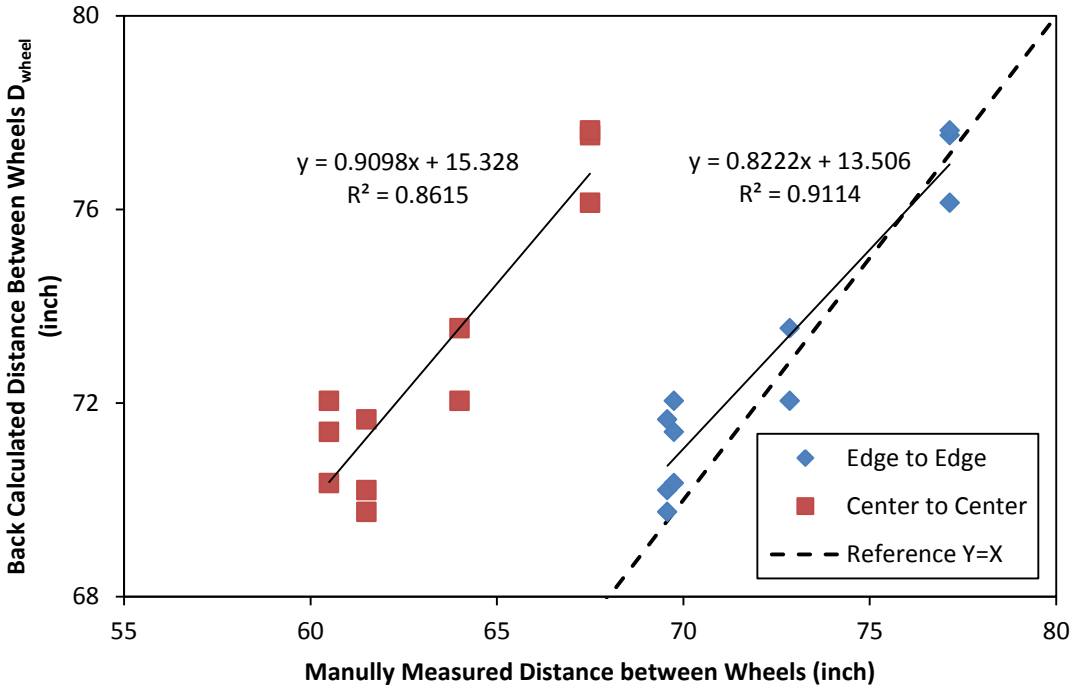

Figure 34: Back Calculated Distance between Wheels.

In the back calculation, the center of the strain distribution corresponds to the peak strain response in pavement, and the distance between the left and right centers is called the distance between wheels. As shown in Figure 34, the back calculated distances between wheels matched in magnitude with the measurement between outer edges of the tires, not

the centers of the tires. It was because that the pressure distribution under the tire was not uniform, and the outer edge applied the most pressure to pavement.

Width of the tire

The parameter σ of the bell curve model, which controls the shape of the bell curve, was assumed to be correlated with the width of the tire. The calculated parameter σ presented a second order polynomial relationship with the corresponding tire width in Figure 35.

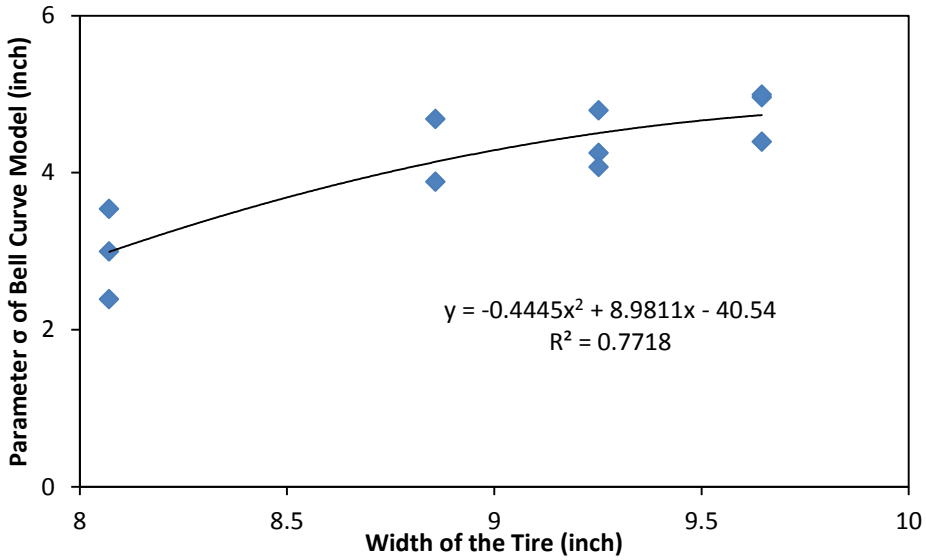

Figure 35: Back calculated parameter σ and the width of corresponding tire.

As shown in Figure 35, the simulated parameter σ had a relationship with the actual width of tire. As a result, parameter σ could be used to estimate the tire width for passing vehicles. The variation in Figure 35 was probably because that the number of sensors in transverse plane was limited. At the same time, the contact area between tire and pavement changes with speed and temperature, which promoted the variation in back-calculation.

Weight

The weight of the passing vehicle is one primary objective of this project, and the monitoring system is expected to work as a Weigh-In-Motion system. As assumed in Gaussian model, the parameter L defined in Eq. (20) represents the passing load, and increases linearly with increasing load when the other loading conditions and environmental conditions keep constant.

In one experiment, the temperature of pavement changed in the small range between 35 and 36 Degree Celsius which was neglected in the comparison. The sum of back calculated parameter L ($\sum L$) was calculated for each passing vehicle, and summarized in Figure 36 with the corresponding weight.

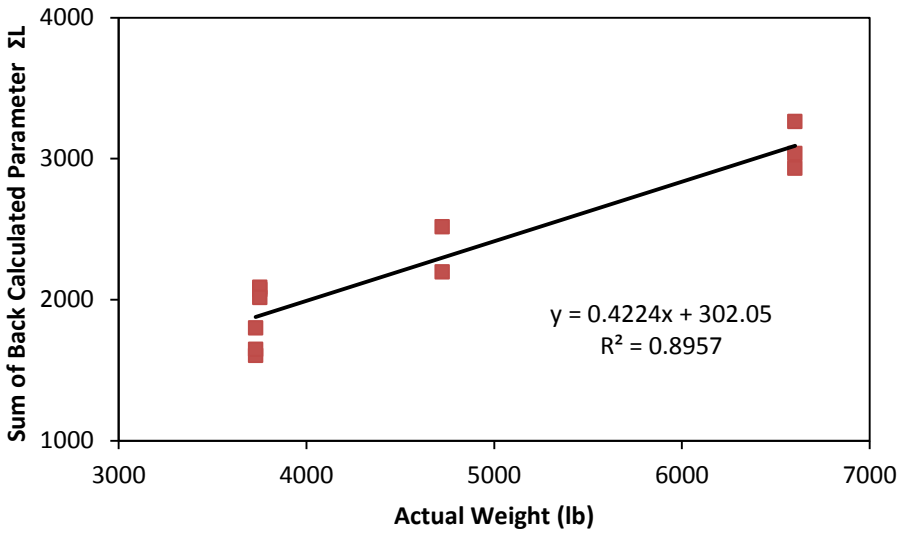

Figure 36: Back calculated $\sum L$ and the weight of corresponding vehicle

As shown in Figure 36, when temperature stayed constant, $\sum L$ increased linearly with the actual weight of vehicles. Based on the linear relationship between $\sum L$ and vehicle weight, the back calculation of weight is simplified into Eq. (24-25).

$$Wheel\ Load = CF \cdot R \cdot L \quad \text{Eq.(24)}$$

$$Weight = \sum Wheel\ Load_i \quad \text{Eq.(25)}$$

Where *R* is the ratio between the wheel load and parameter *L* in ABAQUS, and *CF* is the factor to correct the difference between theoretical calculation and actual application.

For example, the temperature was 18.1°C in the experiment, *R* was calculated to be 7.607 from Table 9, and *CF* was 0.7886 from the regression of on-site calibration as in Figure 36. Back calculated wheel load of Vehicle #1 were summarized in Table 11.

Table 11: Back Calculated Wheel Load of Testing Vehicle #1 (lb)

	Front Tires		Rear Tires		Total
	Left	Right	Left	Right	
Run #1	1,795.1	1,021.2	2,574.7	1,242.9	6,633.8
Run #2	1,795.5	1,358.0	2,141.3	1,198.2	6,493.0
Run #3	2,492.2	715.4	2,760.2	465.3	6,433.1

As seen in Table 11, the load distribution over the four tires of the moving vehicle changed with a big turbulence in the test runs. However, the calculated total weight still wandered around the actual weight 6520 lb (vehicles' weight plus one driver), which validates the Weigh-In-Motion function of this monitoring system again.

Traffic Monitoring System Prototype

The analysis above mainly talks about back-calculating various information of the passing traffic with pavement strain responses for the purpose of traffic monitoring. As a summary, as in Figure 37 describes the prototype of this monitoring system.

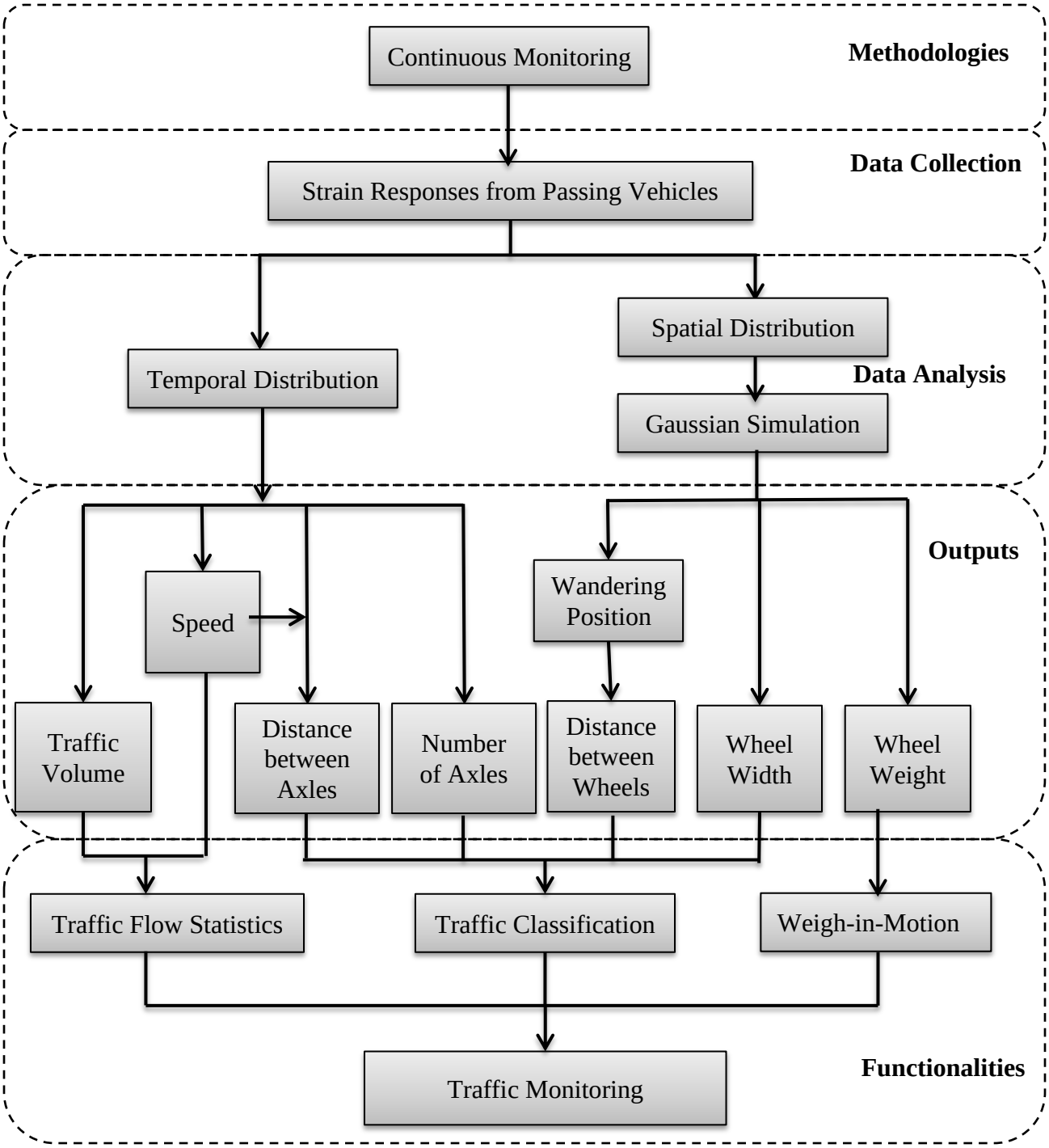

Figure 37: Prototype of the Traffic Monitoring System

As described in Figure 37, this traffic monitoring system is going to collect the strain responses from each passing vehicle continuously in the real-time monitoring. The

pavement responses can be analyzed in time domain. The number of axles for each vehicle and the total traffic volume can be obtained by counting and grouping the signal fluctuations. The speed of each passing vehicle can be estimated based on the time interval between sensors distributed in the direction of traffic. Known the speed, the distance between axles of each vehicle can be calculated by the time interval between the strain responses of different axles.

The spatial distribution of strain responses can also provide lots of important information for the passing vehicle. Based on the observations in experiments, pavement strain response distributes in a shape of bell, and Gaussian function can be used to simulate its distribution conveniently. The parameters representing the wandering position, tire width and wheel load of the passing vehicle can be obtained from the simulation, and the distance between wheels can be easily back-calculated with the wandering position of the left and the right wheel.

The combination of temporal and spatial distribution analysis provides this traffic monitoring system multiple valuable functionalities. The function of traffic flow statistics is achieved by recording the traffic volume and average speed. The function of traffic classification is achieved with various configuration parameter of each passing vehicle. The function of Weigh-in-Motion can be achieved with the load on every wheel estimated.

Discussion and Conclusion

In the process of traffic monitoring, the collected responses were analyzed for various information of passing vehicles. All the analysis could be categorized into two groups: temporal distribution and spatial distribution, according to the analysis methodology.

The analysis of temporal distribution was based on the data distribution in time field. The strain response fluctuations were counted for the number of passing axles, and the compacted fluctuations were grouped and recognized as one vehicle. The number of fluctuations in each group was treated as the number of axles of the vehicle, and the number of groups was treated as the number of the passed vehicles. This counting method was verified with field observations and video records many times, and proved to be reliable and accurate.

The speed of the passing vehicle can also be back-calculated with similar methodology. Since the distance between sensors was fixed, and the speed can be back-calculated based on the time interval between different sensors. The difference between back-calculated speed and speed gun measurements was understandable because that the measurement of speed gun had a standard deviation of 1 mph. And error might also be induced by improper speed gun reading, inaccurate sensor installation, and low frequency of data collecting, and so on.

With known time interval between axles and the back-calculated speed, the distance between axles can be calculated easily. Because the passing process was dynamic, some errors existed in the final result within a reasonable range.

According to collected signal, the maximum strain response distributed in a bell-shaped curve in the transverse plane. Based on the shape and magnitude of the curve, many parameters of the passing vehicles can be back-calculated, which is called spatial distribution analysis in this dissertation.

Viscoelastic pavement loading processes modeled in ABAQUS and the simulated strain distribution matched with measured data in experiment well in the trend (Figure 32). The deviation was understandable for a viscoelastic dynamic loading process on asphalt concrete. The ABAQUS viscoelastic model was proved to be reliable for pavement response simulation under moving loads.

Gaussian Model was used to simulate the spatial distribution of horizontal strain. The designed parameters in the model were assumed to be related with some parameters of passing load, including wheel load, width of tire, and passing offset distance. The parameter μ corresponds to offset of the maximum strain response for each tire. The distance between wheels can be calculated according to the offset of the tires on the same axle. The parameter σ presents a second order polynomial relationship with the tire width. The parameter L, which is actually the area under Gaussian function, was proved to be related to the wheel load.

Gaussian Model is verified in ABAQUS with changing offset distance, contact area and applied load, and the parameters presented expected relationships with passing load (Figure 32). The back calculations method also showed good performance in On-site testing with different vehicles. The verifications with both ABAQUS and on-site testing made the Gaussian Model more convincing.

A prototype of back calculation method was provided, and can be used to collect the weight, speed and configuration of passing vehicles only with ten normal strain gauges in pavement. Gaussian function was used to model the horizontal strain distribution via offset distance, and the simulated parameter of Gaussian function was correlated to weight and configuration parameters of passing vehicles directly.

This method provides the potential of integrated transportation monitoring system, which can monitor both the pavement health status and information of passing traffic. At the same time, the simple and efficient back calculation procedures make the real time monitoring convenient and efficient.

However, the experiment and the back calculation present in this paper were limited in many aspects by time, funding, experience, and circumstances.

- The number of sensor was limited, and both the accuracy of the calculation and the reliability of the monitoring system were affected;
- Sample size was small. More testing results would make the back calculation more convincing;
- Testing vehicle were all family cars, without heavy loaded truck;
- The strain distribution in vehicle direction should be also taken into the back calculation of wheel load to improve the accuracy and integrity of the method;
- The relationship between correction factor (*CF*) and other factors, including pavement structure, temperature, other loading and environmental factors.

EFFECT OF TEMPERATURE AND SPEED

As described in the former chapters, various mechanical responses in pavement can be analyzed to track the pavement health status and back-calculate various loading information. All the previous numerical simulations were based on the viscoelastic theory, but under almost similar temperature and speed. However, temperature and vehicle's speed are changing all the time in the real-time monitoring process, and it is important to understand the effect of temperature on the relationships between simulated parameters of Bell Curve Model and corresponding loading parameters.

In general, temperature and vehicle's speed, which is also loading rate, change the modulus of asphalt concrete based on viscoelastic theory. The changing modulus of asphalt concrete can affect the magnitude of strain response traces, but not the shape of strain distribution via time. As a result, some parameters including speed, wandering position and distances between axles and wheels, which are calculated based on the distribution of strain responses instead of magnitude, will not be affected. The back calculated load is totally based on magnitude of strain response, and will definitely be affected by temperature and loading rate theoretically. The width of the tire is based on the strain spread rate throughout the pavement, and might be affected potentially.

Linear Viscoelasticity Theory

The material characteristic of asphalt concrete is very complicated because of its complex constitution. In normal temperature range, it is believed that asphalt concrete mainly

presents a linear viscoelastic property. Both temperature and loading frequency affect the modulus of the pavement.

Mechanical Model

The behavior of viscoelastic materials closely resembles that of models built from discrete elastic and viscous elements. Two basic elements are involved in viscoelastic models: spring and dashpot, corresponding to elastic and viscous material separately. For a helical spring, the length increases by a certain amount u when a force P applied, and returns to its original length when the force removed. Linear-elastic material can be represented with the same relationship, which is called Hooke's law (Eq.(26)):

$$\sigma = E\varepsilon, \qquad \text{Eq.(26)}$$

where σ is stress; ε is strain, and E is Young's modulus.

Dashpot can be treated as a mechanical model of moving a piston in a cylinder with a perforated bottom. There is a rather viscous lubricant between the cylinder and the piston wall, and a force P is needed to displace the piston. The stronger this force, the faster the piston will move. Assuming the relation between force and the moving speed is linear, the function of strain and stress can be derived as in Eq.(27):

$$\sigma = \eta \frac{d\varepsilon}{dt} = \eta\dot{\varepsilon}, \qquad \text{Eq.(27)}$$

where the quantity $\dot{\varepsilon}$ is the partial derivatives of strain with respect to time t, called the strain rate. A material whose stress is proportional to the strain rate is called a viscous material.

The behavior of viscoelastic materials is a mixture of simple cases with springs and dashpots. More complicated models can be built up combining springs and dashpots to simulate various viscoelastic materials.

One basic model is Maxwell material, in which spring and dashpot are connected in series, as shown in Figure 38.

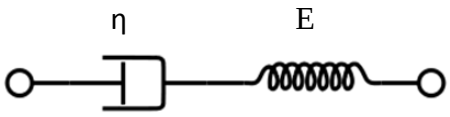

Figure 38: Spring and dashpot in series: Maxwell material

In this case, the force is the same for both the spring and the dashpot, and elongation ε is split into the extension of the spring ε' and the extension of the dashpot ε''.

$$\sigma = E\varepsilon', \quad \text{Eq.(28)}$$

$$\sigma = \eta\dot{\varepsilon''} \quad \text{Eq.(29)}$$

$$\varepsilon = \varepsilon' + \varepsilon'' \quad \text{Eq.(30)}$$

ε' and ε'' are differentiated and introduced into the total elongation ε for the relationship between σ and ε.

$$\dot{\varepsilon} = \dot{\varepsilon'} + \dot{\varepsilon''} = \frac{\dot{\sigma}}{E} + \frac{\sigma}{\eta} \quad \text{Eq.(31)}$$

As a result, the constitutive equation of Maxwell material is:

$$\sigma + \frac{\eta}{E}\dot{\sigma} = \eta\dot{\varepsilon}. \quad \text{Eq.(32)}$$

Another basic model is Kelvin material, in which spring and dashpot are displayed parallel to resist force, as shown in Figure 39.

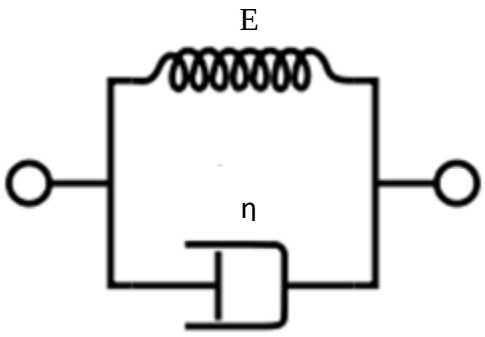

Figure 39: Spring and dashpot parallel: Kelvin material

In this case, the elongation ε of the two elements is the same, and the total force σ will be split into σ' (spring) and σ'' (dashpot) in whichever way it is necessary to make ε the same.

$$\sigma' = E\varepsilon, \qquad \text{Eq.(33)}$$

$$\sigma'' = \eta\dot{\varepsilon}, \qquad \text{Eq.(34)}$$

$$\sigma = \sigma' + \sigma'' = E\varepsilon + \eta\dot{\varepsilon} \qquad \text{Eq.(35)}$$

As a result, the equation above is the constitution equation of Kelvin material.

Both Maxwell and Kelvin materials are basic models, and only simulate simple viscoelastic properties. Asphalt concrete is a complicated composite material, and is usually represented with a generalized Maxwell model (as shown in Figure 40); spring and dashpot mechanical analog.

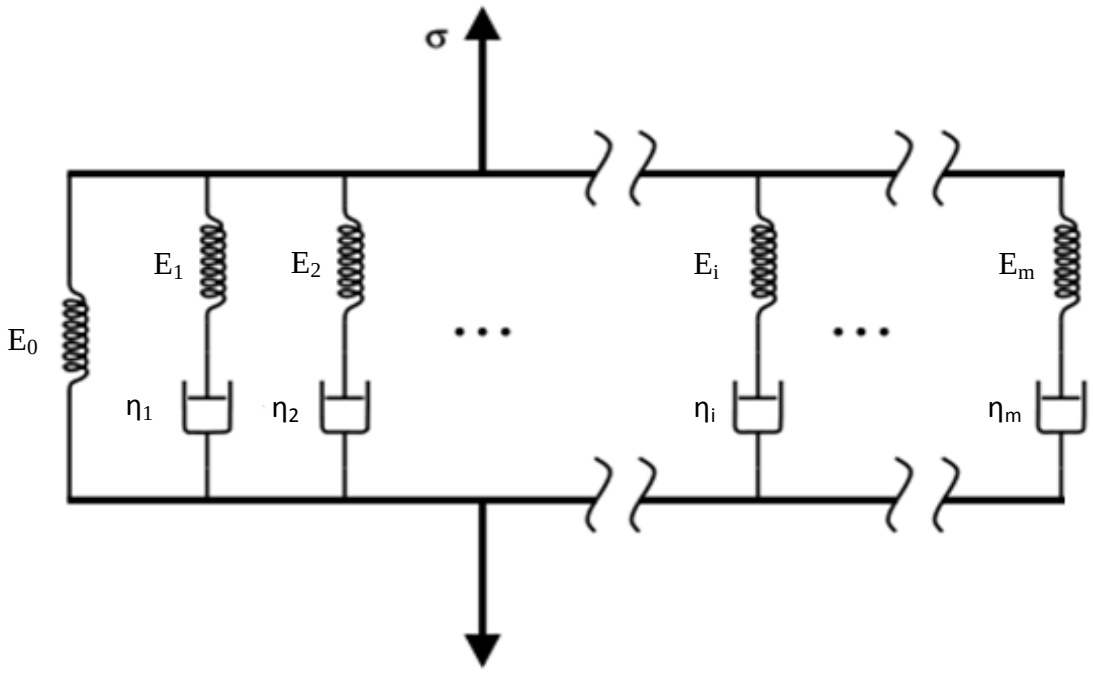

Figure 40: Generalized Maxwell model

The Generalized Maxwell model, also known as the Maxwell-Wiechert model is the most general form of the linear model for viscoelasticity. It takes into account that the relaxation does not occur at a single time, but at a distribution of time, shown in the model by the spring-dashpot Maxwell models. The material constants E_i and η_i correspond respectively to the stiffness of each Maxwell spring and the viscosity of each dashpot.

The Generalized Maxwell model can be analyzed with Prony's method, which extracts valuable information from a uniformly sampled signal and builds a series of damped complex exponentials or sinusoids for the estimation of frequency, amplitude, phase and damping component, called Prony series. The Prony series for Generalized Maxwell

model usually include two series of parameters: the elastic stiffness E_i and the relaxation time ρ_i.

$$\rho_i = \frac{\eta_i}{E_i} \qquad \text{Eq.(36)}$$

The Prony series are going to be used in the following section for viscoelastic properties.

Laboratory Tests

The viscoelastic property of asphalt concrete can be evaluated by many laboratory tests, which can be categorized into two groups originally: static and dynamic tests. In a static test, a static axial loading (strain/stress) is applied to a specimen for a fixed period of time during which the other corresponding mechanical response (stress/strain) is continuously monitored. The axial loading is then removed and both the permanent and recovered response determined.

Investigations have shown that the dynamic tests correlate better with in-service pavement performance than static methods. Static testing method is not included in the latest European standard and does not feature in current American standards. As a result, only dynamic testing methods are described in this section, including creep, relaxation and repeated pulse tests. These dynamic tests use the samples taken from experimental sections, control stress/strain response of the sample by changing and repeating load, and measure the other response strain/stress. The relationship between strain and stress can be used to evaluate the viscoelasticity of the sample.

Based on the controlled strain/stress loading on specimen, the dynamic testing for viscoelastic characterization of asphalt concrete can be grouped into relaxation, creep, and general repeated loading test. Relaxation test methods cover the determination of the time dependence of stress in materials and structures under conditions of approximately constant constraint, constant environment, and negligible vibration. In relaxation test methods, the material is subjected to a sudden strain that is kept constant over the duration of the test, and the stress is measured over time. The initial stress is due to the elastic response of the material. Then, the stress relaxes over time due to the viscous effects in the material.

Creep tests cover the determination of the amount of deformation as a function of time (creep test) when under constant forces at constant temperature. In creep test methods, the material is subjected to a sudden force that is kept constant over the duration of the test, and the strain is measured overtime. The initial strain is due to the elastic response of the material, and the strain overtime is dependent on the creep compliance of the material.

General repeated load tests refer to the tests applying repeated load to specimen at certain frequency pattern, including simple repeated load test, dynamic modulus test and other tests. A simple repeated load test applies a repeated load of fixed magnitude and cycle duration to specimen followed by a rest period. Cumulative permanent deformation is recorded as a function of the number of load cycles which is correlated to rutting potential. Tests can be run at different temperature and varying loads. Dynamic modulus tests apply a repeated axial cyclic load of fixed magnitude and cycle duration to a test

specimen at different temperatures and different loading frequencies and measures a specimen's stress-strain relationship. The applied load varies and is usually applied in a haversine wave. The difference between simple repeated load test and dynamic modulus tests include: the loading frequency in simple repeated load test is fixed and dynamic modulus tests apply a load over a range of frequencies. The dynamic modulus test is more difficult to perform than the simple repeated load test since a much more accurate deformation measuring system is necessary.

Viscoelastic Properties

The generalized Maxwell model consists of a spring and m Maxwell elements connected in parallel. The relaxation modulus derived from this model is given in Eq.(37)

$$E(t) = E_0 + \sum_{i=1}^{m} E_i e^{-\frac{t}{\rho_i}} \qquad \text{Eq.(37)}$$

where E_0 is the long time equilibrium modulus, E_i is the elastic stiffness of each Maxwell spring; ρ_i is the relaxation time of each Maxwell dashpot. The series of E_i and ρ_i are often referred as Prony series.

The creep compliance can be characterized more easily using the generalized Voigt model (Kelvin model) which consists of a spring, a dashpot and n Voigt elements (Kelvin model) connected in series. For viscoelastic solid, the creep compliance can be present as in Eq.(38).

$$D(t) = D_0 + \sum_{j=1}^{m} D_j \left(1 - e^{-\frac{t}{\tau_j}}\right) \qquad \text{Eq.(38)}$$

where D_0 is the initial or glassy compliance, D_j and τ_j are the creep compliance and the retardation of each Voigt element.

The dynamic modulus E^* or D^* (also called the complex modulus) is a commonly measured property of asphalt concrete. It is measured by applying a haversine axial loading at various frequencies$\omega = 2\pi f$ on testing samples. The amplitude of the dynamic compressive stress and a constant contact stress are set based on the material stiffness and experiment targets. The resultant viscoelastic strain response lags behind the stress in time expressed in terms of a phase angle ϕ. The dynamic modulus amplitude $|E^*|$ is calculated as the ratio between the peak dynamic stress and peak dynamic strain[68]. The storage modulus E' and loss modulus E'' are the real and imaginary components of the complex modulus:

$$E'(\omega) = |E^*(\omega)| \cdot \cos \phi(\omega) \quad \text{Eq.(39)}$$

$$E''(\omega) = |E^*(\omega)| \cdot \sin \phi(\omega) \quad \text{Eq.(40)}$$

$$E^*(\omega) \equiv E'(\omega) + iE''(\omega) \quad \text{Eq.(41)}$$

The real and imaginary parts of complex modulus can also be written with creep compliances as in Eq.(42-43):

$$D^*(\omega) \equiv D'(\omega) - iD''(\omega) \quad \text{Eq.(42)}$$

$$E^*(\omega)D^*(\omega) = 1 \quad \text{Eq.(43)}$$

Both the storage and loss moduli of dynamic modulus E^* or D^* can be expressed with Prony series as in Eq.(44-47):

$$E'(\omega) = E_0 + \sum_{i=1}^{m} \frac{\omega^2 \rho_i^2 E_i}{1 + \omega^2 \rho_i^2} \quad \text{Eq.(44)}$$

$$E''(\omega) = \sum_{i=1}^{m} \frac{\omega \rho_i E_i}{1 + \omega^2 \rho_i^2} \quad \text{Eq.(45)}$$

$$D'(\omega) = D_0 + \sum_{j=1}^{m} \frac{D_j}{1 + \omega^2 \tau_j^2} \quad \text{Eq.(46)}$$

$$D''(\omega) = \sum_{j=1}^{m} \frac{\omega \tau_j D_j}{1 + \omega^2 \tau_j^2} \quad \text{Eq.(47)}$$

Complex modulus, relaxation modulus and creep compliance are all related for a given underlying material model (generalized Maxwell model), and all can be represented by Prony series. Once any of them is determined from corresponding viscoelastic test, the other viscoelastic properties can be calculated with the known Prony series. Park and Schapery provided detailed process of the inter-conversion with Prony series [69].

For the transient functions, the following function can be used to determine the relaxation modulus from a known creep compliance or vice versa by approximate analytical or numerical methods.

$$\int_0^t E(t-\tau) \frac{dD(\tau)}{d\tau} d\tau = 1 \quad (t > 0) \quad \text{Eq.(48)}$$

"When one set of constants, either $\{\rho_i, E_i (i = 1, \dots, m), E_0\}$ or $\{\tau_j, D_j (j = 1, \dots, m), D_0\}$ is known and target time constants are specified, the other (unknown) set of constants can

be determined simply by solving the resulting system of linear algebraic equations". $D_j (j = 1, \dots, m)$ can be calculated from Eq.(49-51).

$$[A]\{D\} = \{B\} \quad \text{Eq.(49)}$$

$$A_{kj} = \begin{cases} E_0\left(1 - e^{-t_k/\tau_j}\right) + \sum_{i=1}^{m} \frac{\rho_i E_i}{\rho_i - \tau_j}\left(e^{-t_k/\rho_i} - e^{-t_k/\tau_j}\right) & \text{when } \rho_i \neq \tau_j \\ E_0\left(1 - e^{-t_k/\tau_j}\right) + \sum_{i=1}^{m} \frac{t_k E_i}{\tau_j} e^{-t_k/\tau_j} & \text{when } \rho_i = \tau_j \end{cases} \quad \text{Eq.(50)}$$

$$B_k = 1 - \left(E_0 + \sum_{i=1}^{m} E_i e^{-\frac{t}{\rho_i}}\right) \Big/ E_0 + \sum_{i=1}^{m} E_i \quad \text{Eq.(51)}$$

For the viscoelastic properties in the frequency domain, the inter-conversion can be done based on the real and imaginary part presentation of complex modulus via relaxation modulus and creep compliance, as shown in Eq.(52).

$$D' = \frac{E'}{(E')^2 + (E'')^2} \quad \text{Eq.(52)}$$

Once D' is determined, D'' can be easily established. The equation system is similar as for the transient functions with the following A_{kj} and B_k:

$$A_{kj} = \frac{1}{\omega_k^2 \tau_j^2 + 1} \quad \text{Eq.(53)}$$

$$B_k = \frac{E_0 + \sum_{i=1}^{m} \frac{\omega_k^2 \rho_i^2 E_i}{1 + \omega^2 \rho_i^2}}{\left(E_0 + \sum_{i=1}^{m} \frac{\omega_k^2 \rho_i^2 E_i}{1 + \omega^2 \rho_i^2}\right)^2 + \left(\sum_{i=1}^{m} \frac{\omega_k \rho_i E_i}{1 + \omega^2 \rho_i^2}\right)^2} - \frac{1}{E_0 + \sum_{i=1}^{m} E_i} \quad \text{Eq.(54)}$$

where ω_k is a discrete value of the angular frequency at which the interrelationship is established.

Time-Temperature Superposition Principle

The viscoelastic properties of many materials can be described over a range of temperatures by means of a master curve and a temperature ship factor relationship using the time-temperature superposition principle."[68] The master curves of complex modulus can be developed from test data at different temperatures by shifting the data along the time or frequency axis to form a single master curve. An arbitrary reference temperature is necessary, toward which the data from other temperatures are shifted the shifted material properties is a function of only reduced time or reduced frequency, and not dependent on time/frequency and temperature any more. The reduced frequency and the reduced time are defined as in Eq.(55-56).

$$\omega_R = \omega \times \alpha(T) \qquad \text{Eq.(55)}$$

$$t_R = \frac{t}{\alpha(T)} \qquad \text{Eq.(56)}$$

where ω is the actual loading frequency, $\alpha(T)$ is temperature shift factor, T is temperature, $\omega(R)$ is reduced frequency; t is the actual loading time, t_R is reduced time.

Numerical Simulation

Numerical Model

To study the effect of temperature and speed on pavement strain response, Finite Element Method based software ABAQUS was used to simulate the wheel passing process. The

wheel path section (half of the lane, 6 feet wide) was modeled with rectangular element C3D8R, and the length of the numerical model was set to be 100 inch. The thickness of the top layer of asphalt concrete was 4 inch, and the element size was 1 inch × 1 inch × 1 inch. The thickness of the sub-layer was 8 inch, and the element size was 2 inch × 2 inch × 2 inch. The configuration of the numerical model is shown in Figure 41.

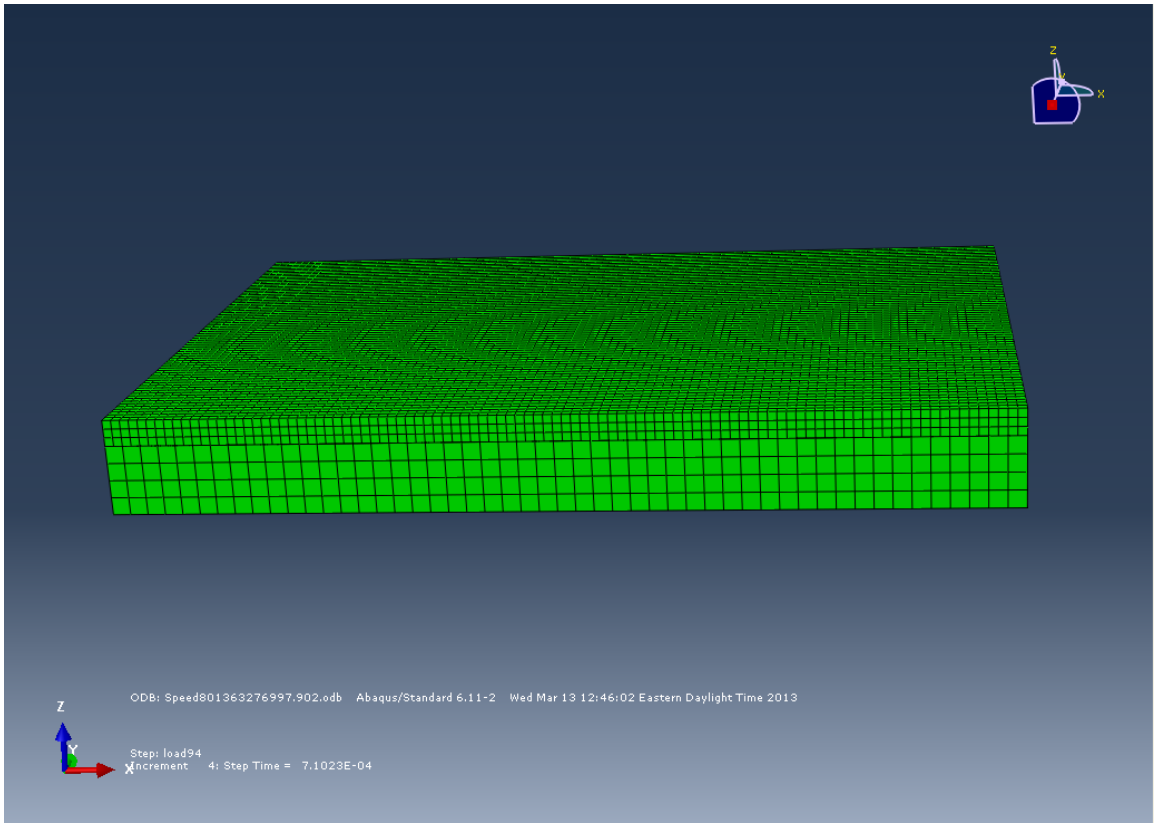

Figure 41: Configuration of the ABAQUS model

In the ABAQUS model, the asphalt concrete layer was treated as linear viscoelastic material, and characterized by Prony series and Williams-Landel-Ferry equation in ABAQUS. The Williams-Landel-Ferry equation (WLF), present in Eq.(57), is an empirical equation associated to time-temperature superposition. The equation can be used to fit discrete value of the shift factor α_T vs. temperature.

$$\log(\alpha_T) = \frac{-C_1(T - T_r)}{C_2 + (T - T_r)} \quad \text{Eq.(57)}$$

where T_r is the reference temperature chosen to construct the compliance master curve and C_1, C_2 are empirical constants adjusted to fit the values of α_T. The Prony series and the WLF shift function used are listed in Table 12, which were both calculated from the dynamic modulus test results provided by Virginia DOT, as attached in Appendix D.

Table 12: Viscoelasticity of the asphalt concrete in Virginia Route 114.

Prony Series					
Rank	E_i (psi)	ρ_i (s)	Rank	E_i (psi)	ρ_i (s)
0	4.66E+01				
1	2.64E+05	1.E-05	14	9.06E+04	3.E+01
2	2.94E+05	3.E-05	15	0.00E+00	1.E+02
3	3.30E+05	1.E-04	16	2.77E+04	3.E+02
4	3.52E+05	3.E-04	17	1.67E+04	1.E+03
5	3.86E+05	1.E-03	18	4.89E+03	3.E+03
6	3.98E+05	3.E-03	19	9.42E+03	1.E+04
7	3.33E+05	1.E-02	20	2.98E+03	3.E+04
8	1.16E+05	3.E-02	21	2.19E+03	1.E+05
9	0.00E+00	1.E-01	22	8.27E+03	3.E+05
10	8.53E+05	3.E-01	23	4.75E+03	1.E+06
11	0.00E+00	1.E+00	24	6.72E+02	3.E+06
12	0.00E+00	3.E+00	25	2.55E+03	1.E+07
13	1.17E+05	1.E+01	26	9.77E+03	3.E+07

WLF Equation Parameters		
T_r (^{0}C)	C_1	C_2
21.11	30.35	253.36

Loading Process

In the loading process, a wheel was assumed to roll across the simulated pavement section. The contact area was simulated by a group of element surface according to the position of the wheel in each step, on which the distributed pressure 80 psi was applied on. There were 94 steps for the wheel rolling across the section, and the pavement strain responses changed with the position of the contact area, as shown in Figure 42. In fact, since the all the loading and environmental conditions kept constant in the whole process, various pavement responses also kept constant with regard to the current position of the wheel. As a result, only the pavement responses corresponding to the step 48 (the wheel is in the middle of the simulated section) were extracted. The stress and displacement responses changed in the same way as strain, and the corresponding stress and displacement responses for step 48 are shown in Figure 43.

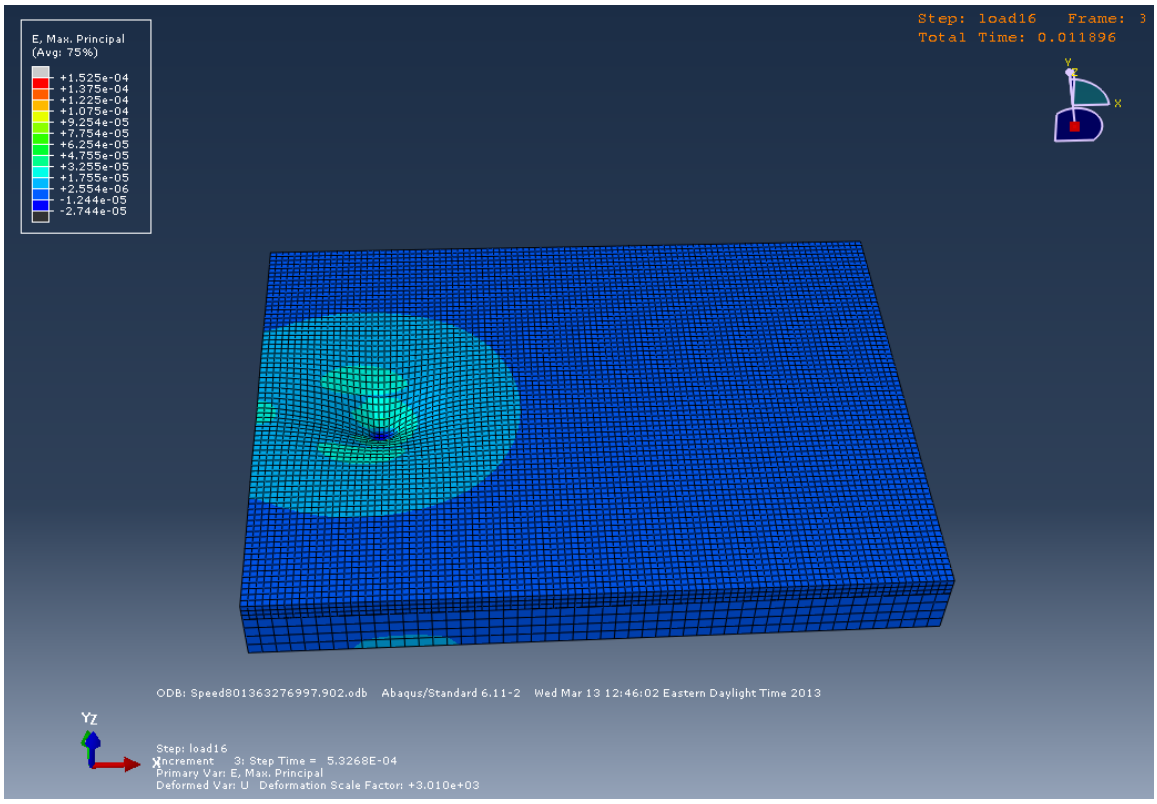

(a) On the left of the section

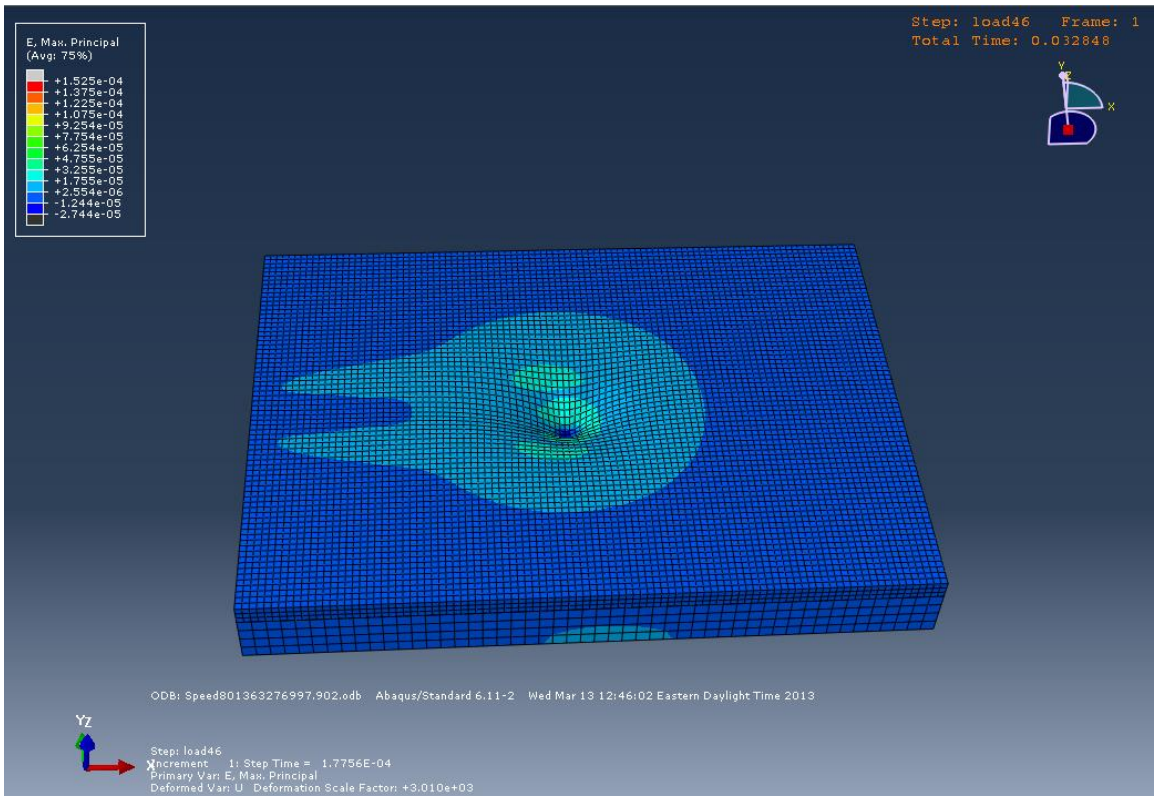

(b) In the middle of the section

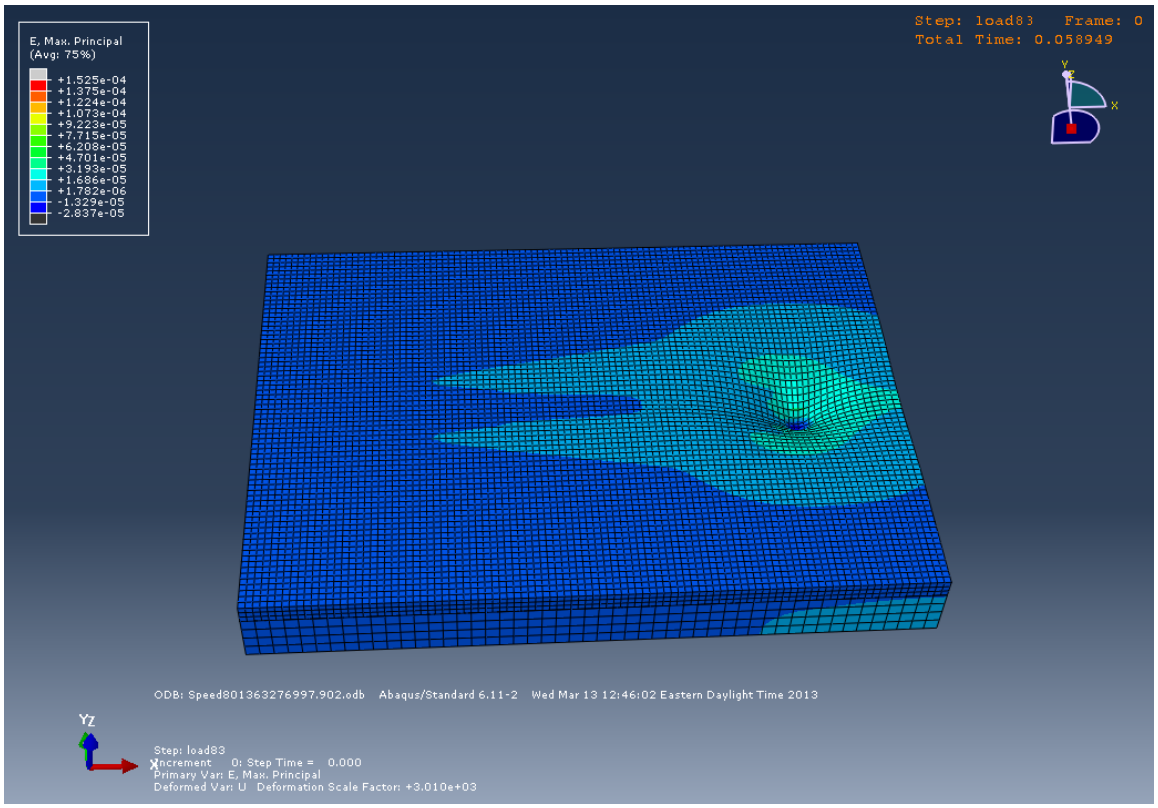

(c) On the right of the section

Figure 42: Pavement strain responses with the position of the wheel.

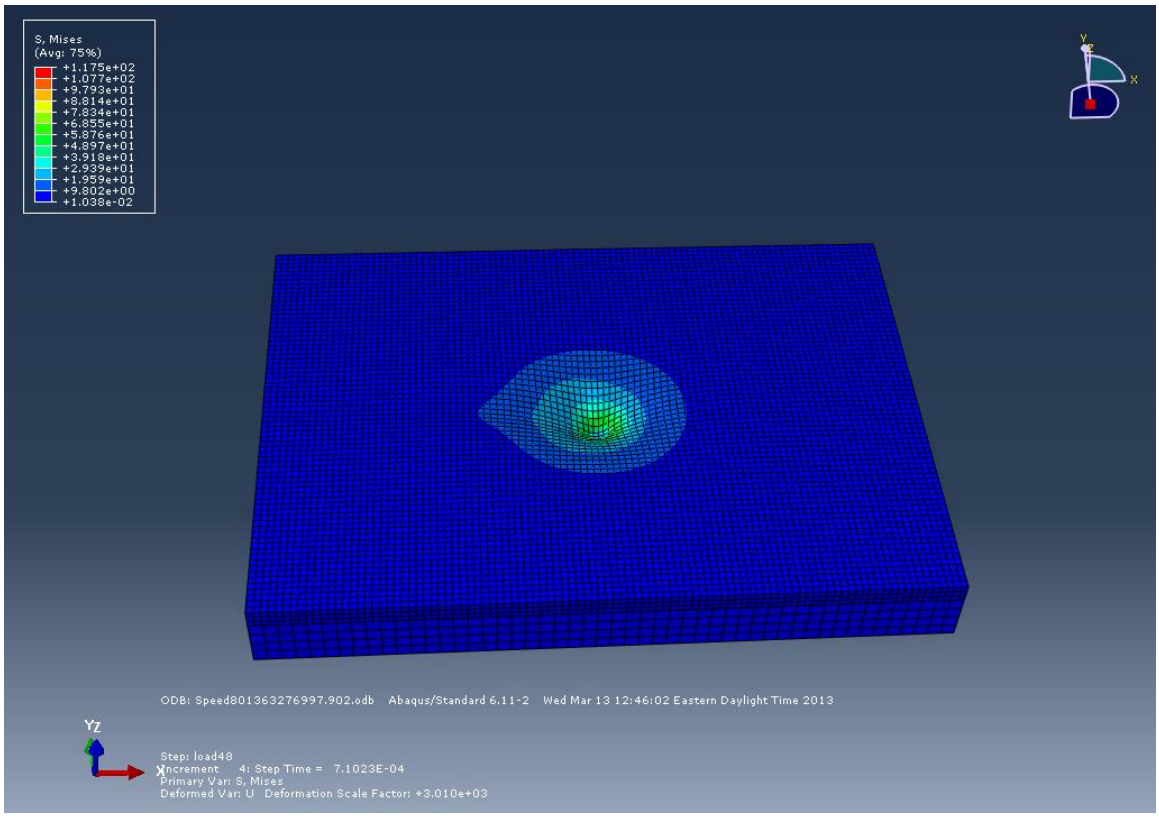

(a) Stress response

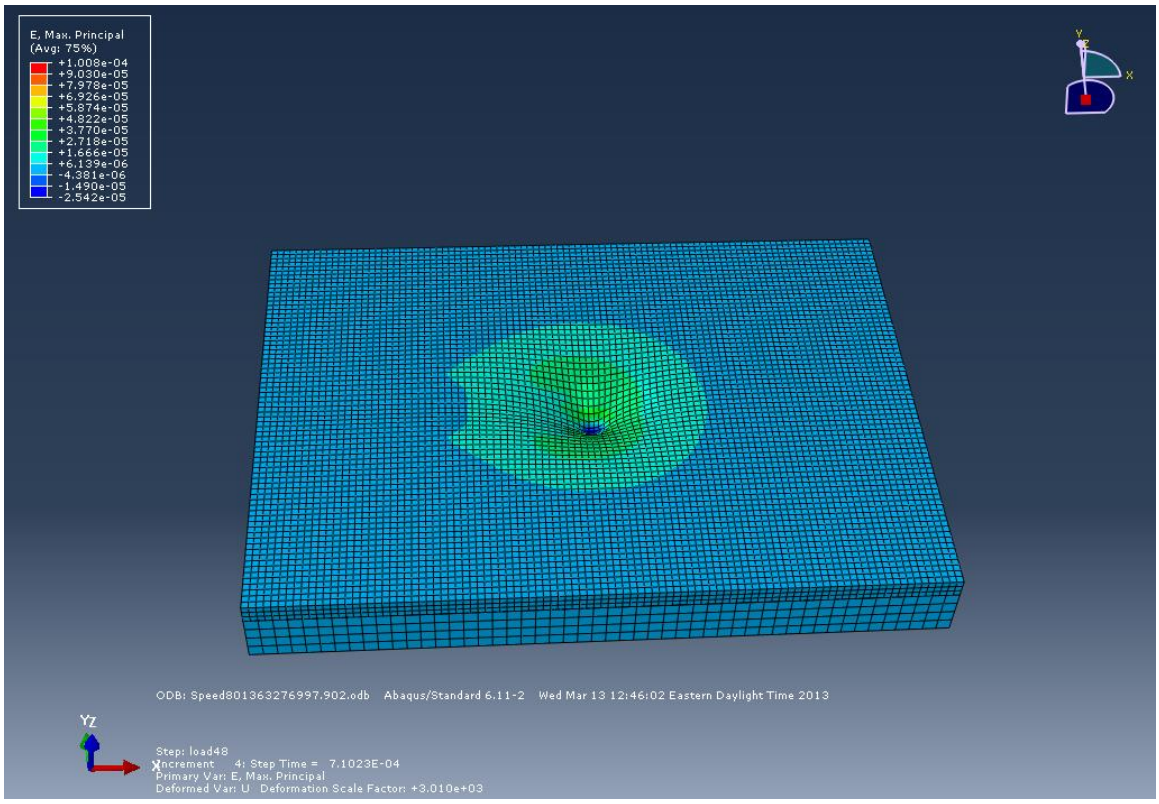

(b) Strain response

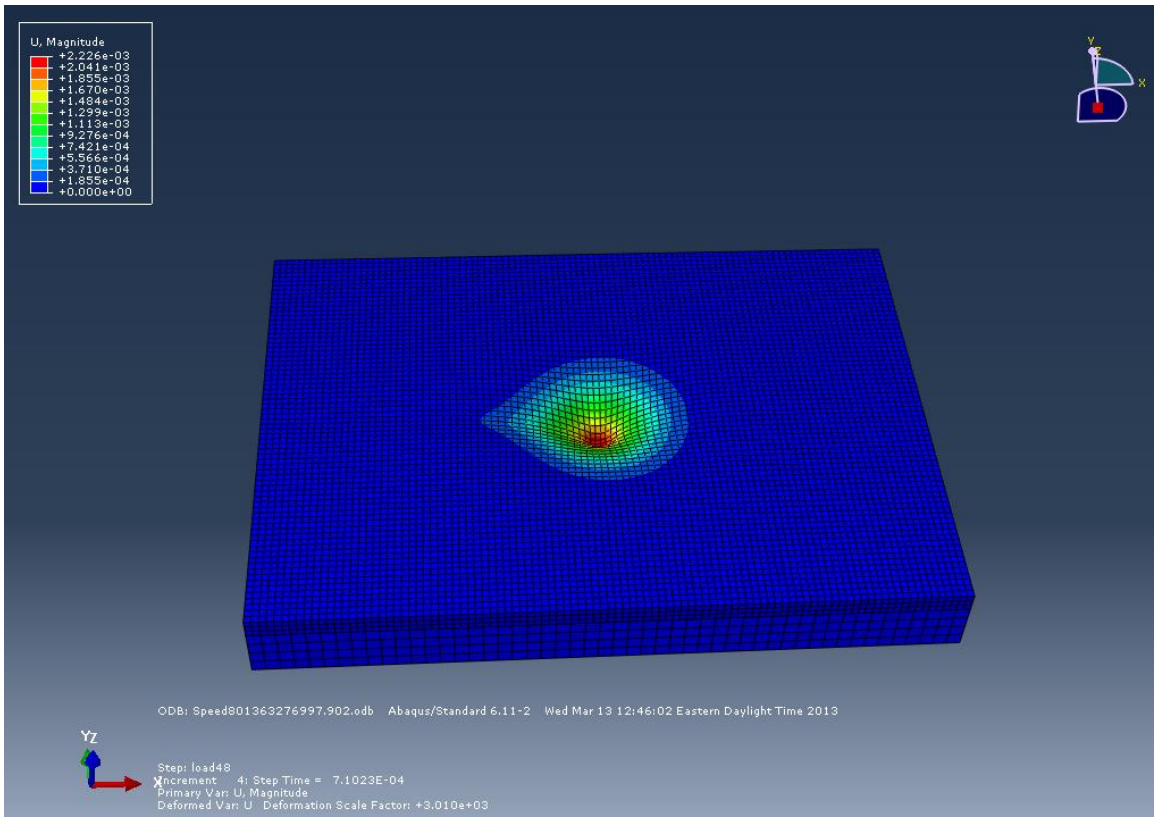

(c) Displacement response

Figure 43: Various pavement responses during the wheel loading process.

As shown in Figure 42 and Figure 43, various pavement mechanical responses changed with the moving wheel. The different responses had their own distribution base on the mechanical compatibility. For simplicity and symmetry, only the responses in the middle transverse plane, corresponding to the step 48, were analyzed.

Data Analysis for Temperature

Since the sensors were installed at the depth of 2 inch, the pavement responses in the transverse plane Y at 2 inch depth were collected for further analysis and comparison with the collected data in this and the following sections. Longitudinal strain ε_X was chosen to present the temperature's effect on the pavement response. The strain

distributions along the transverse plane at 2 inch depth under increasing temperature (°C) are shown in Figure 44, and the maximum strain responses in the middle of the wheel path are summarized in Figure 45.

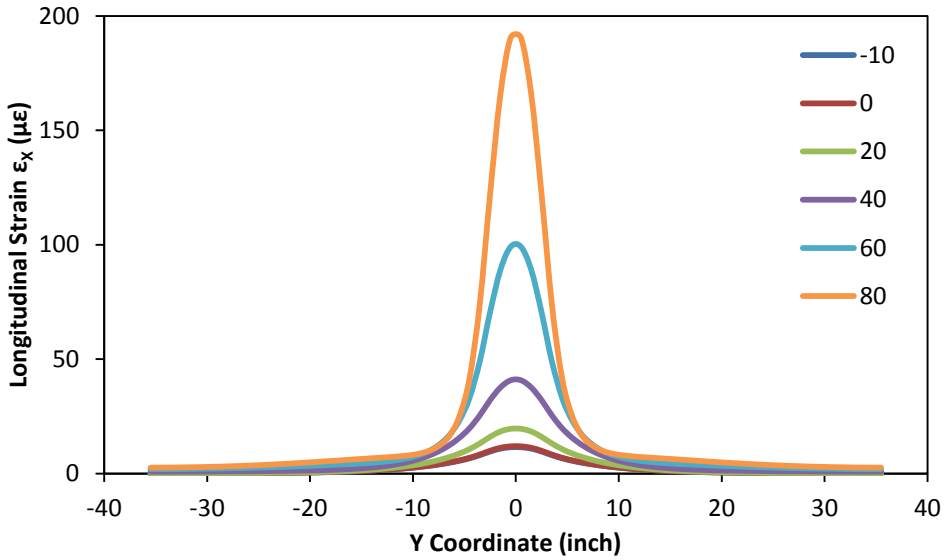

Figure 44: Spatial strain distributions in transverse plane via temperatures.

2 inch depth, 50 mph.

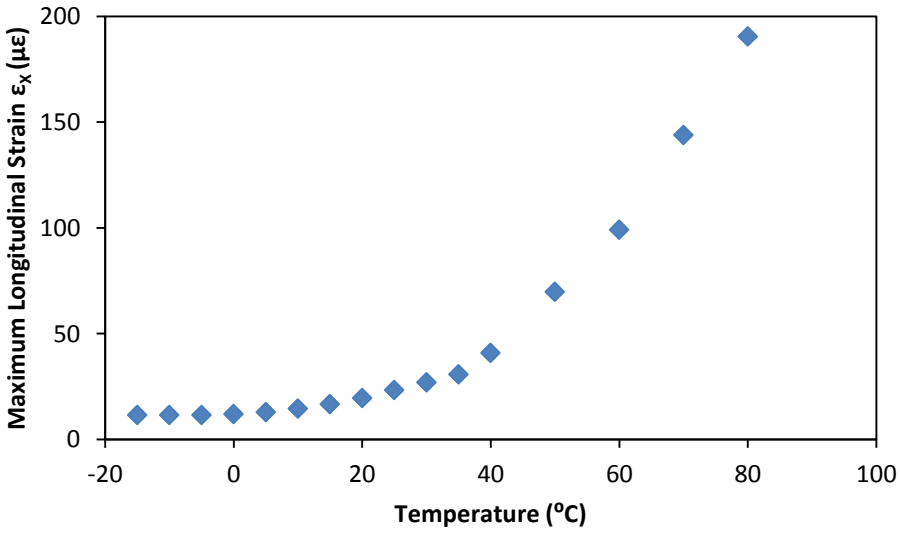

Figure 45: Maximum longitudinal strain via temperature.

2 inch depth, 50 mph.

As shown in Figure 44, pavement responses followed the same distribution pattern under increasing temperatures, but with increasing magnitude. As shown in Figure 45, the strain increased with temperature when the temperature was above 0 ºC, and kept constant when the temperature was below 0 ºC, which was probably because the viscoelasticity of asphalt concrete is negligible when it is cold.

The Gaussian model in the chapter "Traffic Monitoring" was used to simulate the spatial strain distributions in the transverse plane under increasing temperature as in Figure 44, and the simulated parameters are present in Figure 46.

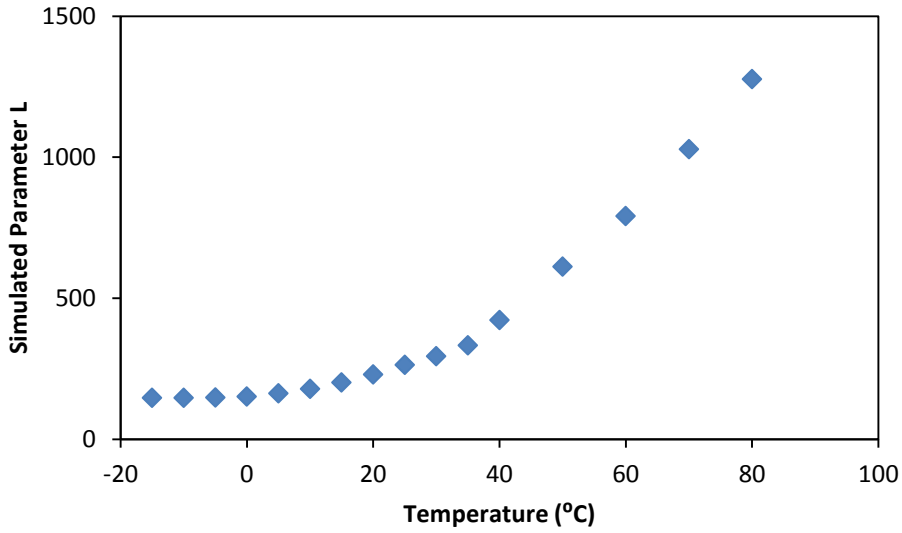

(a) Simulated parameter L

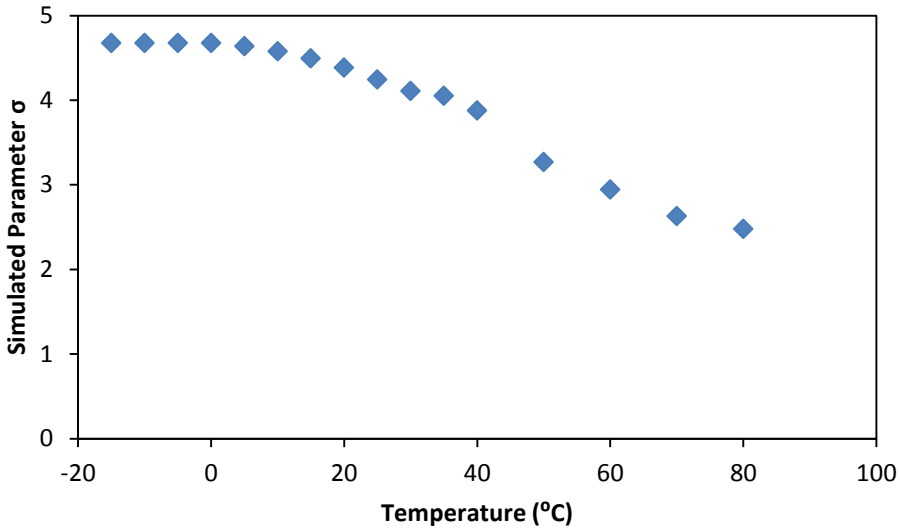

(b) Simulated parameter σ

Figure 46: Simulated Gaussian parameters for calculated strain via temperature
50 mph.

As seen in Figure 46, the simulated parameters of Gaussian model changed with temperature for the same test vehicle, because the pavement strain response from the same loading condition changed with temperature. It is very important to include the temperature's effect in the back-calculation of passed vehicle's configuration and weight.

Data Analysis for Speed

Longitudinal strain ε_X was chosen to present the speed's effect on the pavement response, the same as last section. The strain distributions along the transverse plane at 2 inch depth with increasing speed (mph) are shown in Figure 47, and the maximum strain responses in the middle of the wheel path with increasing speed are summarized in Figure 48.

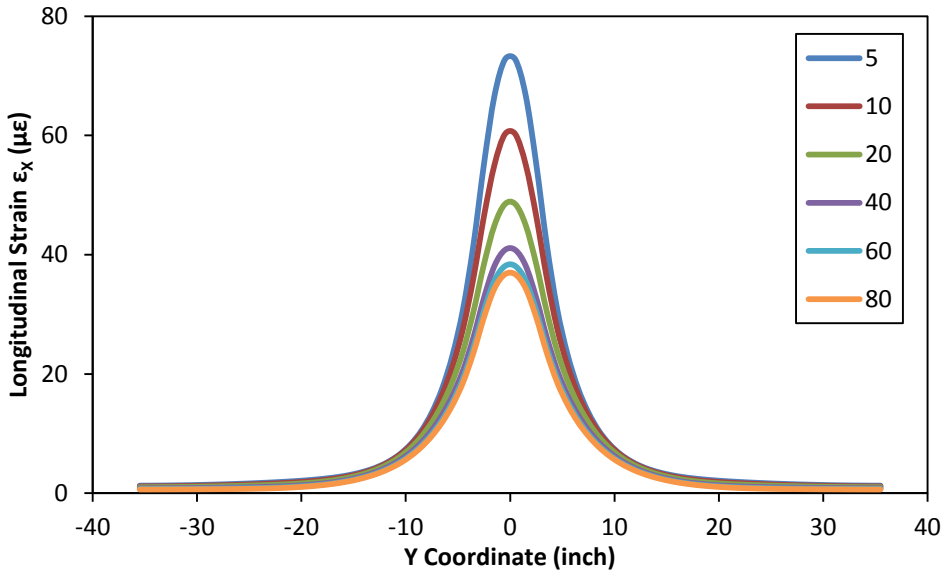

Figure 47 Spatial strain distributions in transverse plane via speed
2 inch depth, 21.1 °C.

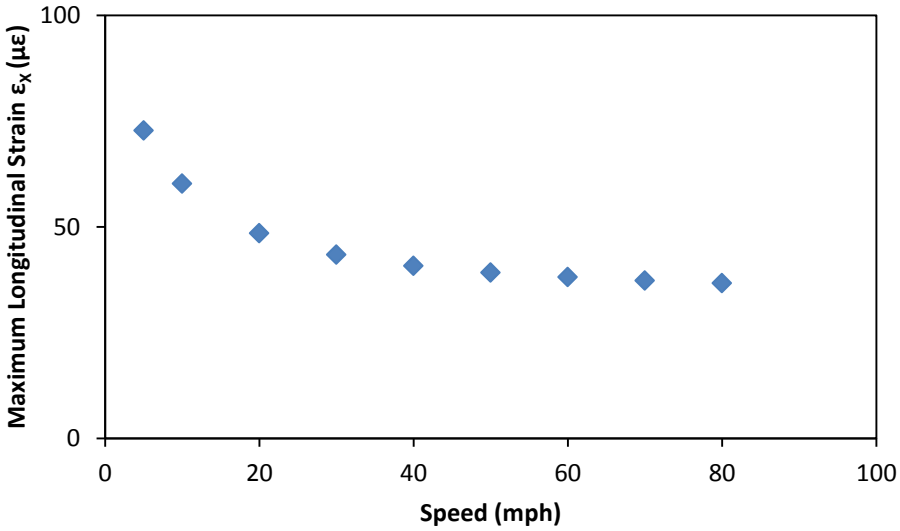

Figure 48: Maximum longitudinal strain via speed
21.1 °C.

As shown in Figure 47, pavement responses follow the same distribution pattern under increasing speeds, but with decreasing magnitude. The changing caused by speed was much lower than that from temperature. Figure 48 present that the strain decreases, and

the changing rate decreased with increasing speed. As a result, the faster the vehicle was, the lower damage it brought to the pavement.

The Gaussian model in the chapter "Traffic Monitoring" was used to simulate the spatial strain distributions in the transverse plane with increasing speed as in Figure 47, and the simulated parameters are present in Figure 49.

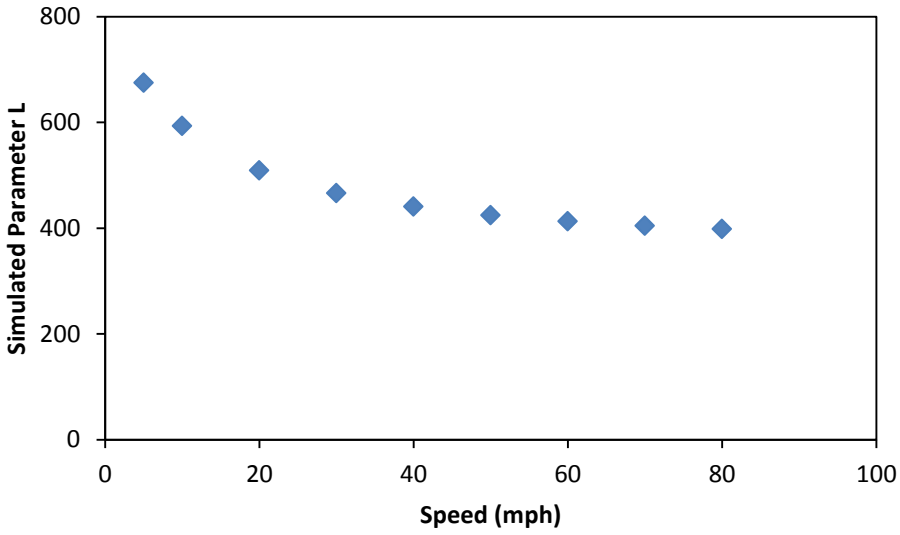

(a) Simulated parameter L

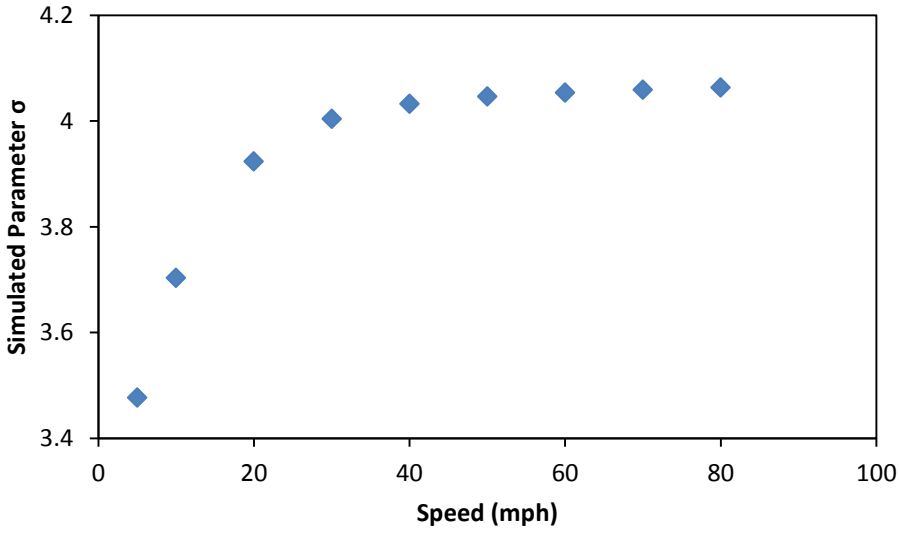

(b) Simulated parameter σ

Figure 49: Simulated Gaussian parameters for calculated strain via speed
21.1 °C.

As seen in Figure 49, the simulated parameters of Gaussian model changed with speed for the same test vehicle, because the pavement strain response from the same loading condition changed with speed. It means that the speed of passed vehicle is important for the back-calculation of passed vehicle's configuration and weight. The speed of vehicle can be back-calculated based on the temporal distribution of collected pavement responses as present in Figure 28, and used for the back-calculation of the weight and configuration in the next step of traffic monitoring.

On-Site Experiment Validation

To find out the effect of temperature and speed, experiments were made several times under different temperatures with speed 40 and 50 mph. For each pair of temperature and speed, the test vehicle was driven through the experiment section at least three times to obtain enough data point to characterize the strain distribution in pavement. As shown in Figure 30, 5 strain gauges were installed in each wheel path, and as a result, 15 strain outputs were obtained for each temperature and speed after 3 test runs. The 5 strain outputs for each test run was analyzed with Gaussian model first to find out the offset distance of the run, and then the total 15 strain outputs with adjusted offset distance were integrated together to form a strain distribution as shown in Figure 50.

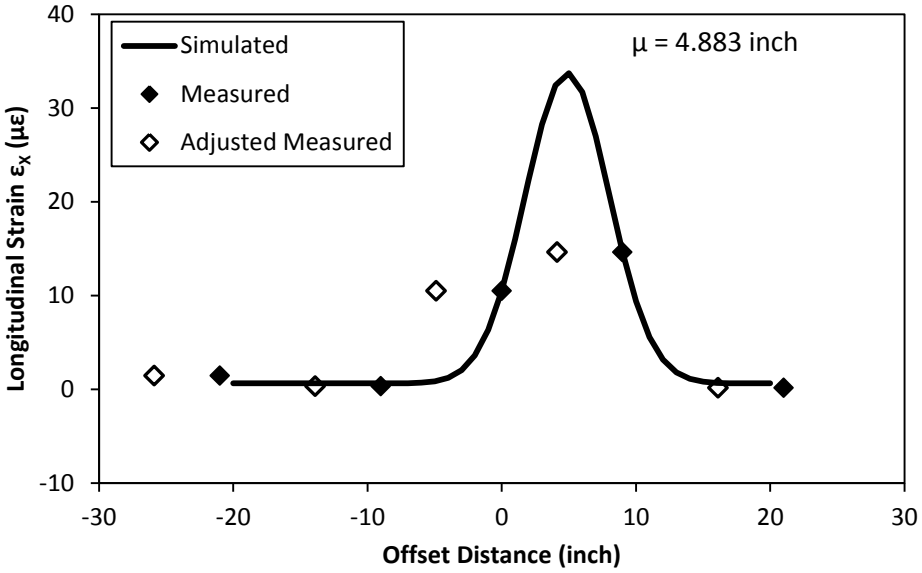

(a) Data point in Run 1 and their adjustments

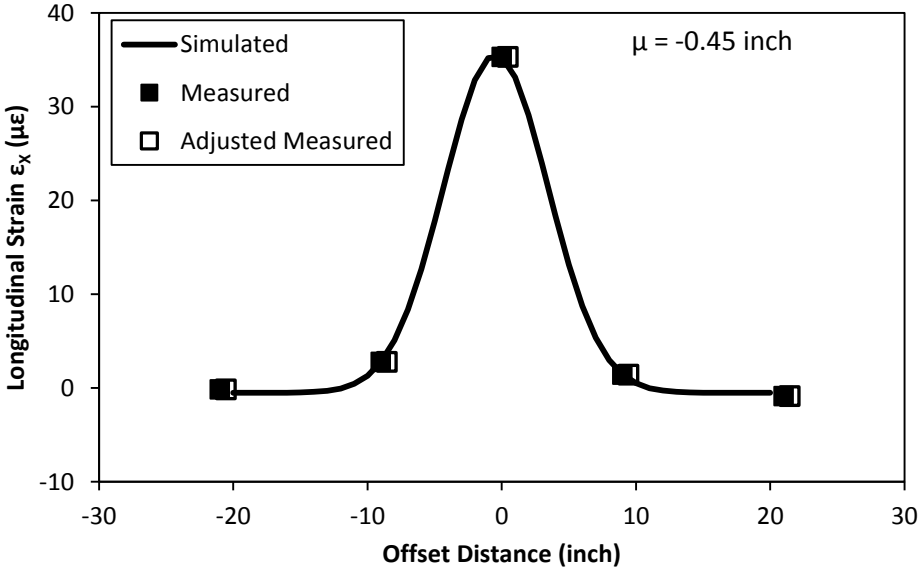

(b) Data point in Run 2 and their adjustments

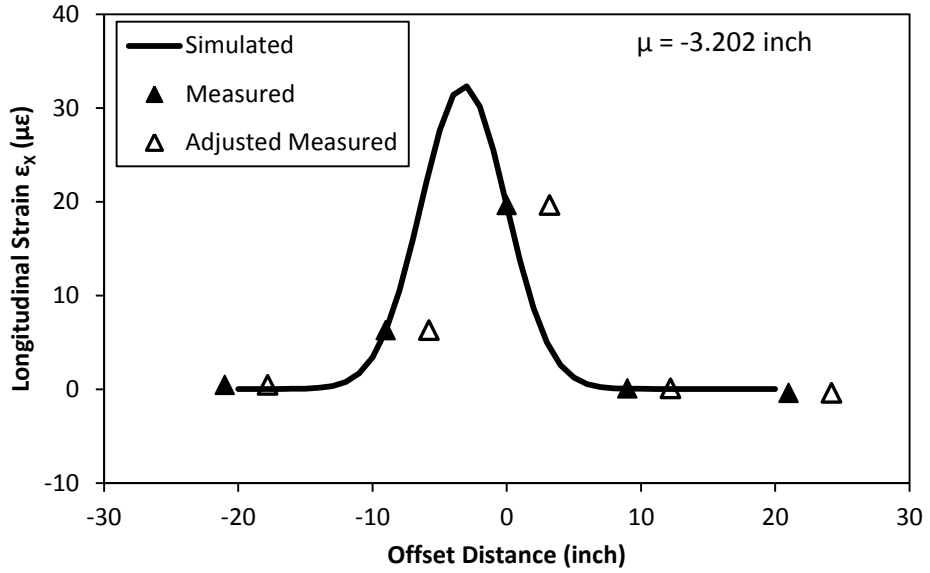

(c) Data points in Run 3 and their adjustments

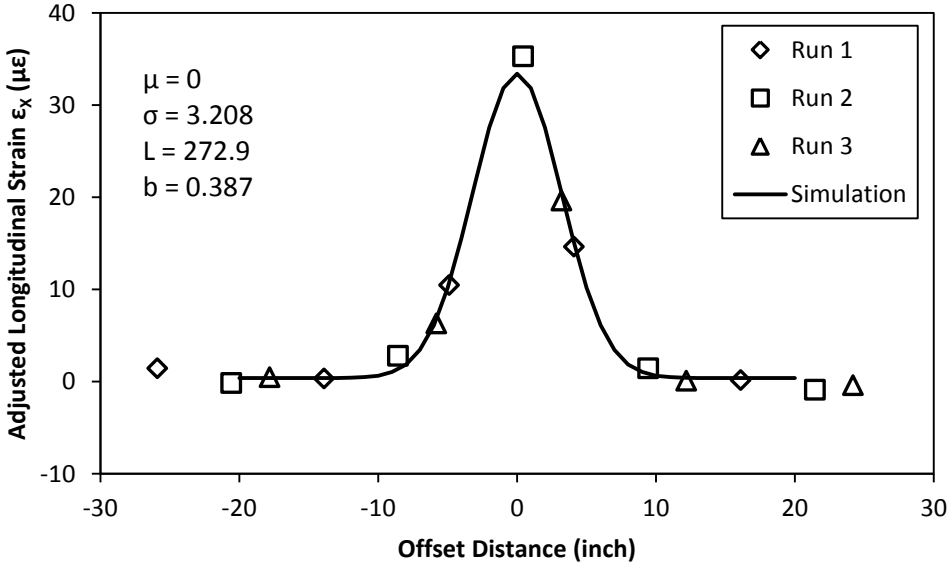

(d) Integrated strain distribution of Run 1, 2 and 3

Figure 50: Integration of data points collected under the same temperature and speed

Sep. 9, Series 3, Run 1, 2, 3, -0.99 ºC, 50 mph.

As explained in Figure 50, after the adjustments based on the first Gaussian simulation, the data points from testing runs with the same temperature and speed can be integrated into a strain distribution curve with enough points to characterize its configuration. The

integrated distribution curve was analyzed with Gaussian model again, and the simulated parameters σ and L would be more stable and accurate because they were based on 15 measurements instead of 5.

For each passing vehicle, the front and rear tires were both integrated in the same way for each pair of temperature and speed, and compared in Figure 51.

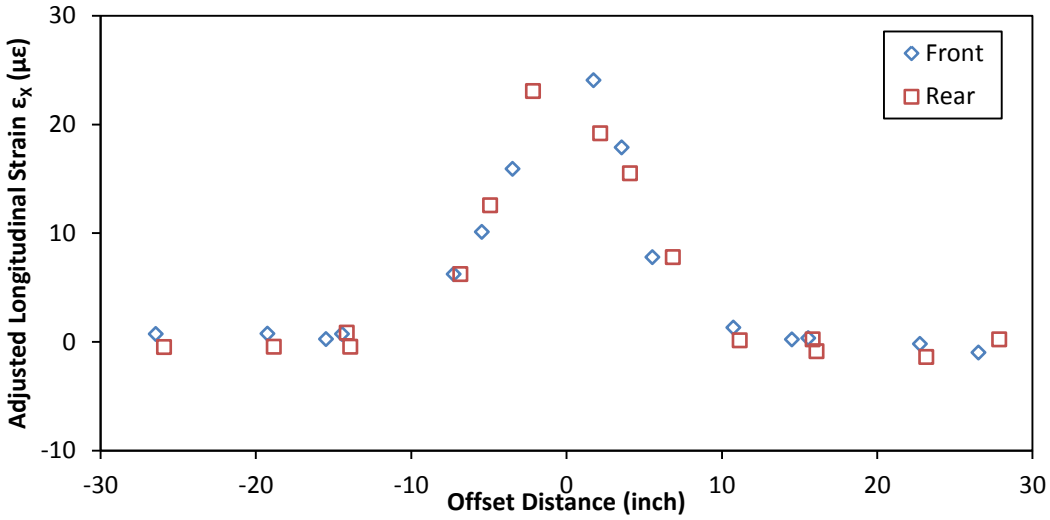

Figure 51: Integrated strain distribution for front and rear tires

Sep 9, Series 2, Run 4,5,6, 1.05 °C, 40 mph.

In Figure 51, the strain distribution induced by the front tire and the rear tire were close to each other. In fact, they were quite different in magnitude when the vehicle ran in bumping and different in position when the vehicle didn't run in straight. In the most testing cases, the testing vehicle was driven in straight and smooth, and the distribution from the front and rear tire were close and treated together to represent the strain distribution induced by the testing vehicle under the corresponding temperature and speed.

For each temperature, the testing vehicle was driven across the section with two different speeds, 40 and 50 mph. the resulted integrated strain distributions were shown in Figure 52. The integrated strain distributions caused by the same testing vehicle under different temperature are shown in Figure 53.

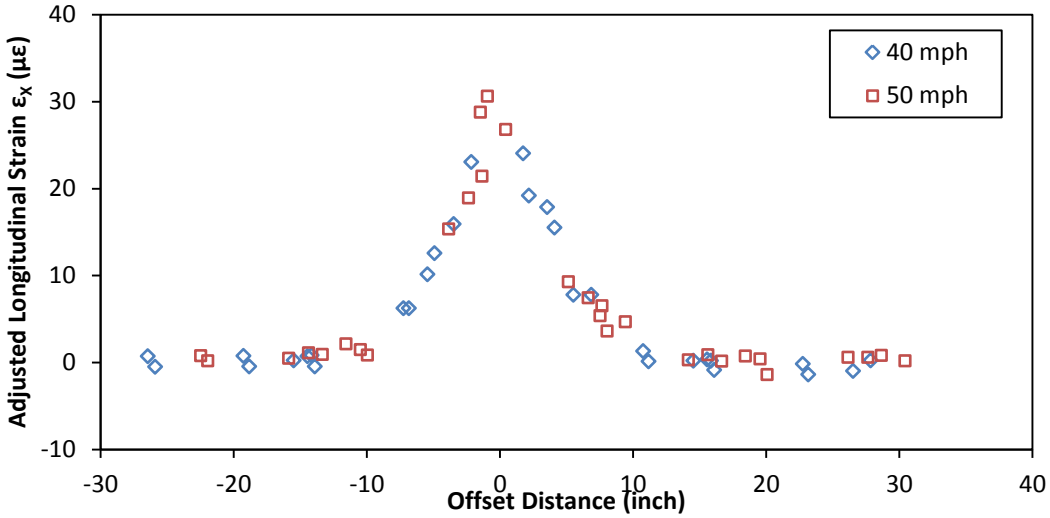

Figure 52: Integrated strain distributions in experiments with different speeds

Sep 9, Series 2, Run 1,2, 3, 4,5,6, 1.05 °C

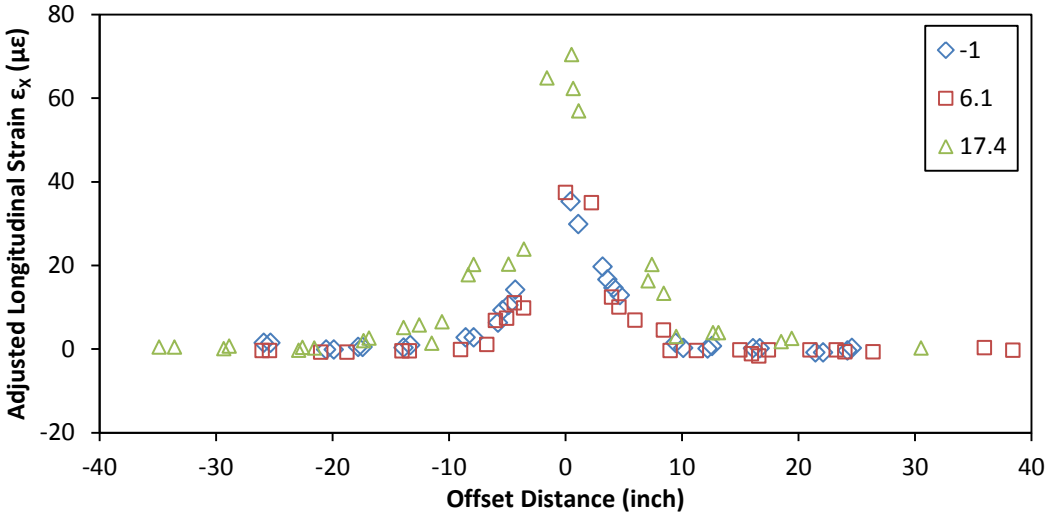

Figure 53: Integrated strain distributions in experiments under different temperatures.

Sep 9, Series 3,1, Aug 8, Series 4.50 mph.

As shown in Figure 52, the resulted strain responses for the two cases were very close, probably because of the little difference between the speed conditions. Figure 53 showed that the strain distributed with similar trend but increasing magnitude when the temperature was increasing.

The distributions caused by vehicle with different speed can be analyzed with Gaussian model, and the simulated parameters $\sum L$ from collected strain responses were summarized in Figure 54. Due to the humid weather and harsh environment, some strain gages on the right wheel path (B part in Figure 13) didn't work anymore after the experiment on June 6th, and all the data analysis in this section was based on the signals collected from the left wheel path (A part in Figure 13).

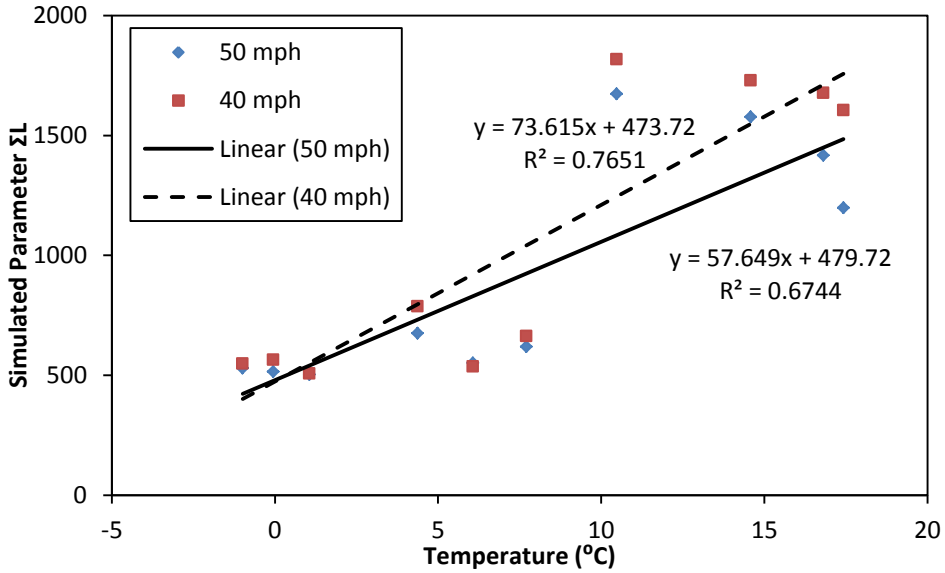

(a) Simulated Parameter ΣL

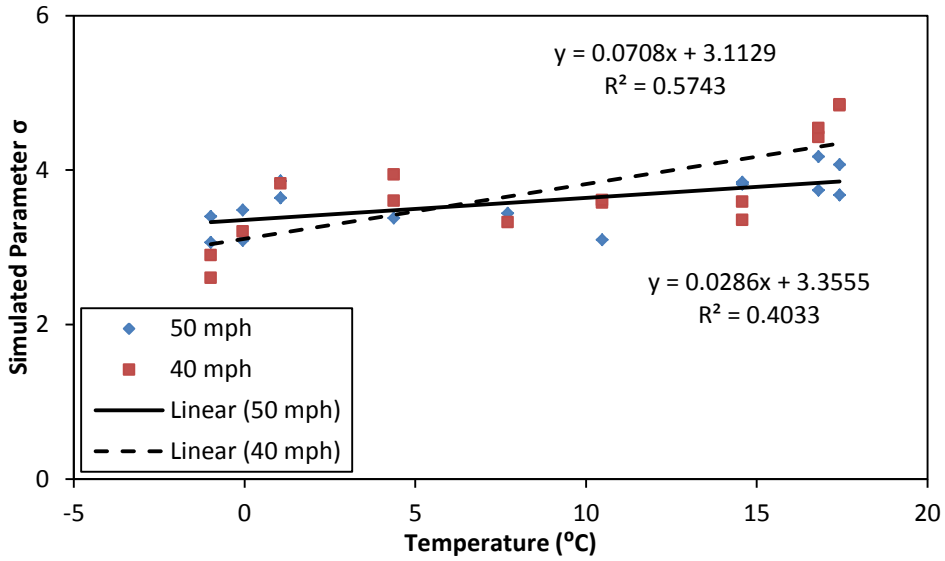

(b) Simulated Parameter σ

Figure 54: Simulated Parameters with Different Temperatures and Speeds

As shown in Figure 54, the simulated parameter of Gaussian model $\sum L$ changed with temperature obviously, and $\sum L$ caused by the test run of 40 mph was more than that from the test run of 50 mph because of the viscoelasticity of asphalt concrete. At the same time, the correlation between the simulated parameter σ and the temperature was much lower, which meant that the strain distribution pattern shaper changed little with changing temperature.

During the vehicle moving process, the load distribution on the tires was changing all the time, and the difference was quite obvious. In this section, due to the damage of some strain gauges in the right wheel path, the simulated parameter ΣL was only the sum of the two left wheel instead of all the wheels as in the previous section. Due to the damage of the sensors in the right wheel path, the load difference between the left and right wheels

were ignored, and the simulated parameter ΣL for the left wheel path was used to represent the weight of the passing vehicle, which induced big deviation in Figure 54.

Discussion and Conclusion

Asphalt concrete is usually treated as a linear viscoelastic material because its mechanical properties depend on the temperature and loading rate. Viscoelastic material is common and complicated, and its mechanical model usually consists of elastic springs and viscous dashpots, and the viscoelastic model used in the analysis is the generalized Maxwell model. Important viscoelastic properties include dynamic modulus, relaxation modulus and creep modulus, and most common laboratory tests include creep, relaxation and repeated pulse tests. The laboratory tests are usually done under more than 3 different temperatures and the results can be integrated together into the master curve in frequency domain with a reference temperature based on time-temperature superposition.

A numerical model was built up in ABAQUS to simulate the process that a wheel rolled across the experimental section. There were 94 step of the whole process, and a contact area was defined for each step with constant pressure. The simulation was made with various temperature and speed, and the results were analyzed for the impact of temperature and speed on the strain response in pavement.

In the experiments, the testing vehicle was driven across the section at least 3 times for each combination of temperature and speed. The strain response data points from the 3 testing runs could be integrated together based on their back-calculated offset distance.

The integrated strain distribution has 15 data points instead of 5 points in each single testing run, and the distribution can be characterized much more accurately.

Even though the numerical simulation can't present the difference between the front and the rear tire, there are slight differences between them in the collected longitudinal strain response in some cases because of the dynamic effect.

In general, no matter in numerical simulation or experiment outputs, strain response in pavement distributed in the same trend, but with the increasing magnitude when the temperature increased. At the same time, the strain response decreased with increasing speed. However, the effect of temperature was much more obvious than that of speed.

Gaussian model can be used to analyze the distribution of longitudinal strain. The simulated parameter $\sum L$ increased with temperature in both numerical simulation and experiment output in a linear manner. However, the back-calculated result were not accurate enough because many installed sensors stopped working before the experiment due to bad environment and excessive traffic load. The simulated parameter σ decreased with increasing temperature and decreasing speed in numerical simulation, but such trends could not be found in the actually collected responses.

In general, the effect of temperature and speed on pavement mechanical responses are important and can't be ignored. It is important for pavement health status estimation and traffic back-calculation to understand and make use of their effect for better estimation of the status of the pavement and the traffic flow. However, incorporating the dependence

on temperature and speed in the whole monitoring system will be a challenge on the back calculation and database capacity.

EFFECT OF TIRE CONFIGURATION AND INFLATION PRESSURE

The main target of Ohio SPS-8 experiment was to compare the potential damage brought to the pavement by different kinds of tires and different tire inflation pressure. To fulfill the target, the experiment was designed to include four tire configurations (Table 3), three tire inflation pressures and three target speeds (Table 4). To understand the effect of tire configuration and inflation pressure, strain distributions and predicted distresses were compared between different tire configurations and inflation pressures with the same temperature, speed and offset distance.

Variable Measurements

In field experiments, lots of uncontrollable environmental and loading factors existed, such as pavement temperature, speed of the test vehicle, offset distance of each run, and so on. These variables might cause variation in field measurement, and made the data analysis difficult. These factors may be accounted for by using laboratory test and pavement analysis software correction, as described in this chapter.

Temperature in Pavement

Temperature in pavement is different from air temperature, and should be measured separately in experiments. For the experiment in Ohio, pavement temperature was measured from morning to evening at the depth of 1 inch, 3 inch and 7 inch on the three days of the experiment. For the experiment in Virginia, pavement temperature was

obtained from the thermo couple, which was installed at the same depth as strain gages and load cells. One example of temperature distribution collected in Ohio experiments is shown in Figure 55[6].

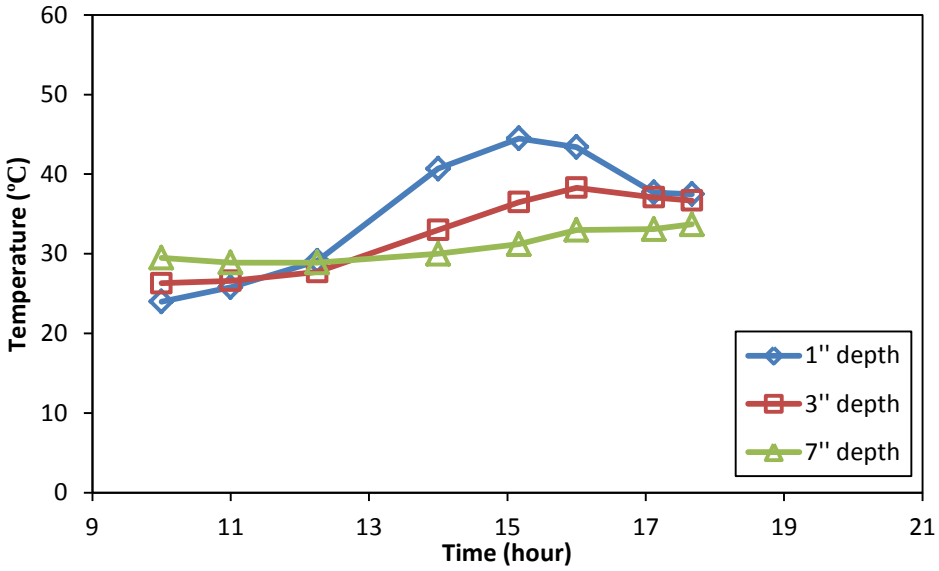

Figure 55: Measured Pavement Temperature Distribution on June 22

To verify the current pavement temperature model, the measured temperature distribution was compared with prediction of Velasquez Pavement Temperature Model, expressed briefly in Eq.(58-59).

$$T_{MAX\_PAV} = 11.432 + 7.123 \times 10^{-3} T_{MAX\_AIR}^2 + 0.743 T_{MAX\_AIR} - 61.742D + 4.604 \times 10^{-4} S - 0.108H - 1.313W \quad \text{Eq.(58)}$$

$$T_{MIN\_PAV} = 2.136 + 5.353 \times 10^{-3} T_{MAX\_AIR}^2 + 0.902 T_{MAX\_AIR} + 32.926D + 1.687 \times 10^{-4} S - 0.025H - 0.491W \quad \text{Eq.(59)}$$

where T_{MAX_PAV} and T_{MIN_PAV} represent the maximum and minimum temperature in the pavement (^{0}C); T_{MAX_AIR} and T_{MIN_AIR} are the maximum and minimum temperatures in the air (^{0}C); D is the depth of the location (m); S is the calculated solar radiation (kJ/m^2 · day); H is the humidity (%) and W is the wind speed (m/s).

All the parameters used in this model were provided by LTPP database. The calculated temperature traces are present in Figure 56 compared with measured temperature on Jun 22nd.

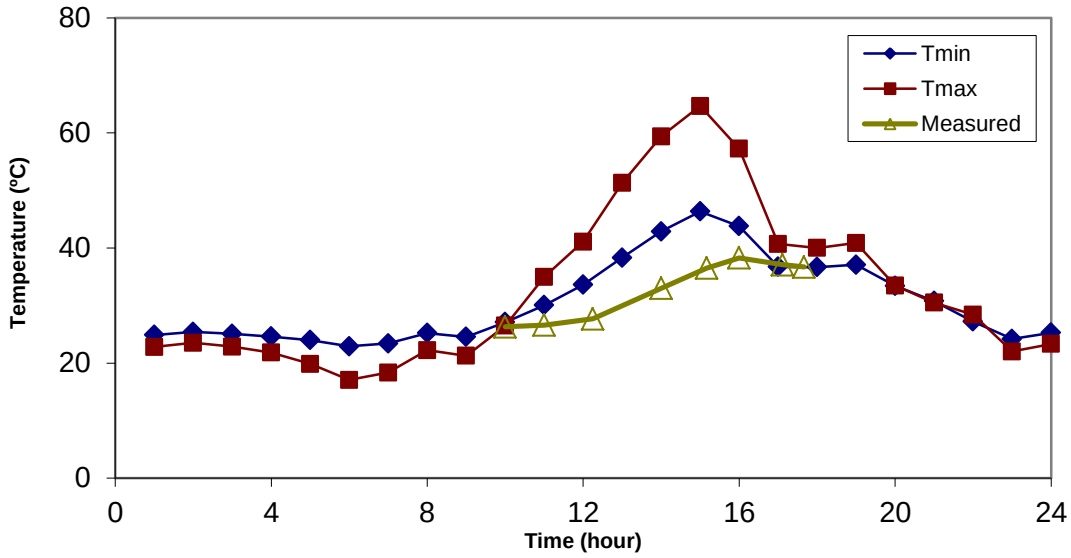

Figure 56: Predicted and Measured Temperature in Ohio Experiment

June 22nd, 3.5 inch depth

From the comparison, the predicted minimum pavement temperature was closer to the actual measurements. The comparison revealed the limits of the current pavement temperature model, and promoted measuring temperature in experiments instead of numerical modeling. Known the temperature history, for each run in experiment, the temperature can be obtained by interpolation between two adjacent time points.

Speed of Vehicle

In the field experiments, the speed of test vehicle was controlled by the driver manually. However, it was difficult for the driver to keep the speed constant, and the actual speed might be close to the target speed with some deviations.

In the Ohio experiment, since the model of the vehicle was fixed, the speed was calculated by counting time interval between front and rear axles, and converted to speed according to the distance between front and rear axles, as explained in Eq.(60).

$$S = \frac{D}{T_R - T_F} \qquad \text{Eq.(60)}$$

where S is the actual speed of the run; D is the distance between the front axle and rear axle 21.25 ft; T_R and T_F represent the time of corresponding peak from rear and front tire.

The calculated speed presented a power relationship with measured loading time (time interval between adjacent peaks in a fluctuation) as shown in Figure 57 [6].

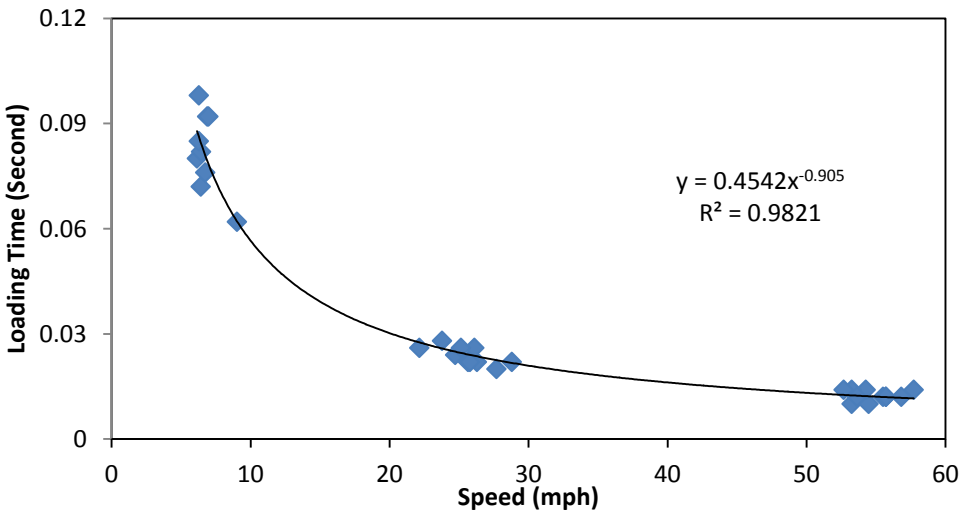

Figure 57: Relationship between Speed and Loading Time

Ohio experiment, Top of 4'' AC, GoodYear Wide-base, Shear Strain S_1_2_3

Offset Distance

In Ohio experiment, the offset distance data was collected using the Sand Track Method. The area around the holes was covered by sand, and the test truck was driven by the hole, with the track of the tire left on the sand. The offset distance here was set as the distance between the edge of the tire track and the centerline of the holes, as shown in Figure 58.

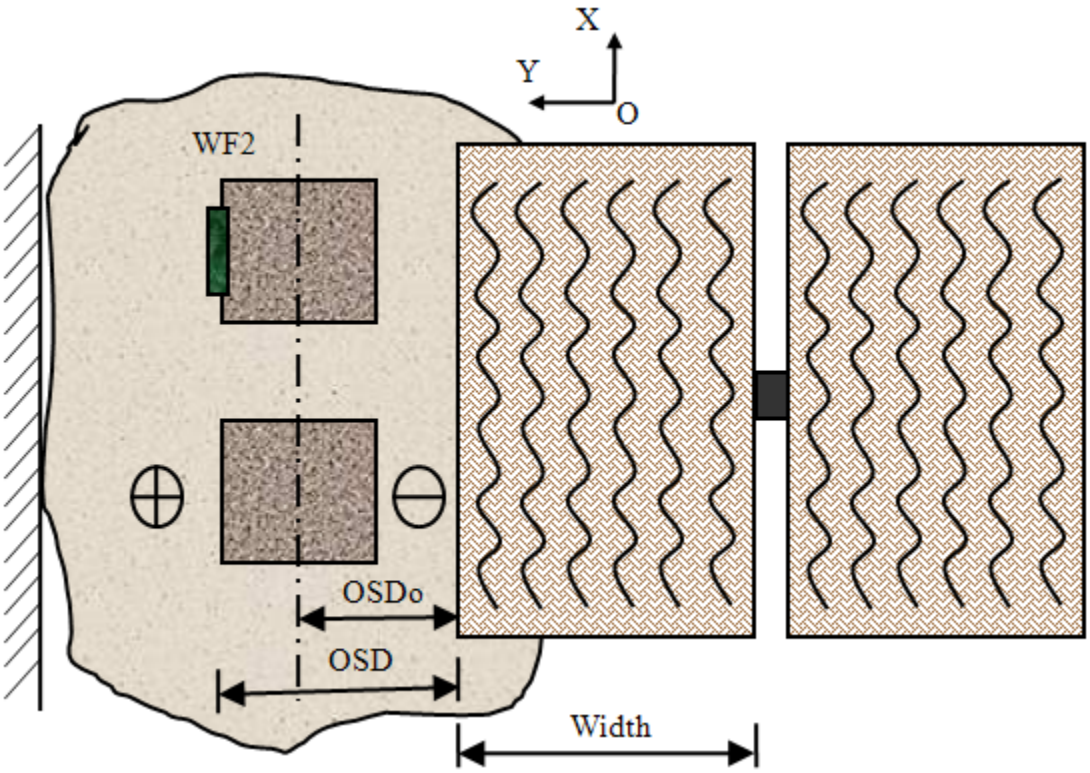

Figure 58: Offset Distance Collection in Sand Track Method

In the sand track method, OSD_O was the recorded offset distance between centerline of the holes and outer edge of the tire. OSD_O was positive when the edge of tire was on the left side of the centerline, and negative when the edge of the tire was on the right side of the centerline. The adjusted offset distance *OSD* meant the distance from the sensor to the

outer edge of the tire, which can be calculated according to the position of the sensor to the centerline of the holes.

Adjustment for Temperature and Speed

Viscoelastic Property of Asphalt Concrete

In the experiment of Ohio, all of the three tests were conducted on AC samples taken from the test sections. An example of a relaxation test result is presented in Figure 59 to show the imposed stepped strain increments and measured stress relaxing over time.

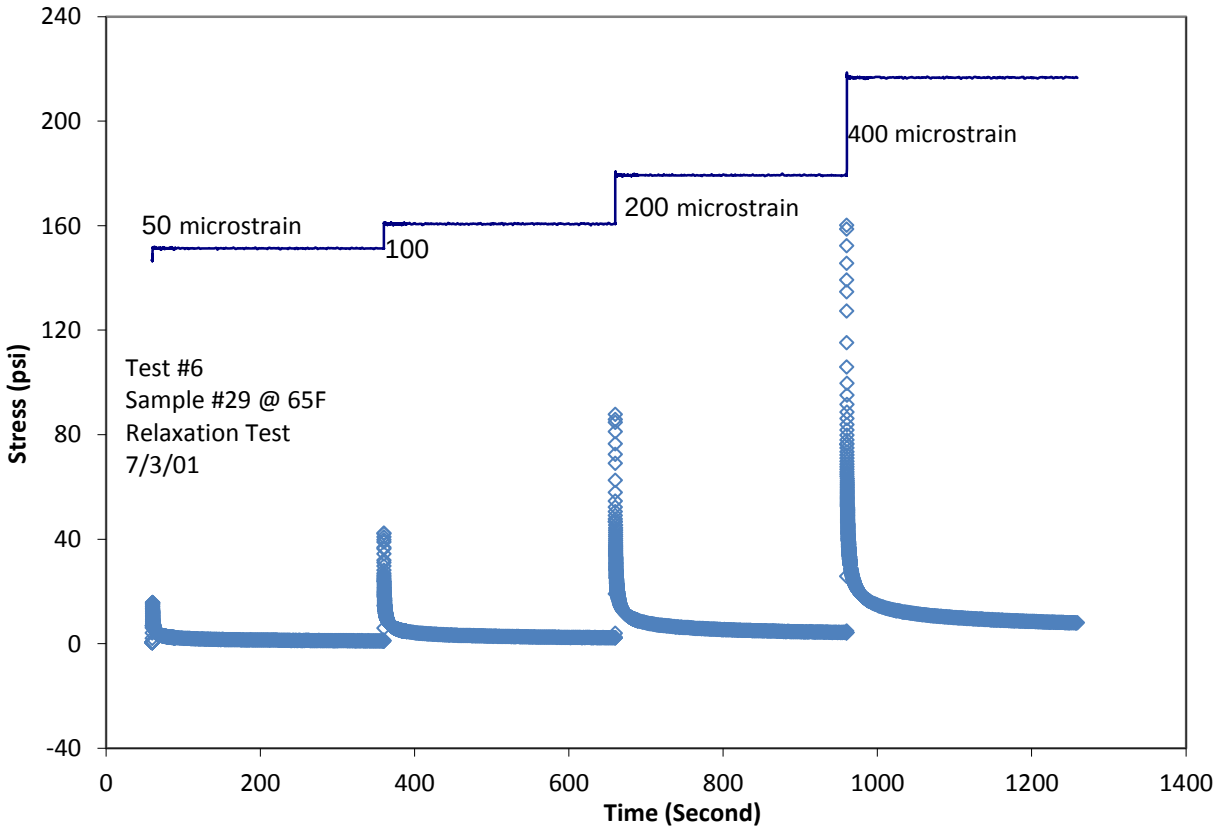

Figure 59: The result of relaxation test under 65 ^{o}F

All the relaxation tests at different temperatures can be presented with a common Prony Series and corresponding Temperature Shift Factors together. In the Ohio experiment, the calculated Prony Series and Temperature Shift Factors were tabulated in Table 13. The comparisons between predicted modulus and the measured modulus are shown in Figure 60.

Table 13: Viscoelasticity of the asphalt concrete in Ohio experiment

Prony Series		
	E_i	ρ_i
0	2191.10565	
1	4.51739014	1.42E+07
2	87.1152282	8.13E+05
3	26.0830443	4.67E+04
4	8.91186237	2.68E+03
5	8445.05685	1.54E+02
6	17013.0612	8.81E+00
7	62500.2705	5.06E-01
8	169580.39	2.90E-02
9	9.01873594	1.66E-03
10	6.40654908	9.55E-05
11	37.6449779	5.48E-06
12	35.0681389	3.14E-07
Temperature Shift Factor $\alpha(T)$		
Temperature	Log ($\alpha(T)$)	
65 ˚F	1.356458825	
90 ˚F	0	
115 ˚F	-1.235252897	

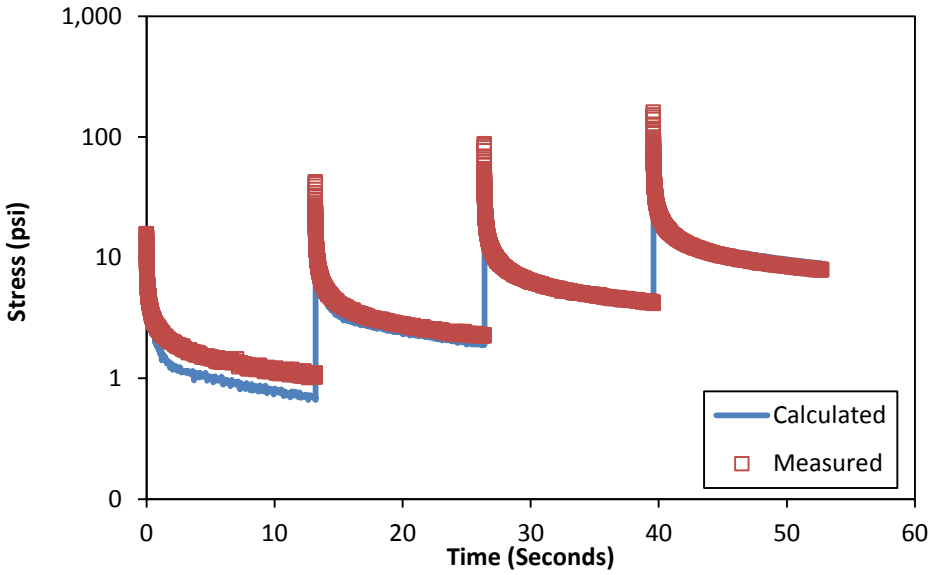
1,000
100
10
1
0
Stress (psi)
0
10
20
30
40
50
60
Time (Seconds)
Calculated
Measured

(a) 65 ˚F

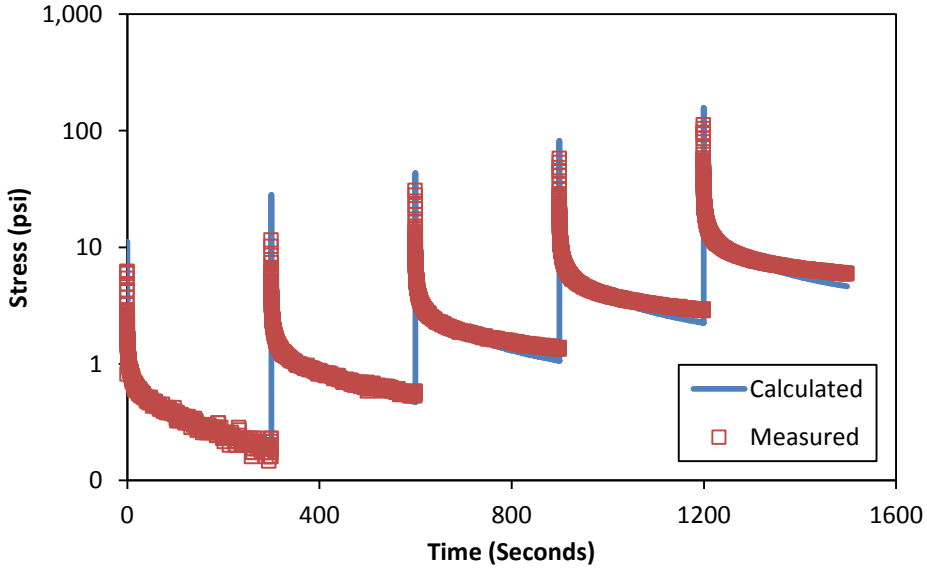
1,000
100
10
1
0
Stress (psi)
0
400
800
1200
1600
Time (Seconds)
Calculated
Measured

(b) 90˚F

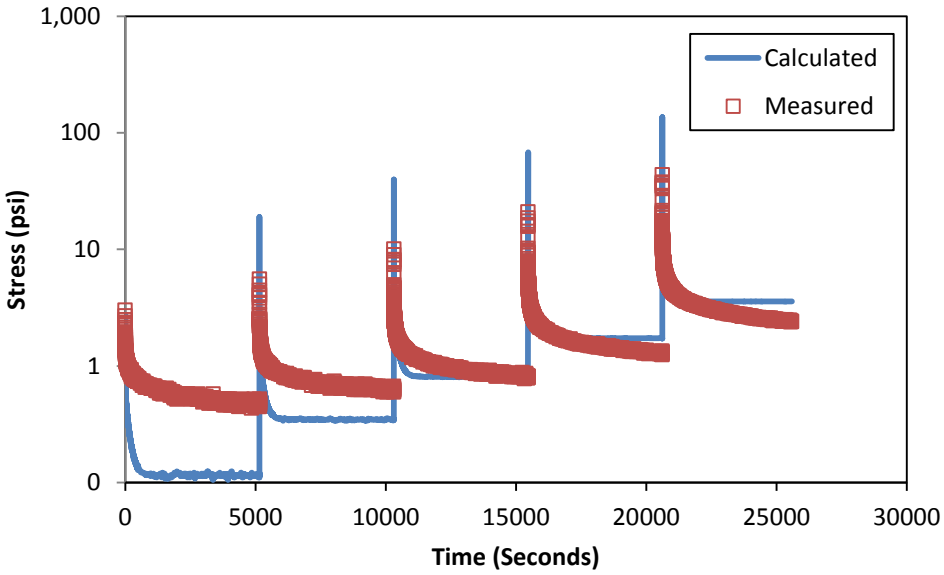

(c) 115 ˚F

Figure 60: The Simulation of the Relaxation Test in Ohio Experiment

After a comparison of the three simulations under different temperatures, a good match can be concluded in most part of the tests, except for the first two loading periods under 115 ˚F. It was very difficult for a Prony Series to match three relaxation tests under different temperatures, and the accumulated square error was still in a reasonable range. The Prony Series in Table 13 was the best result obtained up to now, and a better result can be expected with a more suitable Prony series in the future.

With Prony Series known, the generalized Maxwell model can be fit to the storage modulus E' (the real part of complex modulus) and loss modulus E'' (the imaginary part of complex modulus) in the frequency domain. Dynamic modulus $|E^*|$, defined as the ratio of the dynamic stress amplitude to the dynamic strain amplitude, can be calculated with the storage modulus E' and the loss modulus E''.

$$E'(\omega) = E_0 + \sum_{i=1}^{m} \frac{\omega^2 \rho_i^2 E_i}{1+\omega^2 \rho_i^2} \quad \text{Eq.(61)}$$

$$E''(\omega) = \sum_{i=1}^{m} \frac{\omega \rho_i E_i}{1+\omega^2 \rho_i^2} \quad \text{Eq.(62)}$$

$$\left|E^*\right| = \frac{\sigma_0}{\varepsilon_0} = \left|\sqrt{(E')^2 + (E'')^2}\right| \quad \text{Eq.(63)}$$

where E_i is the elastic spring stiffness and ρ_i is the relaxation time for each element in the generalized Maxwell Model, both of which can be found in Prony Series present in Table 13. The dynamic modulus can be calculated in frequency domain, which is called dynamic modulus master curve.

In the mechanistic-empirical pavement design guide, the sigmoidal function in following equation is used to describe the rate dependency of the modulus master curve, and serve as a direct expression of master curve.

$$\log\left(\left|E^*\right|\right) = \delta + \frac{\alpha}{1+e^{\beta+\gamma(\log \omega_r)}} \quad \text{Eq.(64)}$$

Where $\left|E^*\right|$ is the dynamic modulus; ω_r is the reduced frequency; δ represents the minimum value of $\left|E^*\right|$; $\delta+\alpha$ is the maximum value of E*; β, γ are parameters describing the shape of the sigmoidal function. The useful part of the Sigmoidal function matches the master curve the best by setting the error of this part the minimum, present in Figure 61. The calculated Sigmoidal function is:

$$\log\left(\left|E^*\right|\right) = 2.878546 + \frac{2.688040}{1+e^{-0.867070-0.669119(\log\omega_r)}} \qquad \text{Eq.(65)}$$

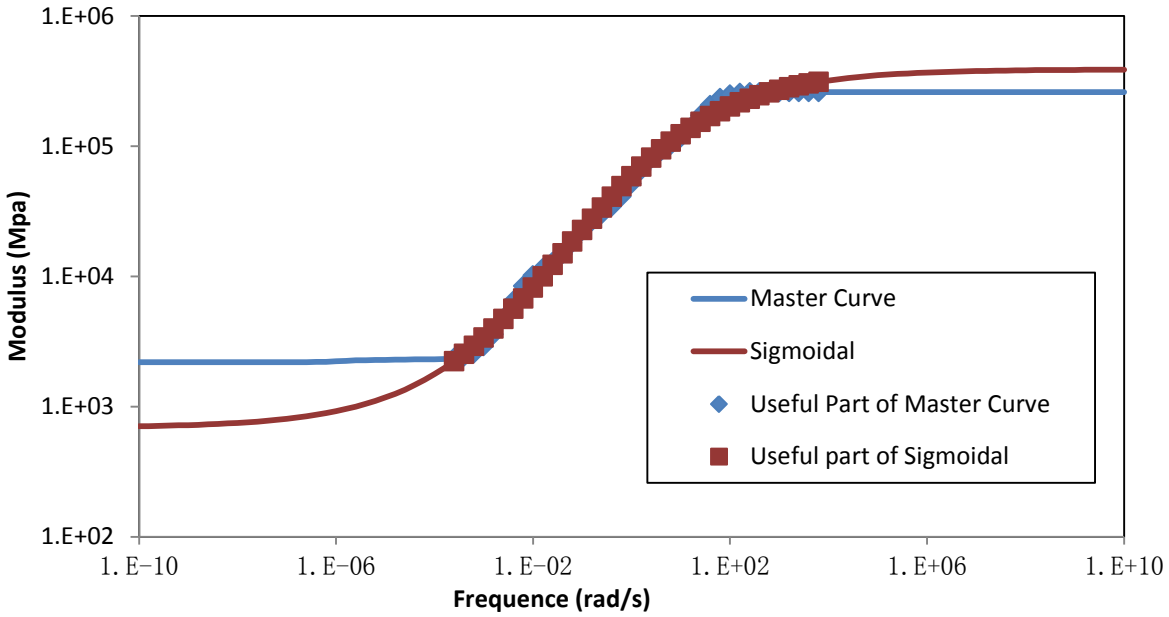

Figure 61: Sigmoidal function and Dynamic Modulus Master Curve

Relationship between Modulus and Strain Distribution

In the experiment in Ohio, the test runs were prosecuted at different time of the three days manually, under different temperatures. To make reasonable comparison and analysis, all the PEAK TO PEAK value should be corrected from its actual temperature to a universal one, which was set as 90 ºF in the project. At the same time, since the vehicle was driven manually, the speed could not always be the target speed accurately, so the PEAK TO PEAK strain should be corrected to the target speed, corresponding to the target frequency, before the final comparison.

To take temperature and speed into consideration, actual modulus and target modulus were calculated from reduced loading time with Prony Series. For actual modulus,

temperature shift factor was based on the actual temperature, and contributes to the reduced loading time with actual loading time. For target modulus, since the target temperature was the reference temperature 90°F, the temperature shift factor was 1, and the target loading time equaled to the reduced loading time.

In the manual adjustment of temperature and speed, the frequency was reduced according to the actual temperature and speed, and the actual resilient modulus was obtained according to the master curve. However, how to derive the corresponding strain change was a big issue. Even if the pavement was treated as a linear elastic material, strain at a certain point didn't change in a simple reciprocal relation with pavement modulus, because of the complicated boundary condition, the nonlinear distribution of the stress, and others.

The pavement analysis software "WinLEA" was used to simulate the relationship between resilient modulus and strain for different offset distance in the first stage of the project. However, WinLEA can only analyze the linear elastic material and uniformly distributed circular tire pressure. As we known, the behavior of asphalt concrete in hot weather was far away from a linear elastic material property, which could lead to a big difference of the prediction to the actual performance. At the same time, the load of the tire was also not uniformly distribution. The interface of WinLEA is shown in Figure 62. In the first year of the project, since 3D-Move was not ready for analysis, WinLEA was used to derive the relationship between modulus and strain distribution.

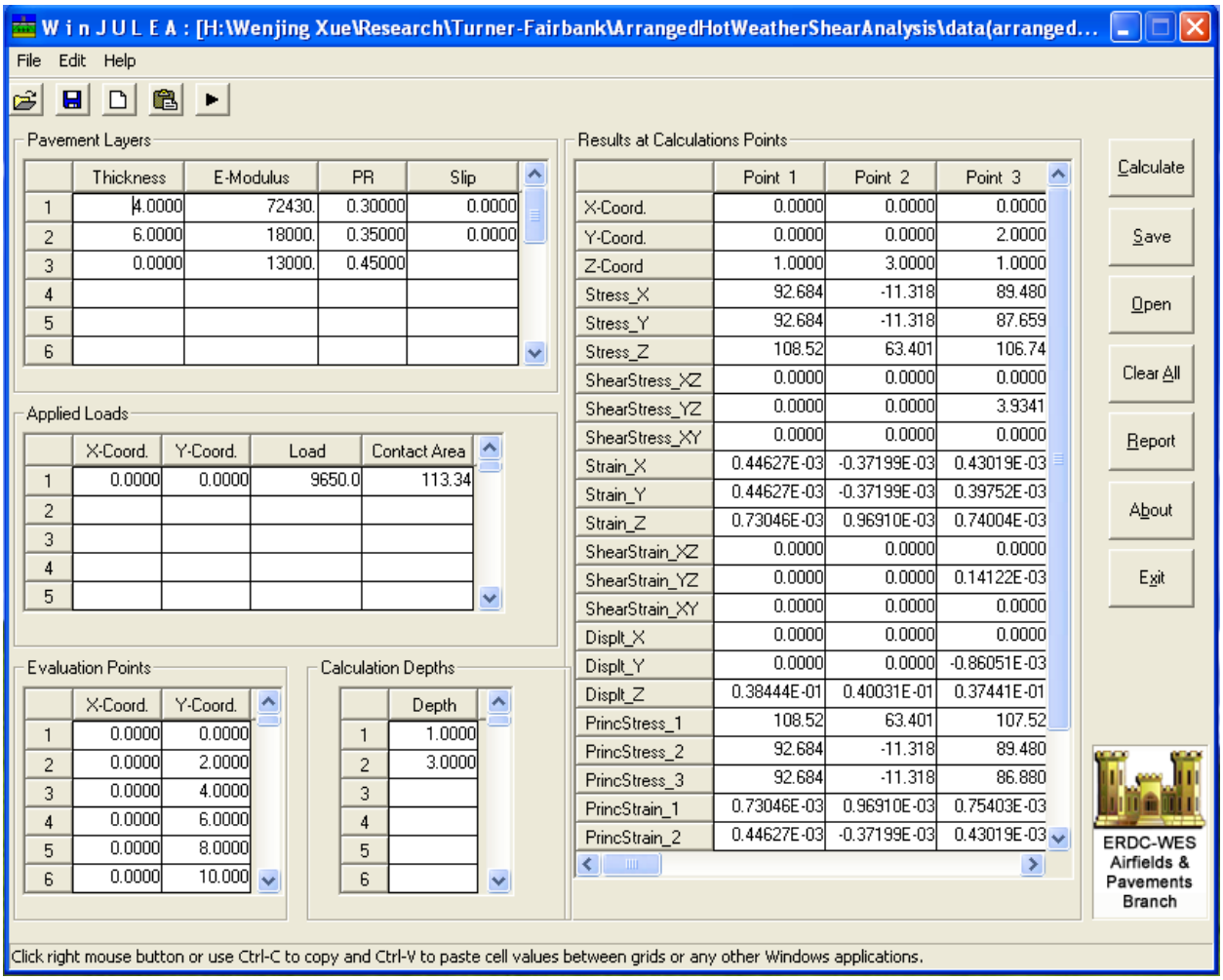

Figure 62: User Interface of the software WinLEA

3D-Move, which is released by the University Nevada Reno, is new software for analysis of asphalt pavement. The continuum-based finite-layer approach is used to compute pavement responses. The 3D-Move model can take moving loads, three dimensional contact stress distribution of any shape, and viscoelastic material characterization for the pavement layers into account, which was good and convenient for the experiment. The interface of 3D-Move is shown in Figure 63.

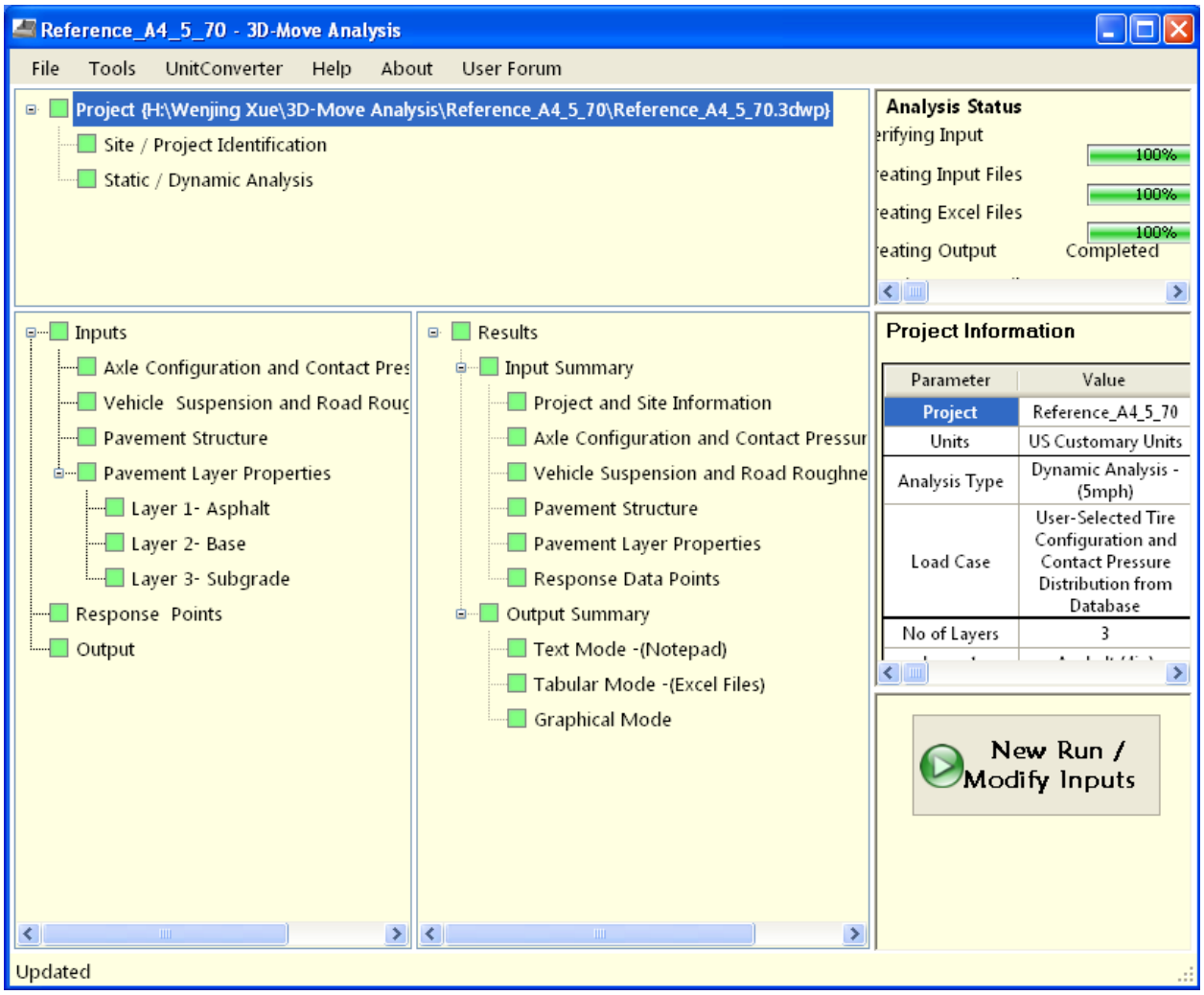

Figure 63: User Interface of the software 3D-Move

After the pavement analysis with different Young's Modulus, the relationship between Modulus and shear strain was found dependent on the offset distance, which meant that the target relationship curve was different for every points in the transverse plane, as shown in Figure 64.

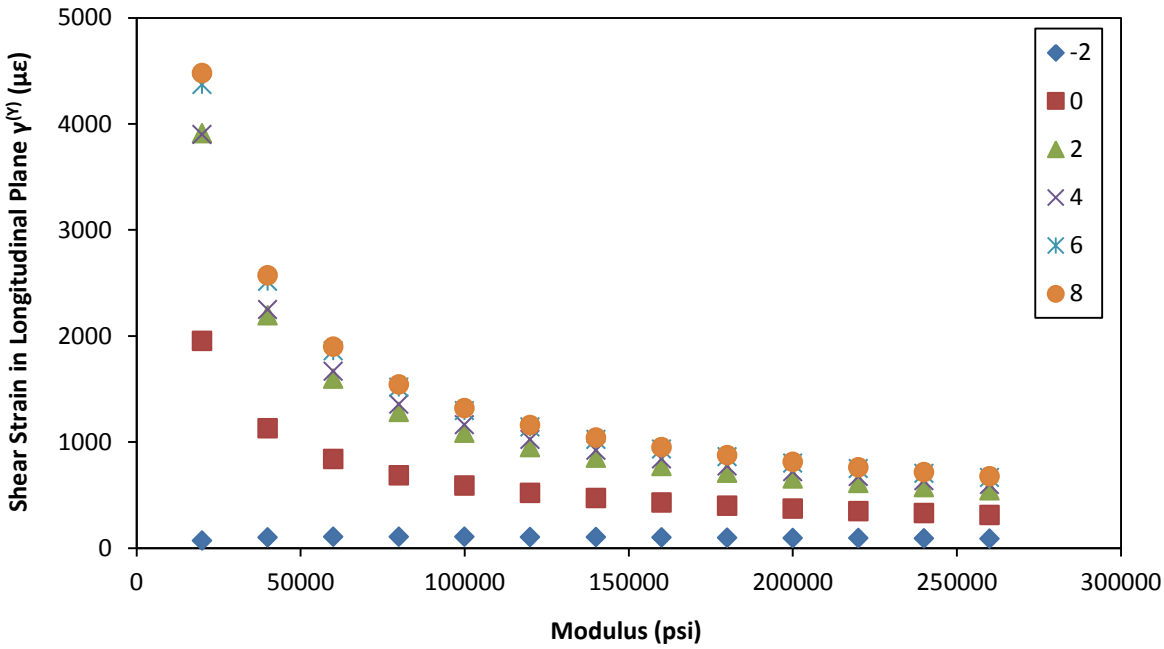

Figure 64: Relationship between shear strain and modulus via offset distance

Top of 4'' AD, GoodYear wide-base

As shown in Figure 64, shear strain in pavement decreased with elastic modulus, following different curves with different offset distances. To obtain the relationship between modulus and strain for each run with a specific offset distance, linear interpolation was made between adjacent offset distances and modulus for the ratio of adjusted strain and original strain.

In general, with the dynamic modulus master curve at the reference temperature (90 ^{o}F), the modulus under any temperature and loading rate can be calculated. First, temperature shift factor can be interpolated for the actual temperature. Then the reduced loading time is calculated with the temperature shift factor and the actual loading time as in Eq.(56). Target modulus and actual modulus can be calculated with corresponding reduced loading time as in Eq.(37). At last, the original PEAK TO PEAK strain responses are

adjusted according to the ratio of target modulus to actual modulus by interpolation of 3D-Move simulation results.

Adjustment for Offset Distance

Strain response changed in the transverse section, with the maximum strain just under the tire. The strain response decreased when the distance of the point to the tire increased. It was impossible to keep the center of the tire across every sensor, and offset distance was inevitable in each run. For localized monitoring system, it was impossible to measure the whole distribution of mechanical response in the transverse plane. It was fair to compare the effect of different loading conditions only if the mechanical response was adjusted to the same offset distance.

Manual Adjustment

It was very difficult to run the truck tire directly above the gages consistently especially at high speeds, and offset distance can't be avoided in this case. Due to the limited runs for each tire with a certain speed and tire inflation pressure, the differences among different speeds and tire inflation pressures were ignored in the adjustment process, and all the runs (including 3 speeds and 3 tire inflation pressures) were put together for distribution curve in the transverse section, as shown in Figure 65.

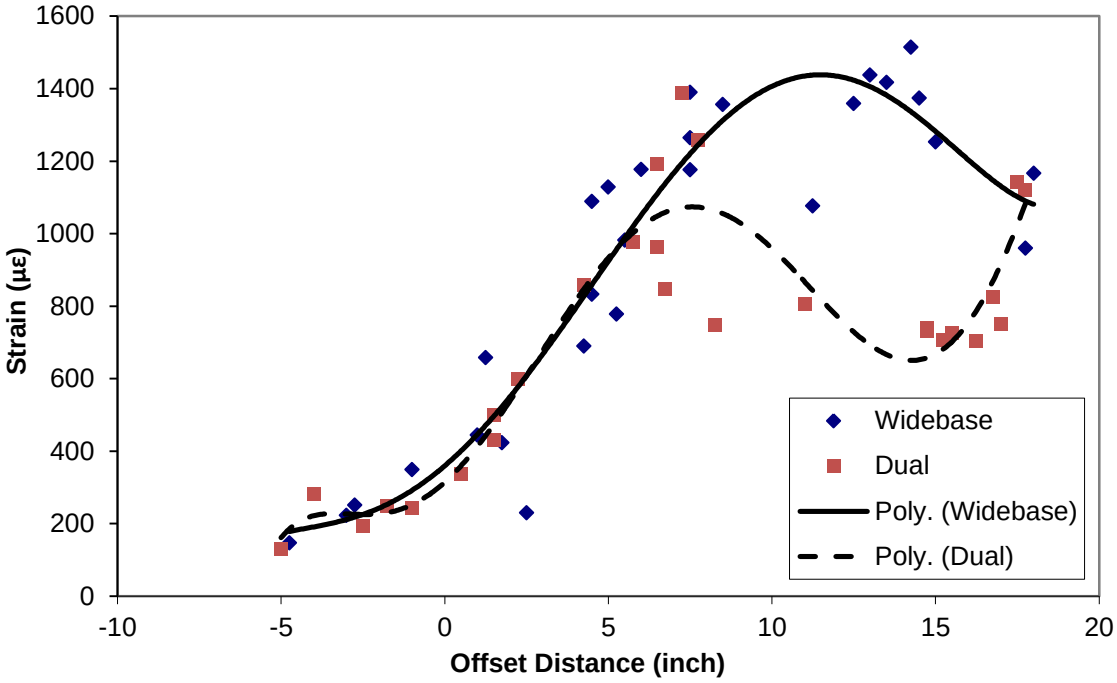

Figure 65: Offset distance's effect to WF1 strain for Michelin tires

Overviewing all the derived trend lines, the maximum strain response most commonly happens at the outer edge and the middle of the tires. To make consistent comparisons between tires, all strain values were adjusted to both the outer edge and the middle of the tire according to the proportional relationship:

$$S_{edge} = S(x_0) \cdot \frac{f(0)}{f(x_0)} \qquad \text{Eq.(66)}$$

$$S_{middle} = S(x_0) \cdot \frac{f(0.5w)}{f(x_0)} \qquad \text{Eq.(67)}$$

where, S_{edge} and S_{middle} are the corrected strains to the outer edge and middle of the tire; $S(x_0)$ is the measured strain response after temperature and speed adjustments at the

offset distance x_0; $f(x)$ is the function of the trend line via offset distance x; w is the width of the corresponding tire.

Adjustment with 3D-Move

3D-Move Analysis can account for many important but complicated factors such as moving loads, arbitrary stress distribution in the contact area, and viscoelastic material characterization.

The tire interface pressure data was collected under a separate FHWA project for all tires used in this experiment[70]. Part of this data has been incorporated into the input library of the 3D-Move viscoelastic pavement response software. These actual loading distributions were used in the pavement response modeling, and compared with circular uniform loading with 3D-Move under various loading conditions. The measured actual loading distributions indeed induced different pavement response from circular uniform ones, and the difference changed with the location of the point. To better display the difference, shear strain distributions under actual measured loading and uniform circular loading are displayed in Figure 66.

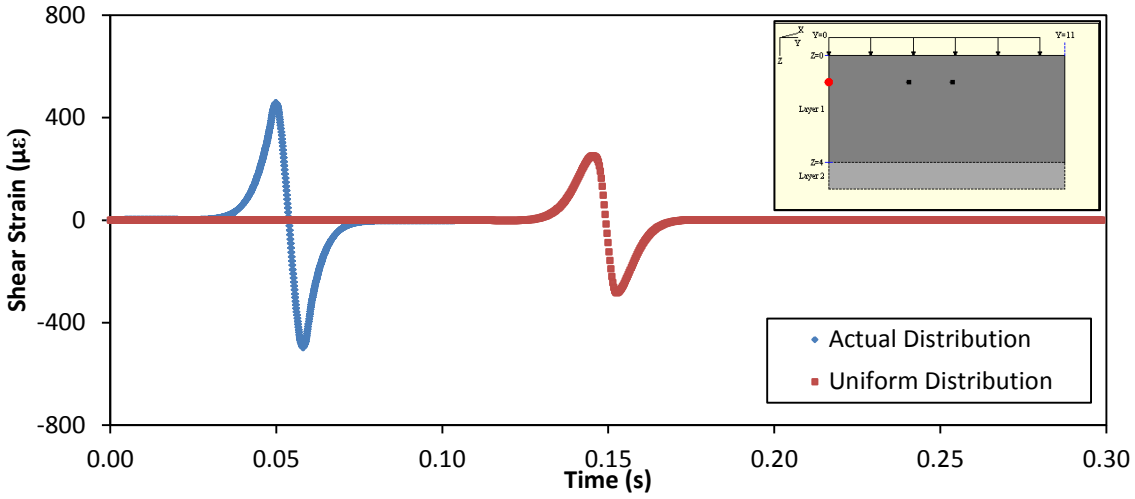

(a) 0” Offset Distance

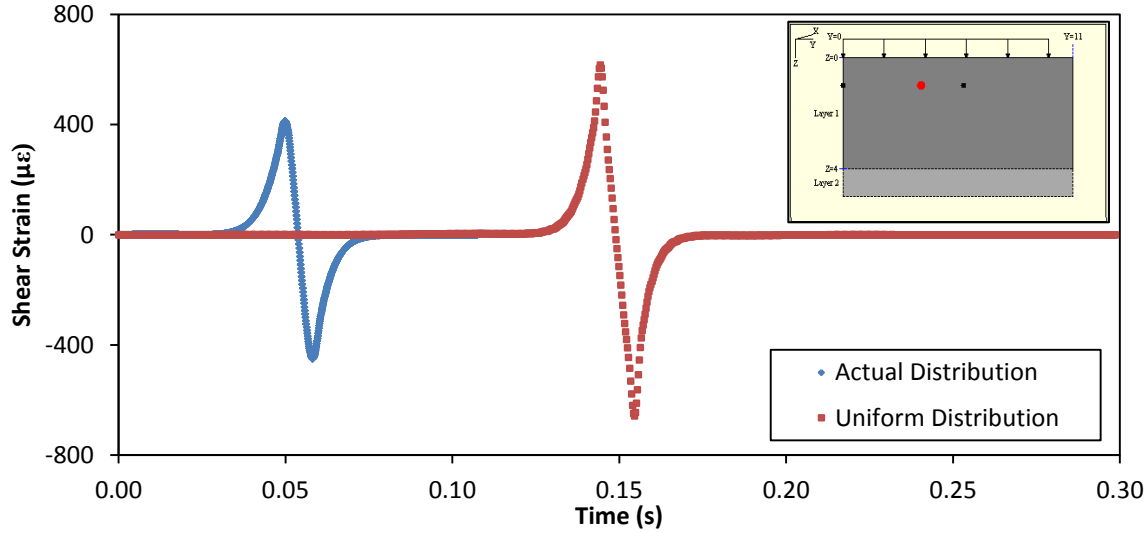

(b) 3.75’’ Offset Distance

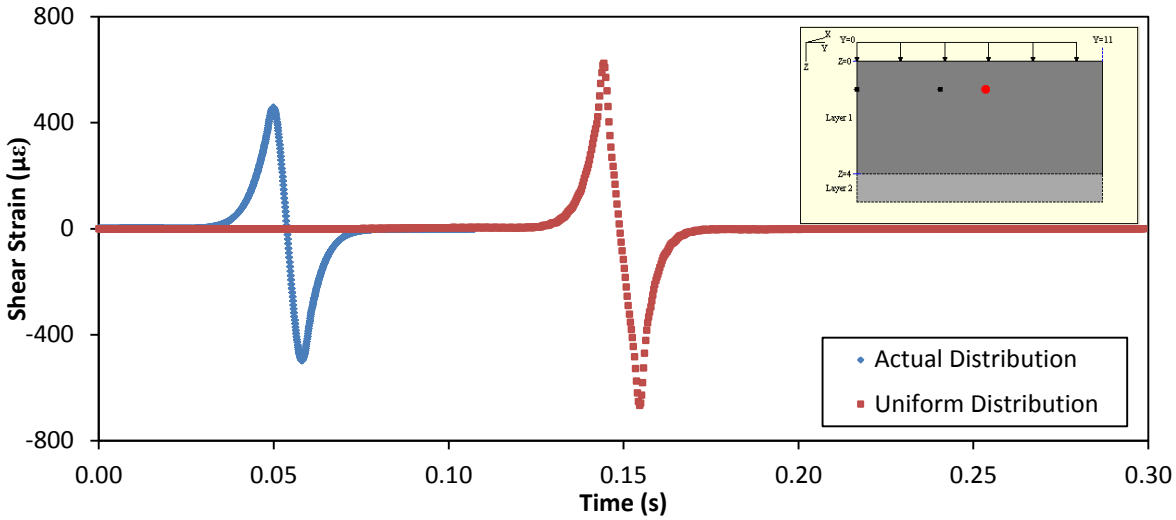

(c) 5.75'' Offset Distance

Figure 66: Shear strain distribution under the actual and uniform load.

Top of 4'' AC, GoodYear wide-base, run#1, 55 mph ,120 psi,

According to the comparison in Figure 66, if the measured actual load was replaced by uniform load, which is common in actual projects, the shear strain response at the edge of the tire would be much smaller than the actual one, and as a result, certain severe pavement response at the edge, which can damage the pavement, might be ignored.

Due to the many advantages, 3D-Move was used to simulate the whole loading process numerically. The experimental pavement was modeled in the software, and the corresponding tire interface pressure data, which had been incorporated into the input library of 3D-Move, was applied on the viscoelastic pavement model with the corresponding temperature and speed. The calculated process of strain response matched the measured ones well in the shape, but the difference of magnitude existed, as shown in Figure 67.

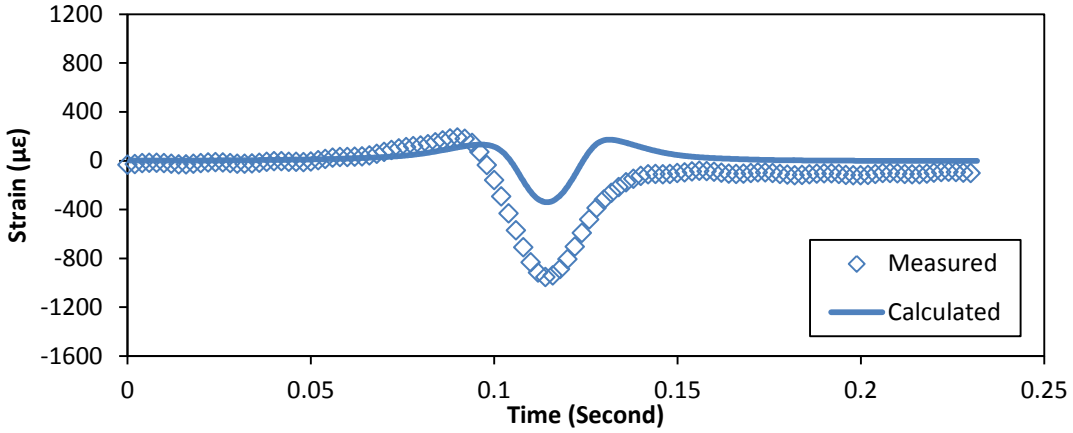

(a) Horizontal Strain Response $\varepsilon_X^{(Y)}$

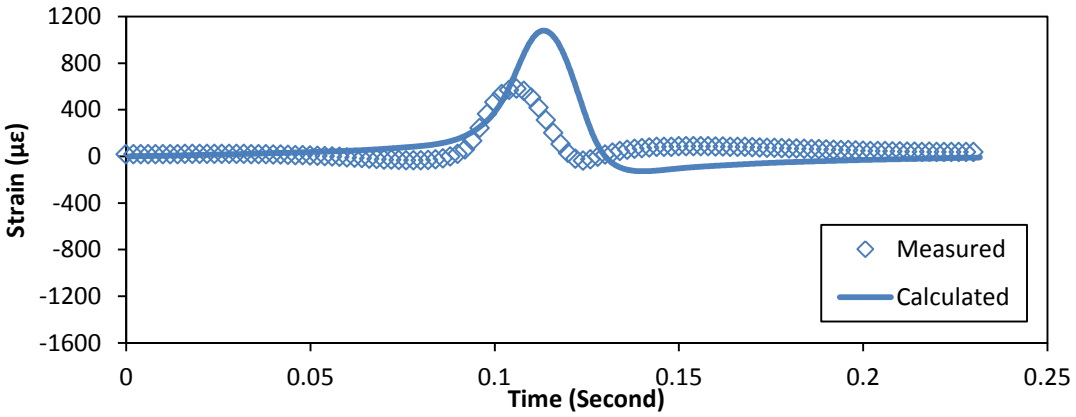

(b) Vertical Strain Response $\varepsilon_Z^{(Y)}$

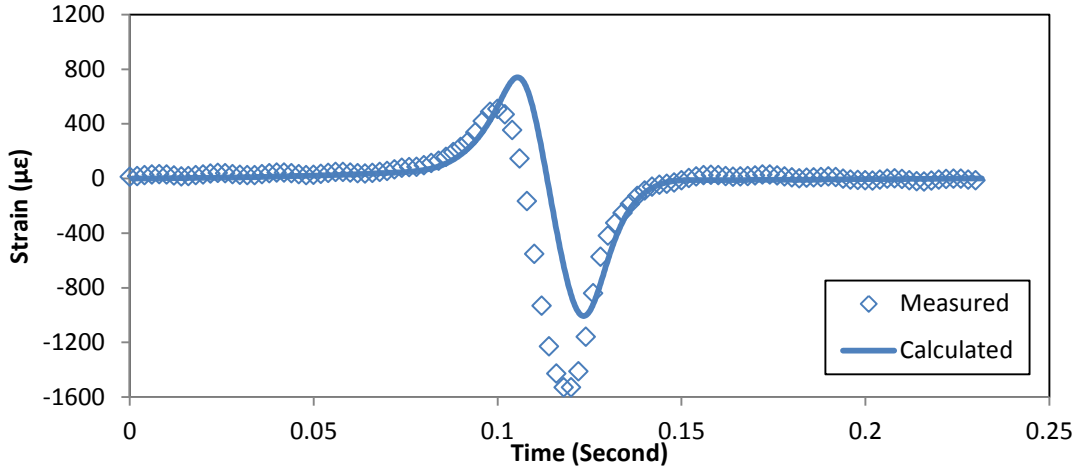

(c) Shear Strain Response $\gamma^{(Y)}$

Figure 67: Comparison between Measured and 3D-Move Calculated Strain Traces

The case shown in Figure 67 was very typical in the calculation: the calculated horizontal strain was smaller than the measured data, but calculated vertical strain was bigger than the measured one. The main reason might include the inaccuracy of the modulus of the base material and the anisotropy of asphalt concrete.

In addition to predicting strain traces, 3D-Move was also tried in offset distance adjustment for a potential better method. Each experimental run was simulated in 3D-Move and compared with the simulation under reference temperature, target speed and zero offset distance. The ratio was used to adjust the measurement for final unbiased comparison. The comparisons between manual and 3D-Move adjusted shear strain are listed in Figure 68 separately with different tire inflation pressures.

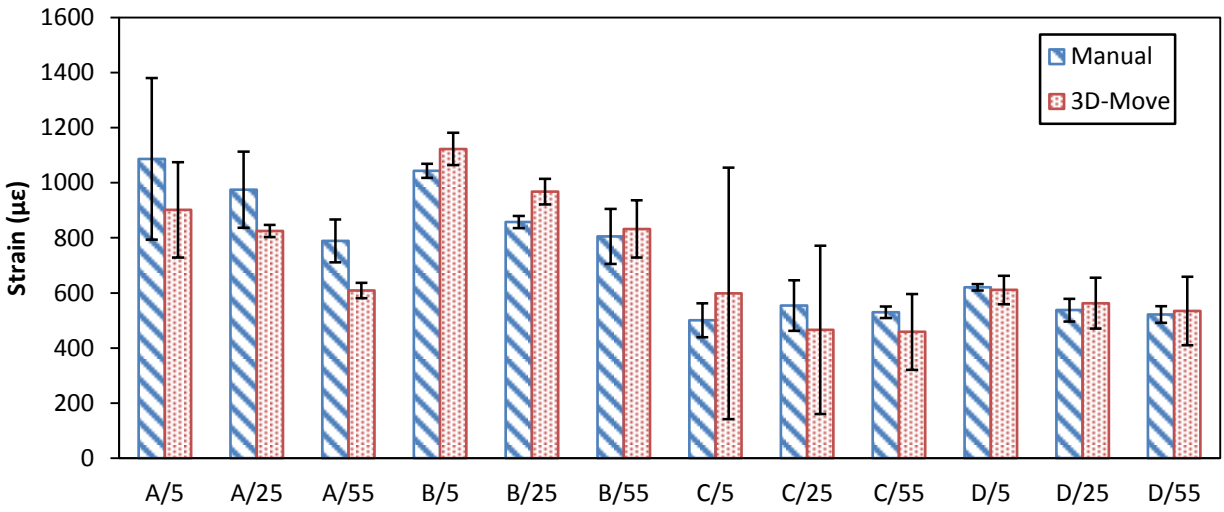

(a) Horizontal Strain $\varepsilon_X^{(Y)}$

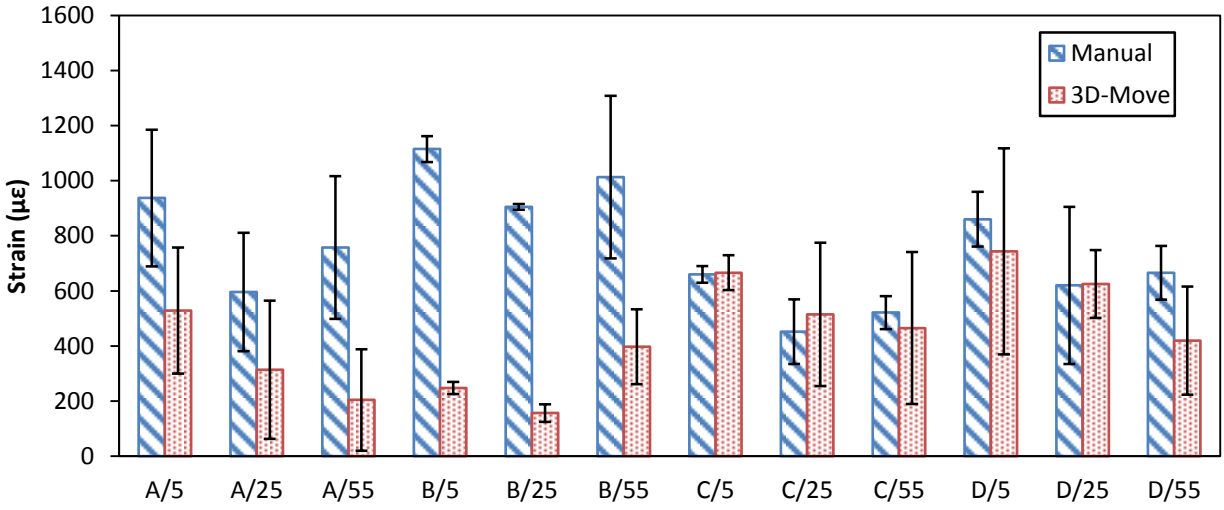

(b) Vertical Strain $\varepsilon_Z^{(Y)}$

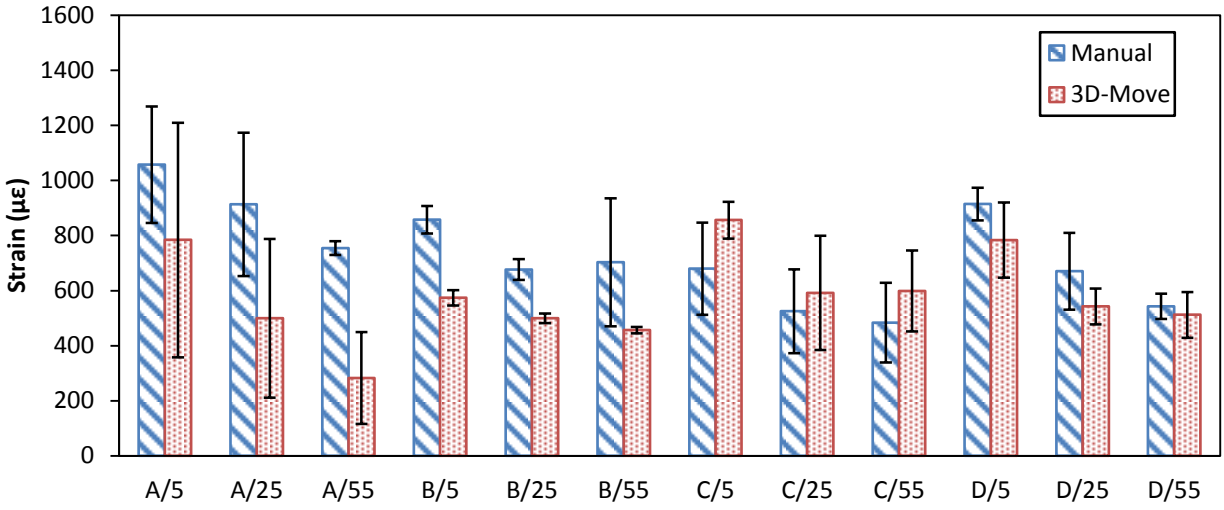

(c) Shear Strain $\gamma^{(Y)}$

Figure 68: Adjusted Strain with Manual Method and 3D-Move.

Tire Types: A, B, C, D. Speed: 5, 25, 55 (mph)

120 psi, 4'' pavement, 3'' depth, longitudinal plane

According to the comparison above, strain in various directions present similar trends but different magnitudes for the two methods except for the vertical strain of GoodYear Dual Tire. The standard deviation of both methods fluctuated a lot, but some of the 3D-Move

adjustments were obviously bigger than others. After all, the results of two adjustments were very close in spite of some differences.

To determine which method adjusted offset distance better, the distribution curves in transverse plane (X-Plane) of the two methods are present together with corresponding measurements after temperature and speed adjustments in Figure 69.

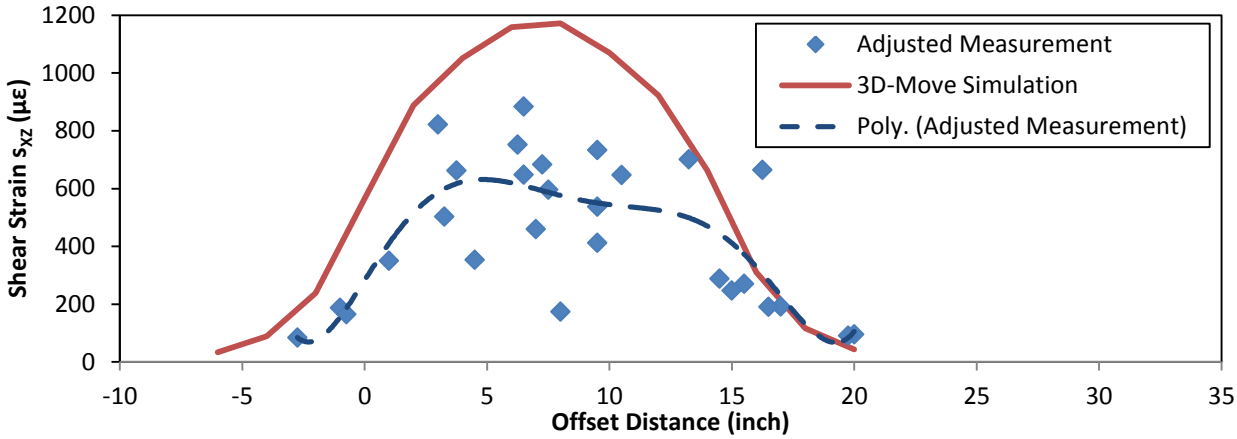

(a) Shear Strain $\gamma^{(Y)}$ of Michelin Wide-Base Tire

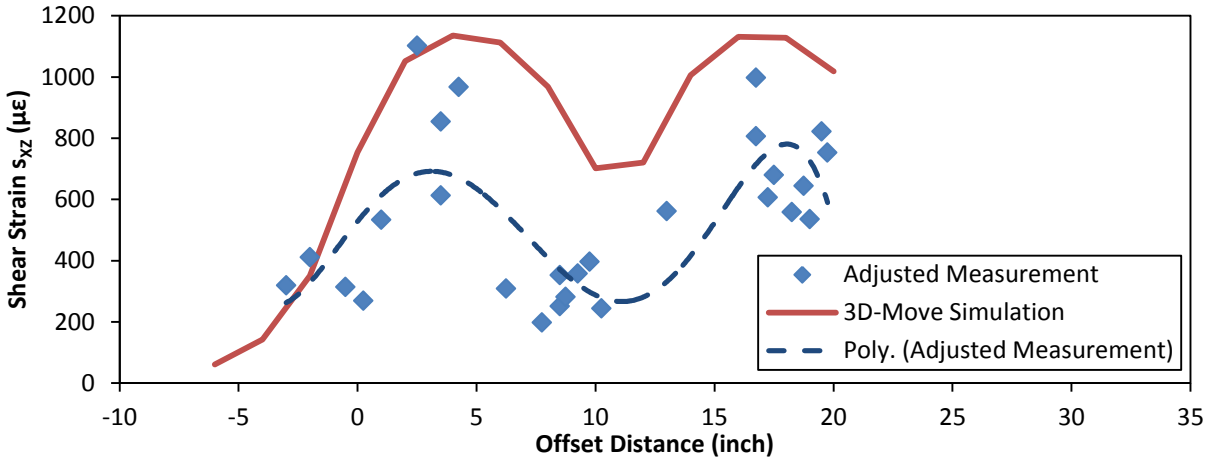

(b) Shear Strain $\gamma^{(Y)}$ of Michelin Dual Tire

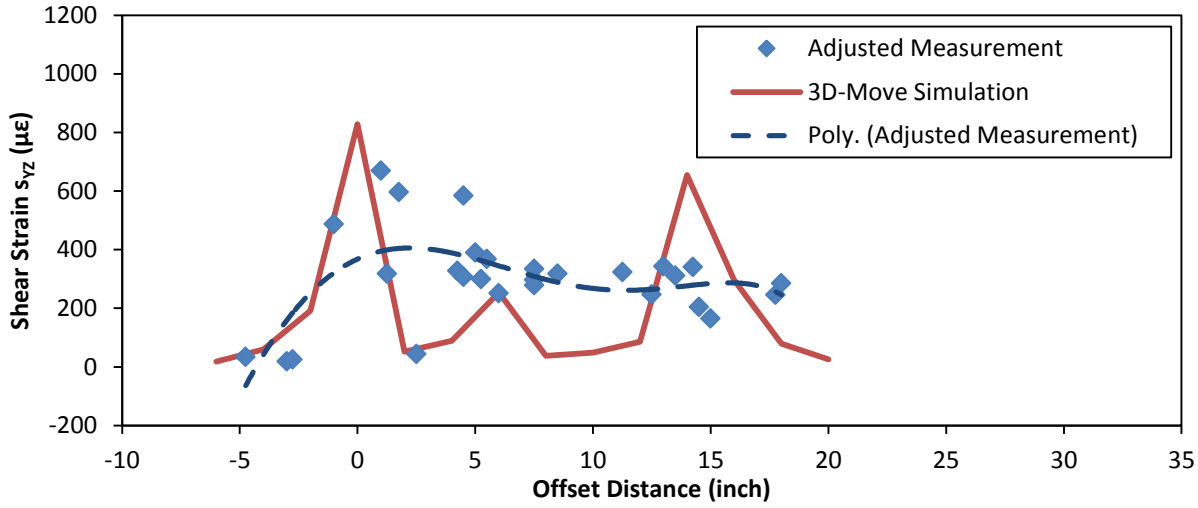

(c) Shear Strain $\gamma^{(X)}$ of Michelin Wide-Base Tire

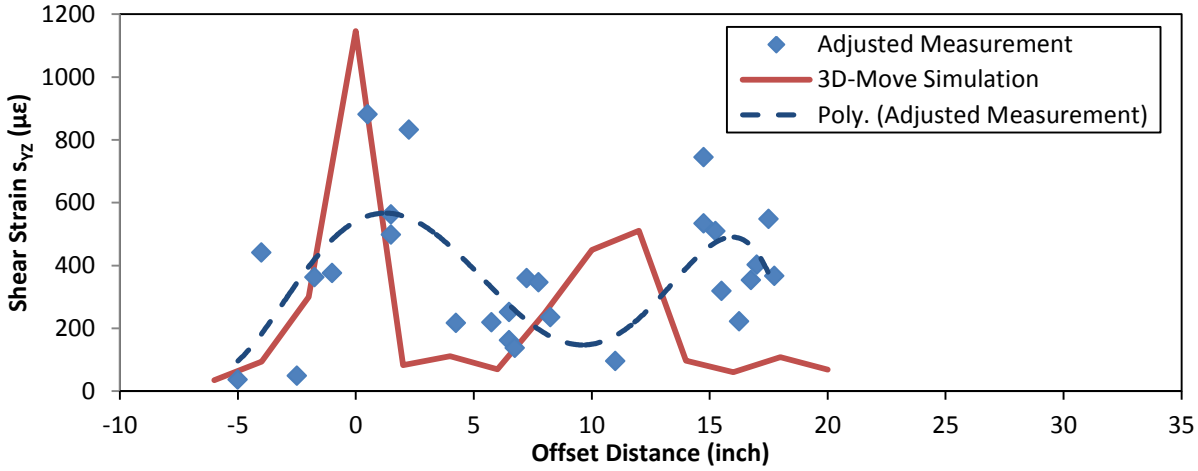

(d) Shear Strain $\gamma^{(X)}$ of Michelin Dual Tire

Figure 69: Distribution of Adjusted Shear Strain with Manual Method and 3D-Move.

Based on the comparisons in Figure 69, 3D-Move simulated better distribution of shear strain in longitudinal plane (X-Plane) than transverse plane (Y-Plane). The trend line given by 3D-Move was always sharp and turbulent, and the adjusted measurement presented a flatter and gentle distribution over offset distances. The detailed reason for the disagreement has not been figured out, and once did, both 3D-Move software and the adjusted method present in the paper will be improved and refined. More 3D-Move

predicted strain distributions at different locations of pavements were summarized in Appendix B.

For an unbiased and objective evaluation of the strain response in pavement by different tire configurations, trend lines of manual method was adopted because it was based on the on-site measurement and can present the actual strain distribution more objectively. All the results after offset distance adjustments referred to manual offset distance adjustment in the following chapters.

Strain Distribution

The response of the pavement changed with depth, including the direction, the magnitude and the shape of the strain traces. In Ohio experiment, both the top and bottom of the pavements, including 4 inch and 8 inch ones, were covered, as shown in Figure 3.

Best Sensing Location to Compare Loading Conditions

As powerful pavement response analysis software, 3D-Move can be used to predict strain distribution throughout the pavements. Shear strain was chosen to reveal the difference between different locations in pavements. Comparisons about shear strain responses at different locations in the pavements are made in Figure 70.

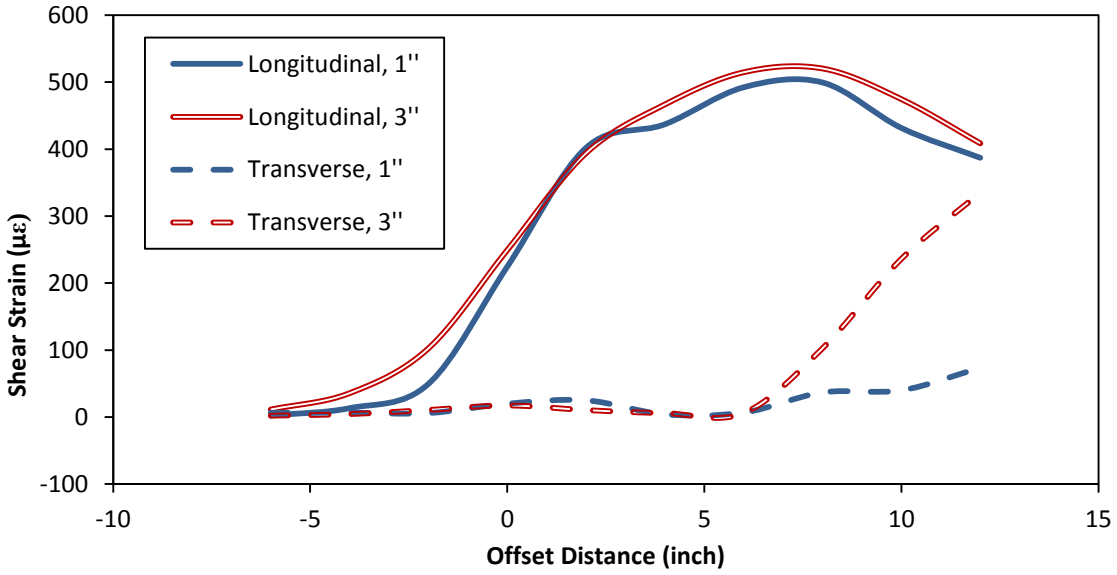

(a) Wide-base Tire on 4 inch Pavement

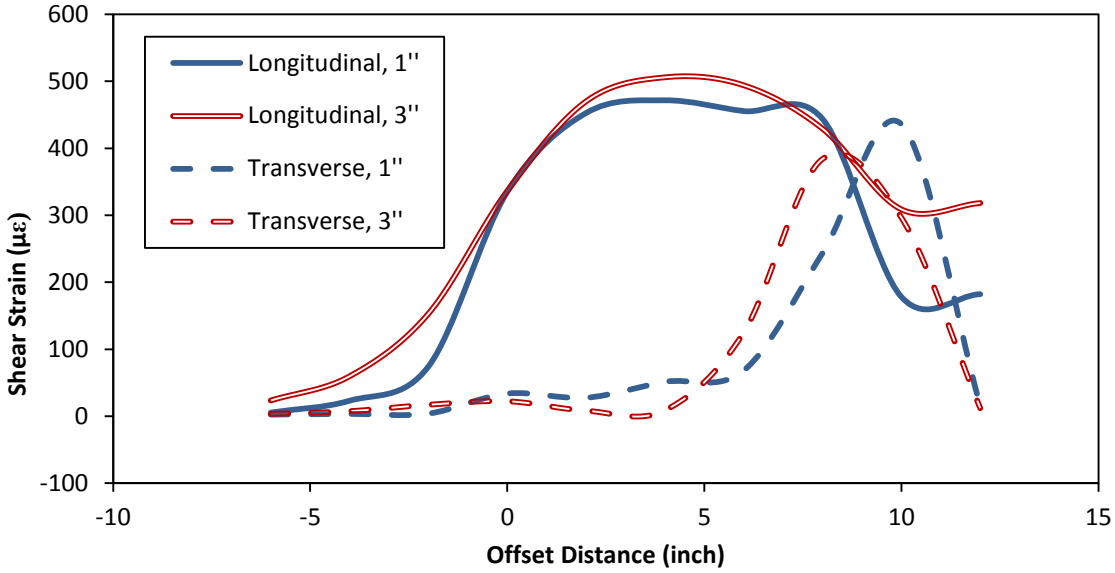

(b) Dual Tire on 4 inch Pavement

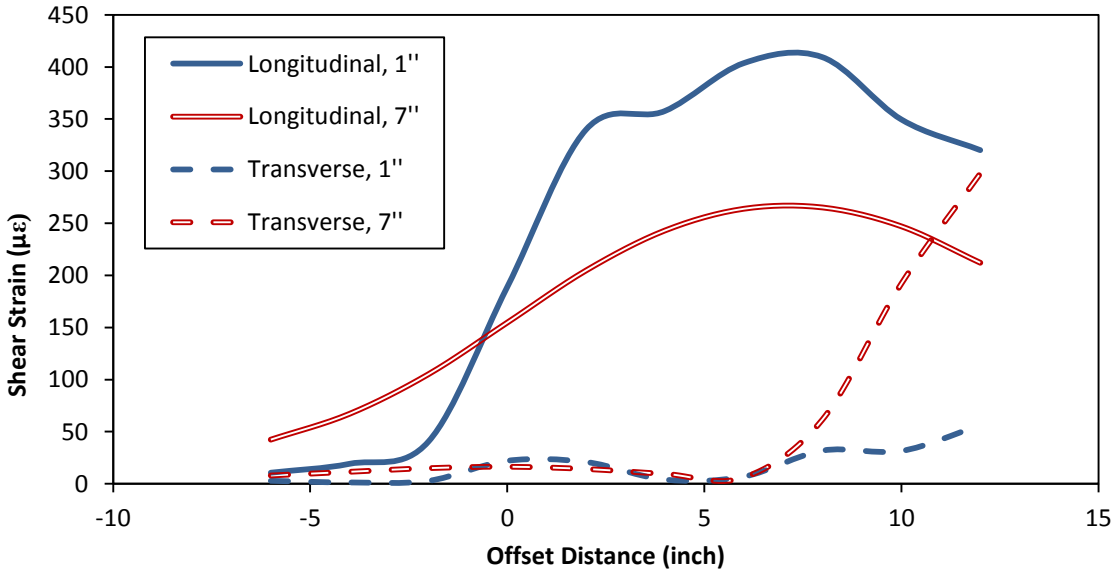

(c) Wide-base Tire on 8 inch Pavement

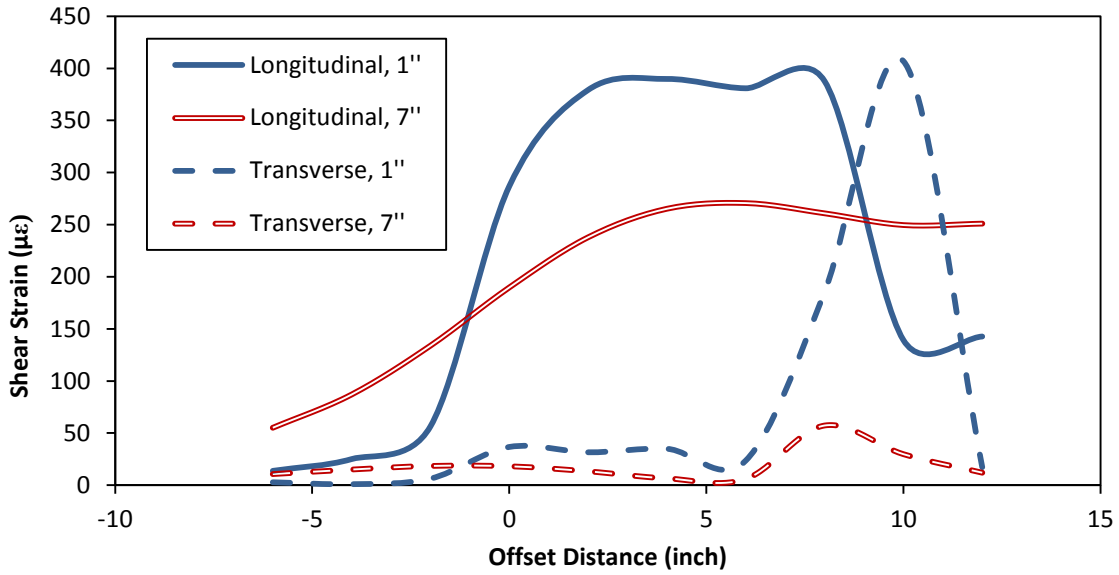

(d) Dual Tire on 8 inch Pavement

Figure 70: 3D-Move Predicted Shear Strain Distribution

Load distribution from GoodYear wide-base and dual tires, 25 mph, 100 psi

As shown in Figure 70 (a-b), the shear strain in the transverse plane was much smaller and sharper than the longitudinal one, which meant that a little error in the original measured strain would be enlarged a lot when it was adjusted to the maximum value in the whole loading area. So according to the distribution of longitudinal and transverse shear strain, the conclusion was that the shear strain in the longitudinal plane is better to tell the difference of loading, in another word, the effect of various tires to the pavement.

Comparing the strain distributions at different depth in Figure 70, the distribution curves of shear strain at the bottom of the pavements were much milder than the ones at the top. The drastic fluctuations at the top might induce unreasonable error during the process of the offset distance adjustment. So theoretically, the adjustments with the distribution curve at the bottom of the pavement might have higher accuracy.

According to theoretical calculation, the shear strain in 4 inch pavement is larger than that in 8 inch pavement both at the top and the bottom, as shown in Figure 70, because of the stress transfer over the depth of the pavement.

To verify the conclusion above, all the available shear strains (two longitudinal and 2 transverse) under various tires loading were adjusted with 3D-Move simulation, and the statistics of the results are concluded as in Table 14. A few unbelievable results, which were far beyond reasonable range, were caused by the small error enlargement and deleted as outliners. The less was the average standard deviation; the better was the adjustment, since it means the adjustments for temperature, offset distance and speed, match well between different runs.

Table 14: Standard Deviation of Adjusted Shear Strain with 3D-Move

	4 inch Pavement				8 inch Pavement			
	Longitudinal		Transverse		Longitudinal		Transverse	
	Top	Bottom	Top	Bottom	Top	Bottom	Top	Bottom
GoodYear Widebase	216.3	133.5	288.1	454.7	164.6	152.9	650.8	515.3
GoodYear Duals	163.7	115.5	314.3	256.6	279.1	78.0	836.6	363.9
Michelin Widebase	263.8	106.4	729.2	256.5	308.9	76.3	674.5	144.1
Michelin Duals	105.2	114.8	216.8	584.1	114.0	86.6	529.7	336.0

As shown in Table 14, the average standard deviation of adjusted shear strain in longitudinal plane was much lower than that in transverse plane for all the monitoring points throughout 4 inch and 8 inch pavements. At the same time, the standard deviations of the adjusted shear strain at the bottom of the pavement were much less than those at the top. The standard deviation of adjusted measurements validated the assumptions above: the strain distribution in the longitudinal plane at the bottom of pavements is the

most stable and wild with the least drastic fluctuations, and most suitable to tell the differences between loading conditions.

In conclusion, from the perspective of telling the difference between tire configurations, the best sensing location was in the longitudinal plane at the bottom of pavements, because the responses were more stable and convergent, and the responses match with viscoelastic analysis the best. Theoretically, increasing the thickness of pavement reduced the shear strain responses and increases the pavement performance as a result.

Adjusted Strains with Different Tire Configurations

The main target of Ohio experiment was to compare the potential damage brought to the pavement by different kinds of tires. To satisfy time and space constraints, only the experimental condition including the speed of 25 mph and tire inflation pressure of 100 psi (689.5 kPa) was used to reveal differences between tires. The raw data without any adjustments are summarized in Table 15.

Table 15: Summary of original strain measurements

		4 inch Pavement				8 inch Pavement			
		A	B	C	D	A	B	C	D
ε_X	Top	190.6	639.5	562.5	379.8	240.6	184.1	319.8	201.6
	Bottom	1083.4	930.7	749.0	520.9	286.4	260.2	326.2	244.4
ε_Y	Top	215.7	273.7	305.4	162.6	469.0	621.2	801.5	600.9
	Bottom	264.4	178.9	228.3	209.2	188.1	87.7	164.0	106.9
ε_Z	Top	137.0	306.6	359.8	227.5	532.8	630.8	1121.7	709.0
	Bottom	446.8	524.1	593.1	444.2	280.2	309.5	482.0	341.2
γ_{XZ}	Top	289.3	839.9	758.0	542.6	447.2	352.8	662.7	387.2
	Bottom	974.0	169.6	477.5	364.1	475.8	374.7	591.0	387.6
γ_{YZ}	Top	393.8	300.7	313.7	276.3	539.4	339.5	646.8	394.1

	Bottom	385.0	469.8	561.2	433.6	374.1	177.8	244.1	257.4

All as-measured strains were subject to the time, temperature and lateral offset distance adjustments described in previous sections. To make a consistent comparison of tires, the strains after temperature and speed adjustment were adjusted to the outer edge and middle of the tires, summarized separately in Table 16.

Table 16: Summary of adjusted strain measurements

		4 inch Pavement				8 inch Pavement			
		A	B	C	D	A	B	C	D
Edge of the Tires									
ε_X	Top	67.4	656.6	244.2	328.3	67.4	656.6	244.2	328.3
	Bottom	344.0	625.1	573.3	565.3	344.0	625.1	573.3	565.3
ε_Y	Top	14.5	107.7	146.3	187.2	14.5	107.7	146.3	187.2
	Bottom	182.9	189.0	118.1	175.3	182.9	189.0	118.1	175.3
ε_Z	Top	19.6	157.5	112.2	243.0	19.6	157.5	112.2	243.0
	Bottom	75.8	403.7	218.2	297.1	75.8	403.7	218.2	297.1
γ_{XZ}	Top	136.8	441.2	329.1	597.5	136.8	441.2	329.1	597.5
	Bottom	394.4	282.2	421.6	425.6	394.4	282.2	421.6	425.6
γ_{YZ}	Top	113.5	186.6	318.8	347.4	113.5	186.6	318.8	347.4
	Bottom	12.8	236.3	492.2	526.1	12.8	236.3	492.2	526.1
Center of the Tires									
ε_X	Top	224.0	606.4	579.0	667.3	217.4	199.1	325.5	256.8
	Bottom	974.9	857.1	554.1	537.7	431.0	226.9	118.3	185.6
ε_Y	Top	75.0	202.9	341.4	224.7	515.1	611.3	762.5	714.0
	Bottom	313.0	202.2	115.7	225.4	266.5	56.7	46.2	54.4
ε_Z	Top	182.7	117.0	202.4	387.4	468.4	603.2	809.3	986.4
	Bottom	399.9	394.4	282.2	443.6	911.1	440.5	191.2	298.2
γ_{XZ}	Top	680.7	439.1	488.5	796.0	251.6	274.3	502.7	543.4
	Bottom	71.8	196.2	273.1	521.5	942.3	459.3	303.6	355.7
γ_{YZ}	Top	192.7	156.4	181.1	329.9	212.1	394.9	455.7	493.7
	Bottom	312.4	560.3	327.7	465.9	250.4	273.4	125.0	219.5

The difference between tires and sensor locations was evident in the results presented in Table 16. The strains adjusted to the middle of the tires were mostly higher than those adjusted to the edge of the tires. For easier comparison, the adjusted strain at outer edge and middle of tires were compared, and the maximum response is plotted in Figure 71.

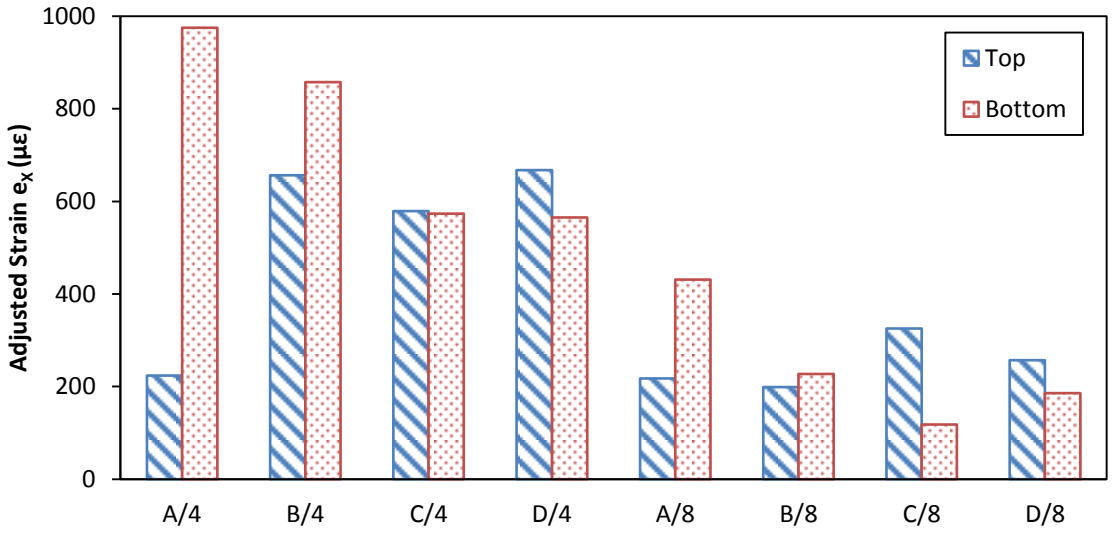

(a) Horizontal Strain in Longitudinal Plane $\varepsilon_X^{(Y)}$

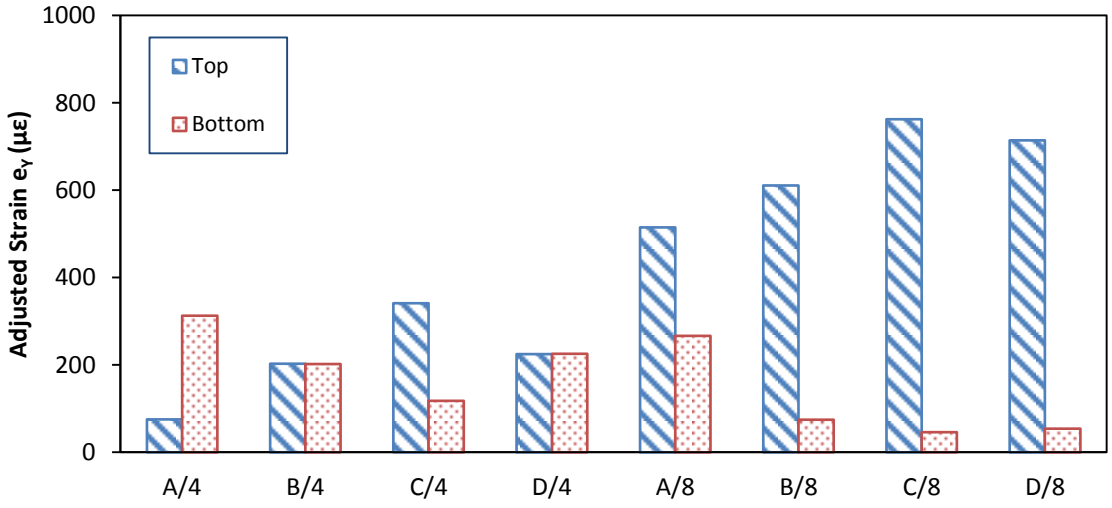

(b) Horizontal Strain in Transverse Plane $\varepsilon_Y^{(X)}$

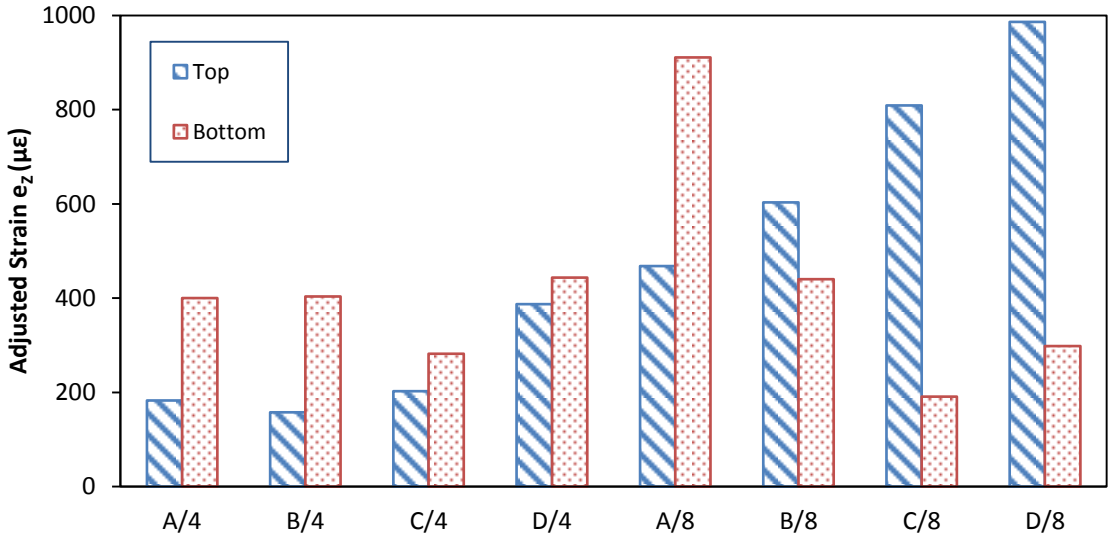

(c) Vertical Strain ε_Z

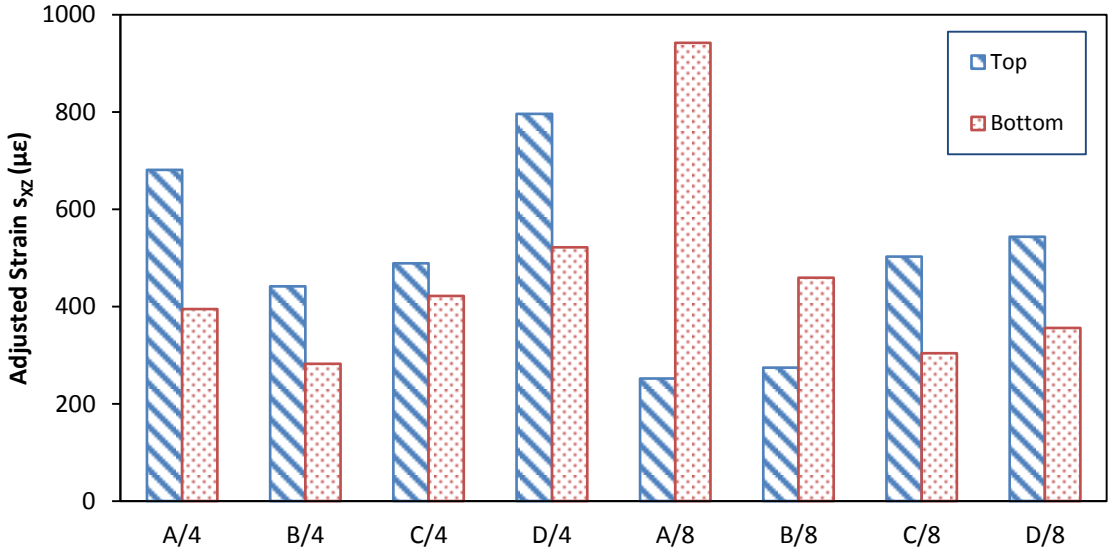

(d) Shear Strain in Longitudinal Plane $\gamma^{(Y)}$

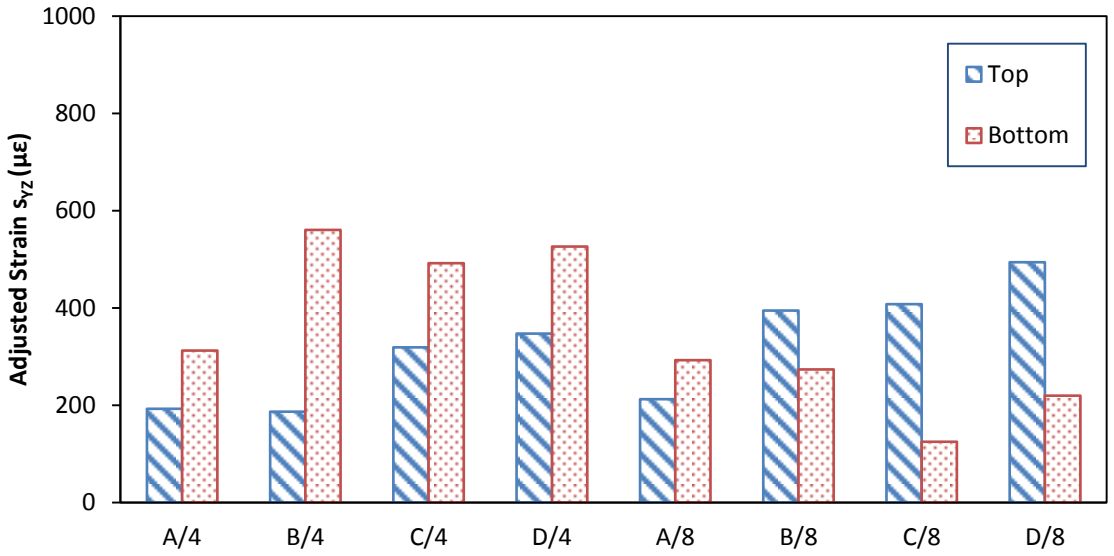

(e) Shear Strain in Transverse Plane $\gamma^{(X)}$

Figure 71: Adjusted Strain for Different Tires (A, B, C, D) in 4" and 8" Sections

100 psi, 25 mph

Based on the research about pavement permanent distress in the passing decades[67], fatigue pavement damage is caused by the tensile strain at the bottom of HMA layer, and the primary rutting in HMA layer is correlated to the ratio of permanent strain to recoverable stain. Endurance limit is defined as a pavement able to withstand 500 million design load repetitions in a 40-year period, and the 95% lower prediction of endurance limit varies from 75 to 200 microstrain[71].

According to the horizontal strain at the bottom of pavement sections, as shown in Figure 71(a-b), 8 inch pavement was close to being considered perpetual for all but tire type A. the tensile strain at the bottom of 4 inch pavement was mostly more than 2 times of the tensile strain in 8 inch pavement, which induced a much shorter fatigue life than 8 inch pavement. Wide-base tire A showed the largest tensile strain at the bottom of 4 inch and 8 inch pavement, which indicated high risk of fatigue cracking. On the contrary, the

lower tensile strain for dual tire B and D at the bottom of pavements would lead to a lower sensitivity to fatigue cracking and longer fatigue life.

Comparing the vertical strain in Figure 71(c), the vertical strain in 8 inch pavement was higher than 4 inch pavement, which might lead to a high rutting potential. Tire A and D induced higher vertical strain in 8 inch pavement, and had high rutting potential in 8 inch pavement. Due to the complexity of rutting prediction, the difference on rutting depth can be revealed only if the calculated strain is used in rutting models.

Adjusted Strains with Different Tire Inflation Pressures

Each kind of tire configurations ran 18 test series in the experiment, which were combinations of different tire inflation pressure, speed and thickness of pavement, as summarized in Table 4. The design of test series targeted the effect of speed and tire inflation pressure on the strain response distribution in pavements. To present the difference between test series, the unadjusted and adjusted shear strain responses of different test series are present in Figure 72 for the four tire configurations.

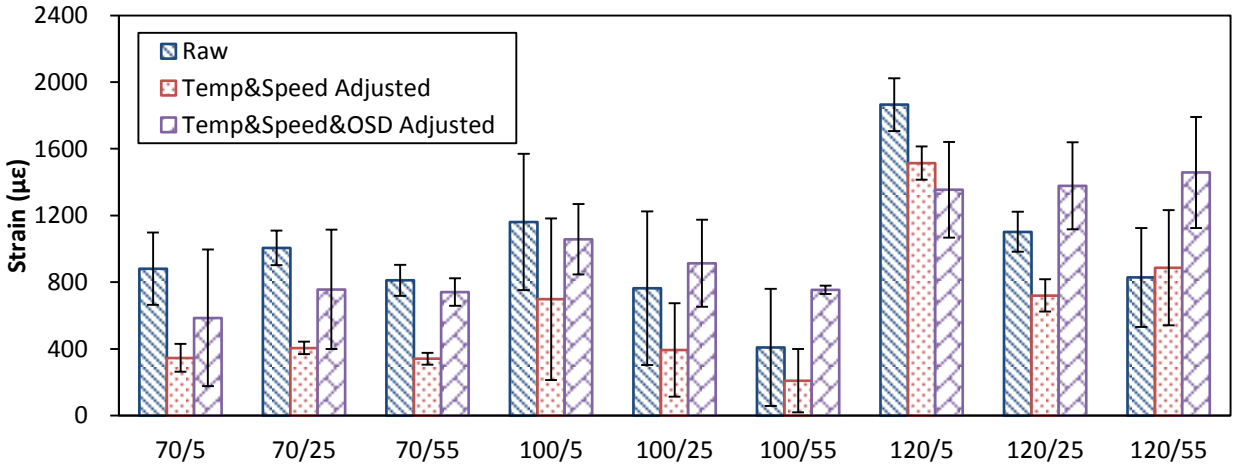

(a) GoodYear Wide-Base Tire

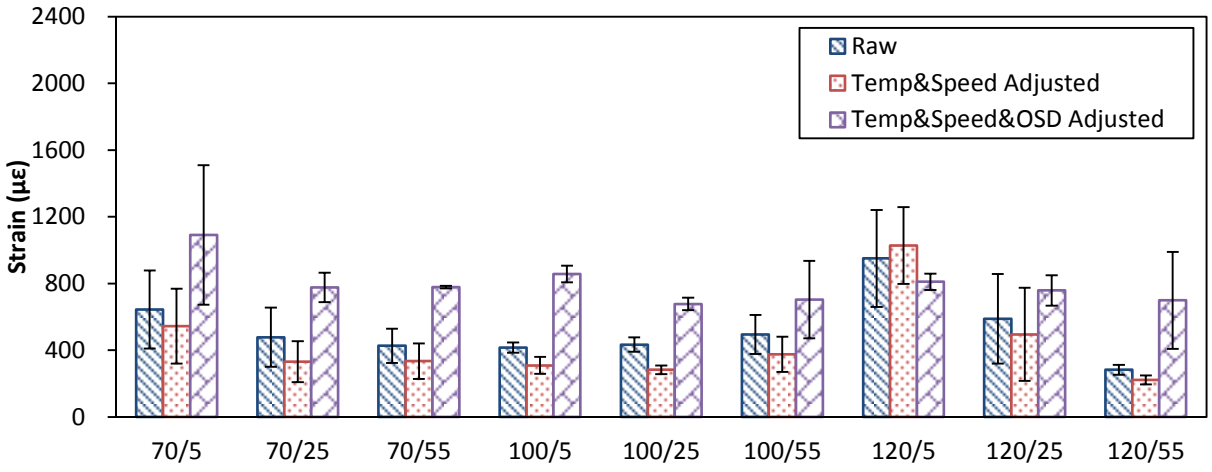

(b) GoodYear Dual Tire

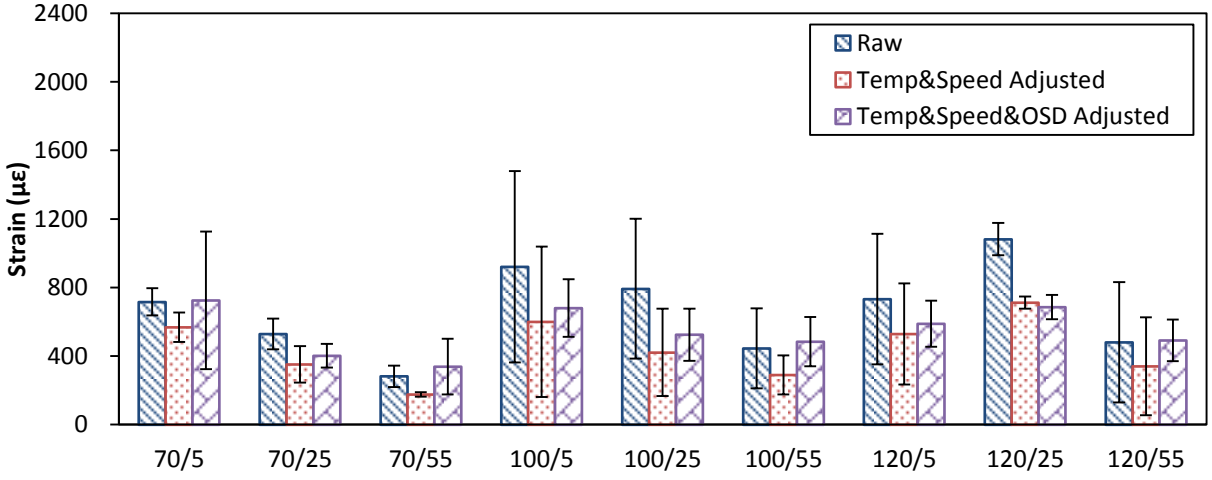

(c) Michelin Wide-Base Tire

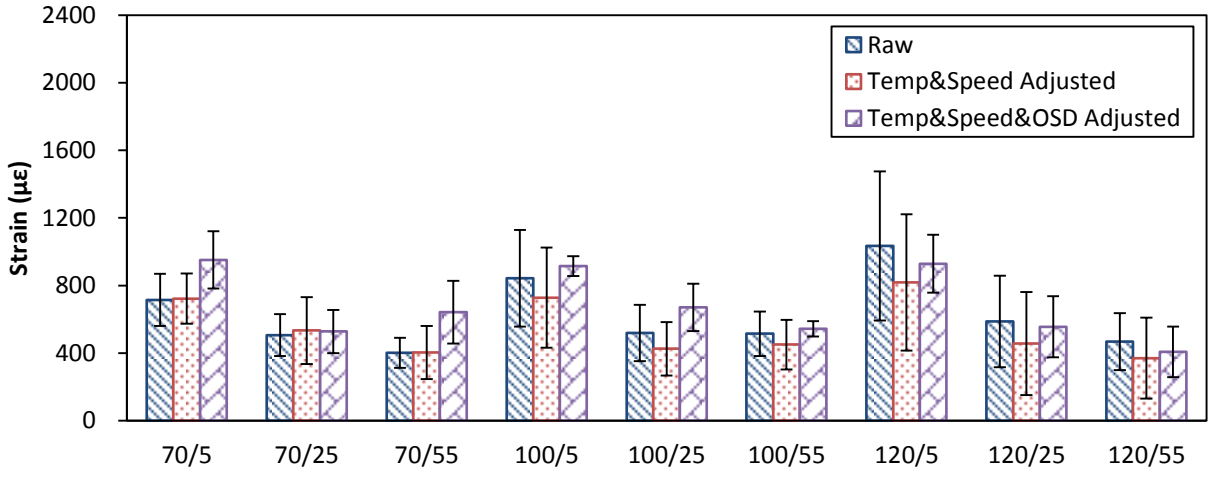

(d) Michelin Dual Tire

Figure 72: Raw and Adjusted Shear Strain for Different Test Series

(Tire Inflation Pressure: 70, 100 and 120 psi; Speed: 5, 25 and 55 mph)

Bottom of 4 inch AC, Shear Strain 19_20_21.

As compared in Figure 72, strain response decreased with increasing speed. The tire inflation pressure didn't make as much difference as speed. However, for the GoodYear wide-base tire, higher inflation pressure of 120 psi made the shear strain response much bigger than the lower pressure (70 and 100 psi). GoodYear wide-base tire induced larger shear strain response at the bottom of 4 inch asphalt concrete pavement, and strain response from different tire configuration was discussed in the previous section.

To evaluate the effect of tire inflation pressure on the strain response distribution in the pavement under different speeds, the maximum strains induced by Michelin Wide-base tire with different tire inflation pressures and speeds are summarized in Table 17.

Table 17: Maximum strains induced by Michelin wide-base tire

		Tire Inflation Pressure (psi) / Speed (mph)								
		70/5	**70/25**	**70/55**	**100/5**	**100/25**	**100/55**	**120/5**	**120/25**	**120/55**
4 inch AC										
ε_X	Top	916	857	789	682	579	722	556	616	795
	Bottom	856	620	509	518	573	548	562	476	485
ε_Y	Top	387	375	304	315	341	268	217	319	529
	Bottom	162	144	155	126	138	169	132	197	180
ε_Z	Top	277	528	262	272	208	213	234	316	210
	Bottom	373	356	301	399	287	297	361	283	318
γ_{XZ}	Top	861	699	596	845	488	624	736	647	711
	Bottom	568	352	206	653	476	340	544	712	406
γ_{YZ}	Top	386	303	309	405	319	288	355	342	314
	Bottom	724	677	498	759	492	445	640	542	540
8 inch AC										

ε_X	Top	302	279	288	336	325	285	515	321	287
	Bottom	151	161	213	92	118	115	138	142	98
ε_Y	Top	716	816	715	810	762	805	1203	896	723
	Bottom	58	55	38	44	46	46	78	36	57
ε_Z	Top	1052	808	662	847	809	770	1405	747	875
	Bottom	286	261	214	240	191	178	293	214	139
γ_{XZ}	Top	602	522	620	467	503	497	790	522	552
	Bottom	416	351	335	303	304	276	362	315	408
γ_{YZ}	Top	700	606	378	451	456	484	901	559	604
	Bottom	145	175	192	138	125	120	198	169	184
Maximum		1052	857	789	847	809	805	1405	896	875
Average		497	447	379	435	377	375	511	419	421

In the most cases, the strain responses in different directions at top and bottom of pavements decreased with increasing speed, which was reasonable for viscoelasticity analysis. In some cases, the trend of strain with increasing speed was meandering instead of downward, which was understandable because of the big standard deviation with only three data point for each test series. However, strains at the top of pavements sometimes increased with increasing speed. It made no sense for static viscoelasticity analysis. But if the dynamic passing process was taken into consideration, it was understandable because it was easier for vehicle to make additional bumping impact to pavement with higher speed. Such case usually happened at the top of pavement especially for 120 psi, because when tire inflation pressure was high, it was more likely for the tires bumping in the experimental process.

For the heavy loaded trucks on highways, the resulting responses in both 4 inch and 8 inch pavements were combined together to evaluate the effect of tire inflation pressure

for specific tire configuration. Compare the maximum and average strain response with different tire inflation pressures in

Table 17, the tire inflation pressure 100 psi induced least strain response for Michelin wide-base tire and was most protective for the pavements. Strain responses for other tire configurations under different tire inflation pressures were also adjusted, and summarized in Appendix C.

Based on the comparison between different tire inflation pressures for the four tire configurations, suitable inflation pressure can be derived for each tire configuration.

In general, the best inflation pressure was 70 psi for GoodYear wide-base tire; 70/100 psi for GoodYear dual tire; 100 psi for Michelin wide-base tire and 120 psi for Michelin dual tire. Compared to width of tire footprint listed in Table 3, higher inflation pressure was suitable for the tire group which has wider contact area. For example, the total width of GoodYear dual tires was 18 inch, which was the largest among the four tire configurations, and its suitable inflation was 120 psi, which was larger than other tire models.

Discussions and Conclusion

As seen in Figure 72, temperature and speed adjustment changed the magnitude of strain responses because of the viscoelasticity properties of asphalt concrete. The proportion of adjustment was smaller for series with the same tire inflation pressure because these series were closer in time with less temperature turbulence. Comparing strain responses before and after temperature and speed adjustments, the distribution of strain responses

via tire inflation pressure was more likely to be changed by temperature and speed adjustment than the distribution via speed.

Offset distance adjustment changed strain responses more obviously than the temperature and speed adjustment, not only on magnitude, but also the distributions over speed and tire inflation pressure. It was because the strain response for passing tire in transverse plane of pavements changed intensely with the offset distance. The comparison in Figure 69 ensures the necessity of offset distance adjustment for a fair comparison of strain measurements in experiments.

For the strain response after temperature, speed and offset distance adjustments, increasing speed leaded to smaller responses in most cases, which make sense in viscoelasticity analysis. Due to the limited number of runs in each test series, standard deviation was big, and the decreasing trend of strain via speed was disrupted in some cases. At the same time, for the series with high speed (55 mph), the bumping impact to pavements might be exacerbated, and the strains were more likely to increase with speed than those with low speed.

The effect of tire inflation pressure to strain response in pavement was more complicated than that of speed. The relationship between tire inflation pressure and adjusted strain responses changed with speed, direction of strain, location of the sensor, and probably the configuration of the tire. Based on general comparison of the maximum and average strain response, 100 psi was recommended for heavy loaded truck from the perspective of pavement protection.

Different tire configurations leaded to different distribution of strain responses in pavements. By comparison in Figure 71, GoodYear wide-base tire A brought biggest tensile strain at the bottom of 4 inch and 8 inch pavements, and biggest vertical strain throughout 8 inch pavement compared to other 3 kinds of tires. Since tensile strain at the bottom of pavement is an indicator of fatigue cracking and vertical strain is correlated to the rutting depth of pavements, GoodYear wide-base tire might brought more fatigue cracking damage to 4 and 8 inch pavement, and both GoodYear wide-base tire A and Michelin Dual Tire D had a high potential to bring more rutting damage to 8 inch pavement.

Comparing the shear strain present in Figure 71 (d-e), GoodYear wide-base tire A induced extremely high shear strain at the bottom of 8 inch pavement; GoodYear wide-base tire A and Michelin dual tire D brought higher shear strain at the top of 4 inch pavement compared to tire B and C.

The structure of pavement also played an important role in the distribution of strain response in pavements. Compared to 8 inch asphalt concrete pavement, 4 inch asphalt concrete layer was more flexible, and stand more horizontal tension and less vertical compression in mechanical analysis, as shown in Figure 71 (a-c). From the point view of limiting fatigue damage, 8 inch asphalt concrete decreased the tension strain at the bottom by 50 percent compared to 4 inch AC surface layer, and the tensile strain at the bottom of 8 inch AC was so limited that the pavement was almost perpetual to fatigue cracking for all the tires except for GoodYear wide-base tire.

Distress Prediction

Various distresses of pavements are the main target of pavement management and maintenance, and the original intent of collecting the data was to predict pavement performance under different loading and environmental conditions. Main pavement distresses include fatigue cracking and rutting depth, which are going to be discussed in this chapter.

Distress Models

The cumulative damage concept has been widely used to predict fatigue cracking. It is generally agreed that the allowable number of load repetition is related to the tensile strain at the bottom of the asphalt layer. The major difference in the various design methods is the transfer functions that relate the tensile strains in asphalt concrete layer to the allowable number of load repetitions. The fatigue cracking model by Illinois Department of Transportation [67] was used to justify the fatigue damage of each tire to the experimental section.

$$N_f = 5 \times 10^{-6}(\epsilon_t)^{-3.0} \qquad \text{Eq. (68)}$$

where ϵ_t is the tensile strain at the bottom of asphalt concrete layer and N_f is the allowable number of load repetitions.

Permanent deformation is another factor for flexible pavement design and maintenance. “With the increase in traffic load and tire pressure, most of the permanent deformation occurs in the upper layer rather than in the subgrade” [67]. Since only the strain in the

asphalt concrete layer is measured in the experiment, then the rutting depth calculated in the paper is only for the asphalt concrete layer of the experimental sections.

The Mechanistic-Empirical Pavement Design Guide (MEPDG) rutting models along were used to estimate the rutting depth of experimental sections.

$$\frac{\varepsilon_p}{\varepsilon_r} = k_1 \cdot 10^{-3.4488} T^{1.5606} N^{0.479244} \quad \text{Eq.(69)}$$

where ε_p is the accumulated plastic strain after N repetition of load; ε_r is the resilient strain of the asphalt material; N is the number of load repetitions; T is the pavement temperature (°F); and k_1 is the function of total asphalt layer(s) thickness and depth to computational point, to correct for the variable confining pressures that occur at different depths.

$$k_1 = (C_1 + C_2 \cdot depth) \cdot 0.328196^{depth} \quad \text{Eq.(70)}$$

$$C_1 = -0.1039 \cdot H_{ac}^2 + 2.4868 \cdot H_{ac} - 17.342 \quad \text{Eq.(71)}$$

$$C_2 = 0.0172 \cdot H_{ac}^2 - 1.7331 \cdot H_{ac} + 27.428 \quad \text{Eq.(72)}$$

Then the overall permanent deformation was then computed as sum of permanent deformation for each individual sub-layer.

$$PD = \sum_{1}^{NS} \varepsilon_p^i \cdot h^i \quad \text{Eq.(73)}$$

Where PD is the permanent deformation of pavement; NS is the number of sub-layers; ε_p^i is the total plastic strain in i^{th} sub-layer; and h_i is the thickness of the i^{th} sub-layer.

Distress Prediction with Different Tire Configurations

Known the strain distribution for different tire configurations and pavement structures, the corresponding distresses can be predicted with existing models. It is more practical and understandable to compare different tire configurations with predicted distress than with strain responses.

The allowable number of load repetition was computed for each tire on both 4 inch and 8 inch sections, and summarized in Figure 73.

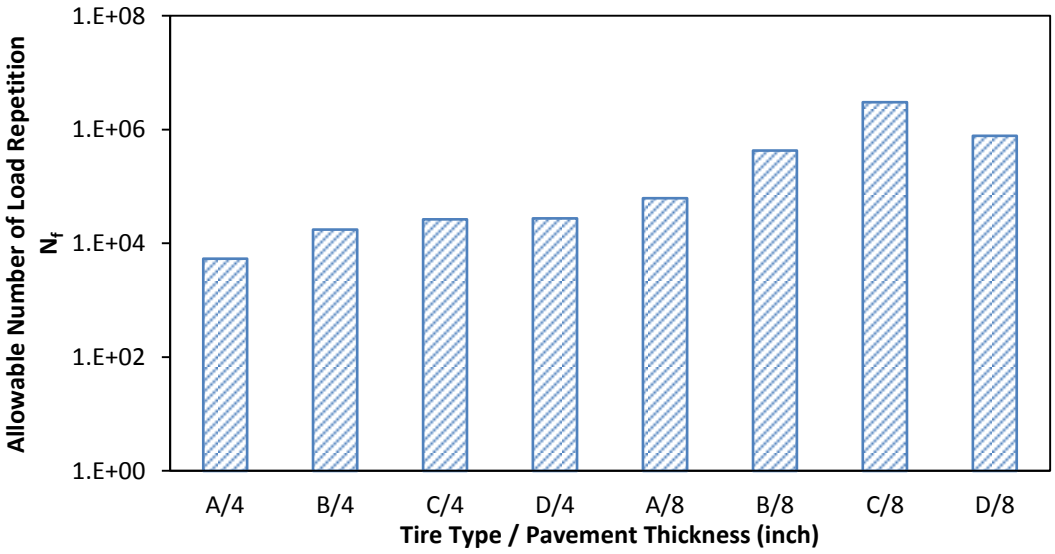

Figure 73: Allowable load repetition N_f via tire configurations and layer thickness

100 psi, 25 mph

Based on the comparison in Figure 73, the fatigue cracking life of 8 inch pavement was increased 10 times of 4 inch pavement. The allowable repetition number of Michelin wide-base tire C was the highest, which meant that the wide-base tire C reduced fatigue damage to pavement instead of inducing additional fatigue damage than dual tires.

The allowable repetition number of tire A was 24% of the average number of GoodYear dual tire B and Michelin dual tire D in 4 inch pavement, and only 10% of the average number of the dual tire B and D in 8 inch pavement. It meant that using wide-base tire A induced approximately 4 times fatigue cracking damage to the 4 inch section and 10 times to the 8 inch section. In another word, the fatigue cracking life of 4 inch pavement was reduced to 25% of original life, and the fatigue life of 8 inch pavement was reduced to 10% of original life after using tire A instead of B and D

The repetition number of load was set as 10^6, and the vertical strain ε_Z and the shear strain $\gamma^{(Y)}$ were chosen to represent the resilient strain separately. The calculated rutting depths brought by four kinds of tires to pavement sections are plotted in Figure 74.

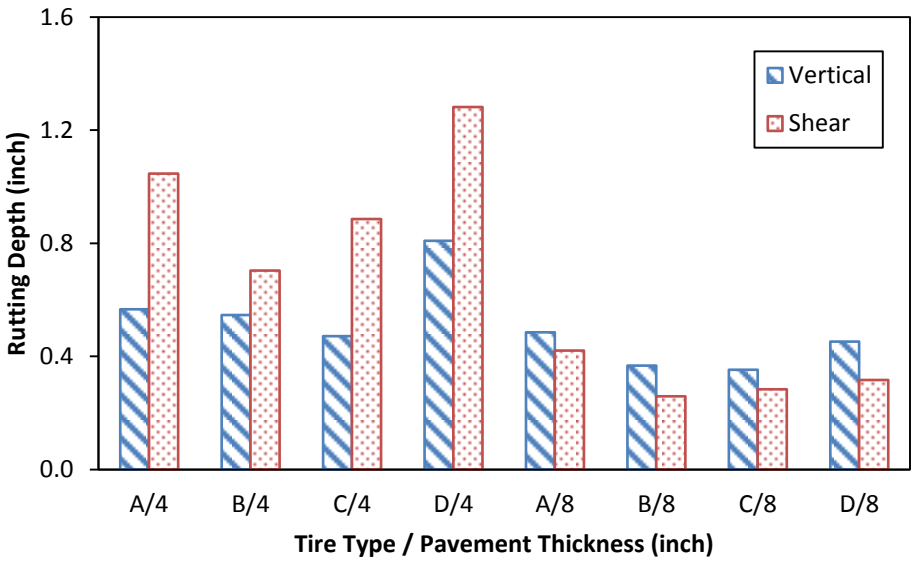

Figure 74: Rutting depths via tire configurations and layer thickness

Based on the comparison in Figure 74, the 4 inch pavement present more sensitivity to transverse profile distortion than the 8 inch pavement although the vertical and shear strain in 4 inch pavement were lower than those in 8 inch pavement (as shown in Figure

71). It was because the vertical and shear strain in 4 inch pavement was not transferred to sub-layer as wide as 8 inch pavement, and the strain concentration aggravated the rutting distress in pavement.

Wide-base tire A induced 20% more rutting depth than the average of dual tires B and D in 8 inch pavement. Tire D produced a high rutting depth in 4 inch pavement, probably because it applied high pressure at the edge of tire, and aggravated the stress concentration in pavement.

Distress Prediction with Different Tire Inflation Pressures

Based on the adjusted strain response for different tire inflation pressures, pavement distress damage can be predicted with existing models, and the effect of tire inflation pressure can be evaluated.

The allowable number of load repetition induced by various test series was computed for the four involved tire configurations, and compared in Figure 75.

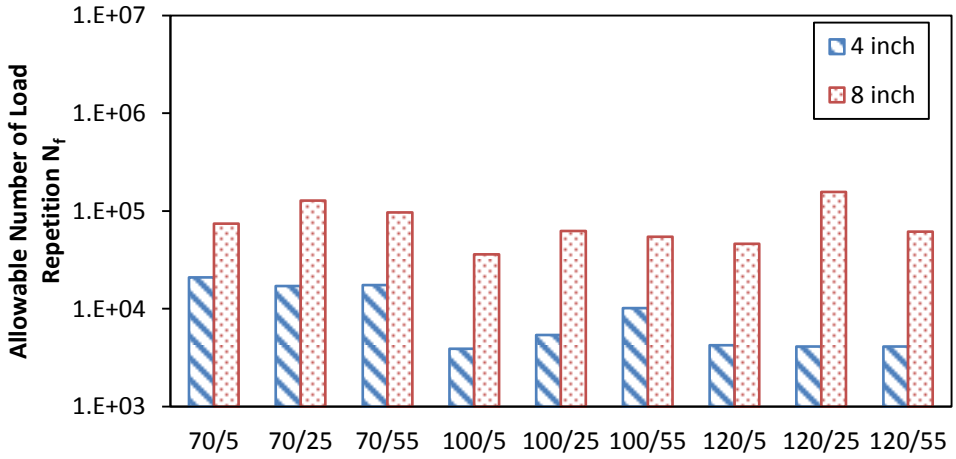

(a) Tire A: GoodYear Wide-base

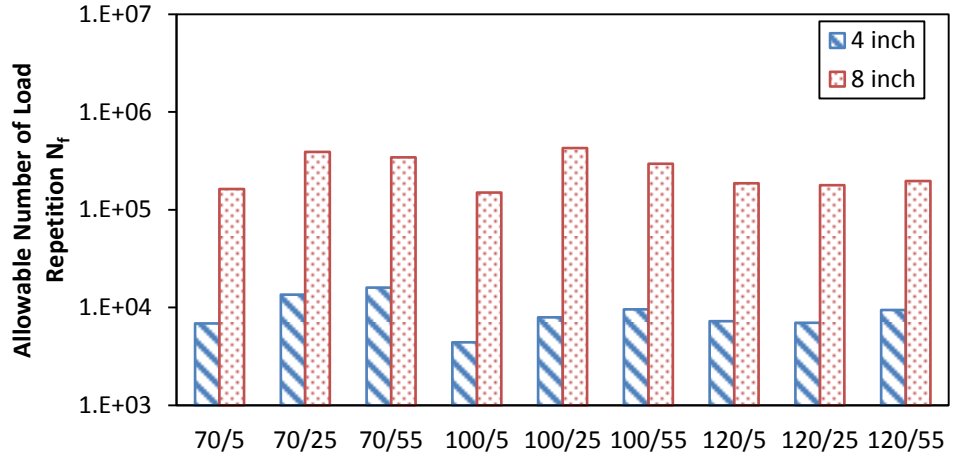

(b) Tire B: GoodYear Dual

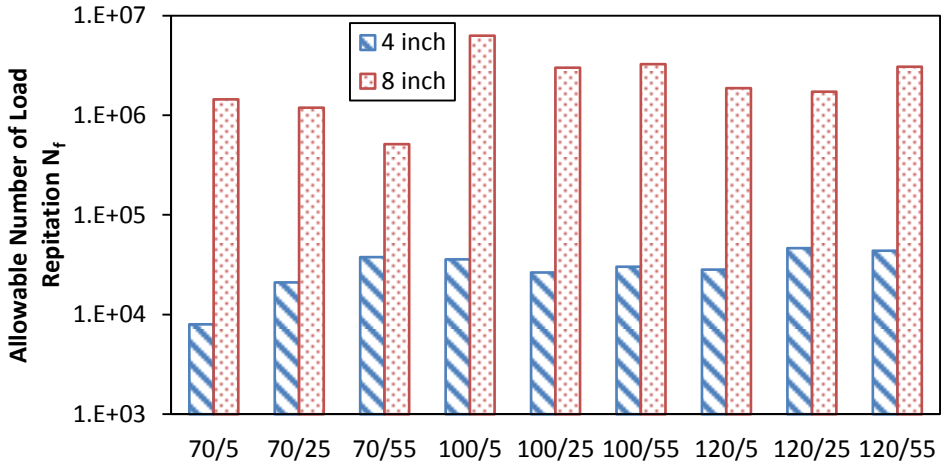

(c) Tire C: Michelin Wide-base

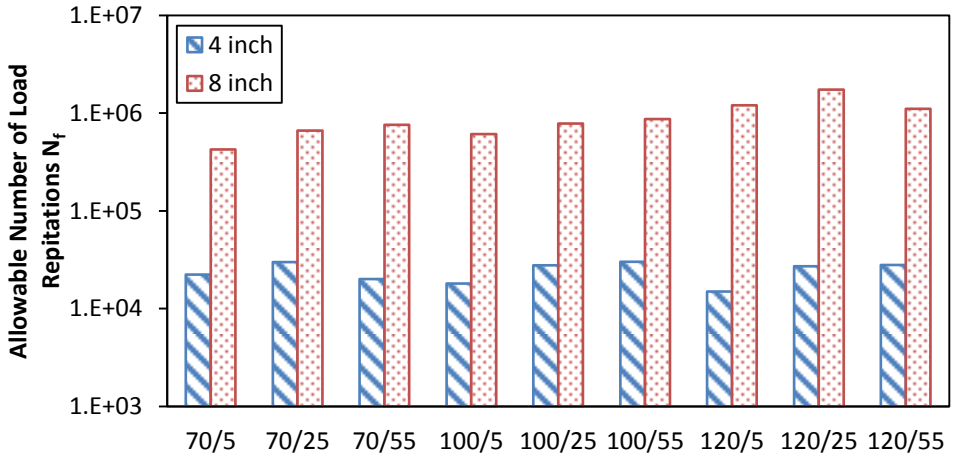

(d) Tire D: Michelin Dual

Figure 75: Allowable load repetition N_f via test series

From the comparison in Figure 75, the allowable number of load repetition can be affected obviously by speed. For heavy loaded trucks in motion, although speed is changing all the time, the most common speed should be around 55 mph because the heavy loaded trucks spend most time on highway instead of local roads. Only considering 55 mph for each tire configurations, Michelin wide-base tire C and dual tire D induced less fatigue cracking damage with higher inflation pressure 120 or 100 psi than the low pressure 70 psi; GoodYear wide-base tire A and dual tire B induce less fatigue cracking damage with lower inflation pressure 70 psi than 100 or 120 psi.

The same rutting model was used on the adjusted vertical and shear strains of different test series for each tire configuration, and the results are listed in Figure 76.

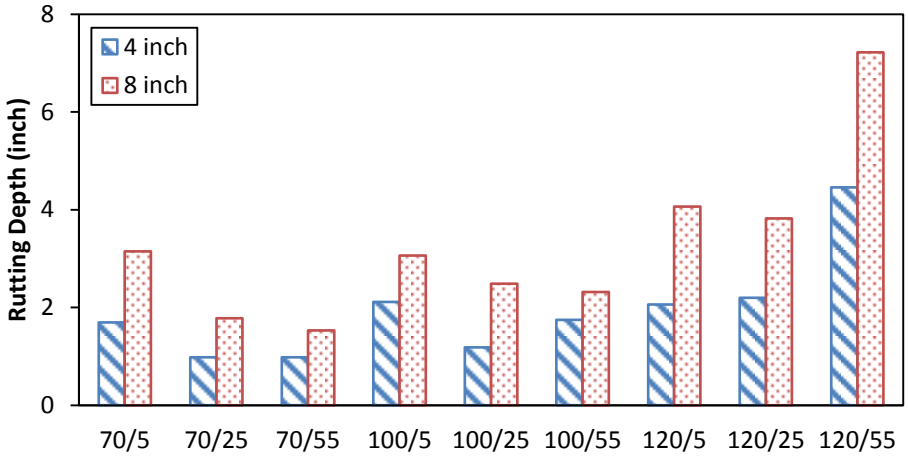

(a) Tire A: GoodYear Wide-base

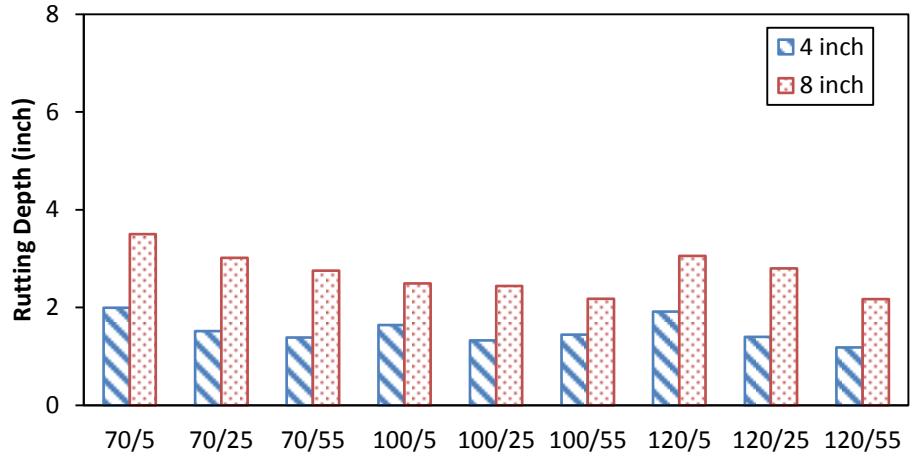

(b) Tire B: GoodYear Dual

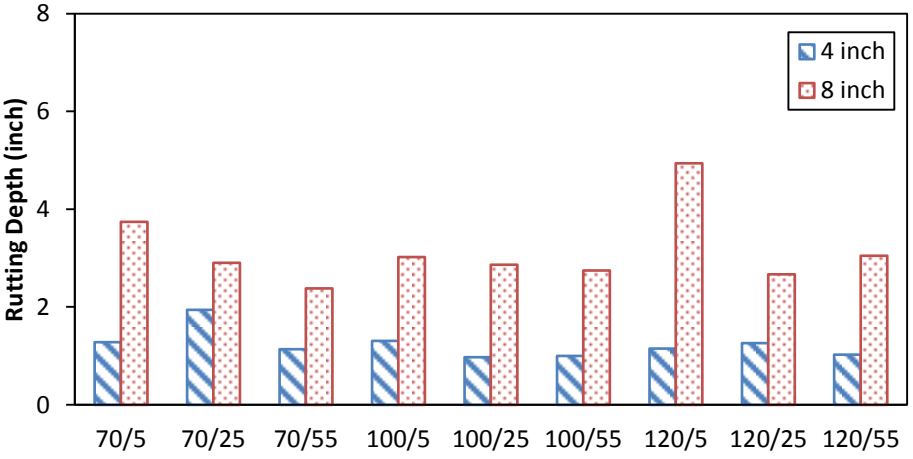

(c) Tire C: Michelin Wide-base

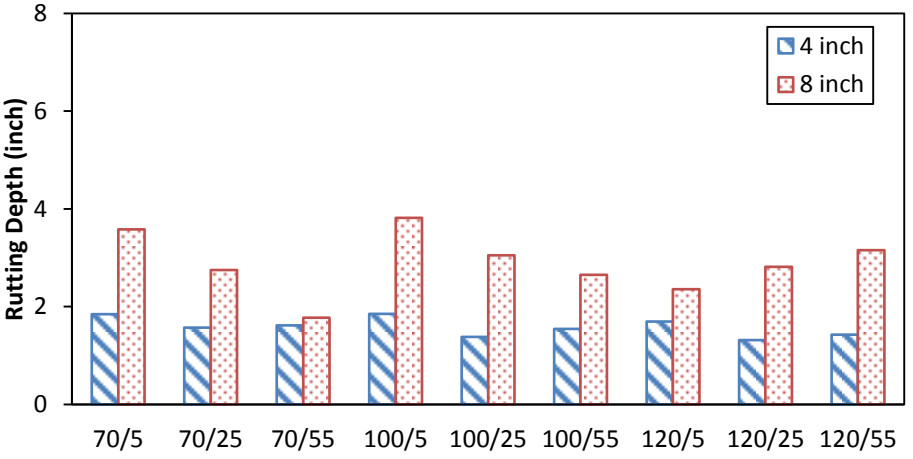

(d) Tire D: Michelin Dual

Figure 76: Rutting depths via test series

As seen in Figure 76, for most tire configurations, high tire inflation pressure (120 psi) brought the most rutting damage. It was probably because the bigger vertical pressure induced bigger vertical stress in pavement which could aggravate the rutting damage of pavements. At the same time, wide-base tires present more sensitivity to tire inflation pressure. In another word, wide-base tire might bring more rutting damage to pavements once tire inflation pressure was increased. In the perspective of reducing rutting damage, 100 psi was the best inflation pressure for most of the tire configurations in the experiment.

Discussions and Conclusion

In the prediction of fatigue cracking, GoodYear wide-base tire A induced much more damage to both 4 inch and 8 inch pavements than other 3 kinds of tires, and the allowable repetition number was much lower. As a result, if GoodYear wide-base tire A was used instead of dual tires B and D, the fatigue life of pavements would be reduced to a quarter or even less of their original expectation. In contrary, the new wide-base tire, Michelin MXDA, present a close and even better fatigue life than GoodYear and Michelin dual tires, which made its pavement friendly characteristics more convincing.

At the same time, 8 inch pavement exhibited a much better fatigue cracking resistance compared to 4 inch pavement. The fatigue life of 8 inch pavement was more than 10 times of 4 inch pavement, and could be treated as perpetual for tires B, C and D.

GoodYear wide-base tire A brought more rutting damage than GoodYear dual tire B and Michelin wide-base tire C. However, Michelin dual tire D also induced a high rutting

depth, extremely in 4 inch pavement. The possible reason was the high pressure at the edge of the tire D.

Although the vertical and shear strains in 8 inch pavement were higher than those in 4 inch pavement, the resulted rutting depth was much lower instead. It was probably because that the strain responses were transferred to a wider area throughout the thickness and the rutting damage was limited a lot.

Based on the quantification of fatigue cracking and rutting depth for different tires in 4 inch and 8 inch pavements, 8 inch pavement was much more resistant to the damage brought by different tire configuration. As a result, if these varying tire configurations were expected in the traffic mix, then state highway agencies may increase the thickness of pavement to mitigate the additional distress.

CONCLUSIONS

All the research in transportation area can be categorized into traffic and infrastructure, and monitoring function is important for both of the two groups. Traffic monitoring system focuses on obtaining various information of traffic flow, and pavement monitoring system tracks the health status of pavements for better infrastructure management.

This dissertation builds up an integrated transportation monitoring system which can monitor the health status of pavements and the statistics of traffic flow simultaneously. All the work done for this dissertation is concluded in this chapter, including the overview of the research, the contributions to civil engineering, and the recommendation to future research.

Summaries

Sensing devices in pavements include electrical sensors and optic fiber sensors. And the sensing technologies in past decades were summarized and discussed. At the same time, various pavement research facilities (test roads) were also talked about as integrals of pavement research and engineering. Related monitoring systems, including bridge monitoring system, Weigh-in-Motion system and traffic classification system and some comprehensive monitoring systems, were also discussed in dissertation.

Results from two comprehensive field experiments were used in the dissertation. In Ohio experiment, testing vehicle was driven on Ohio experimental road with different

combinations of tire configuration, inflation pressure and speed. In Virginia experiment, testing runs were made with various vehicles under changing temperatures to study the effect of temperature on pavement mechanical responses. The strain responses in pavements were used to develop back-calculation method of vehicles' speed, configuration, weight and other parameters.

Various pavement responses were checked and recognized, and many sensors were found out of service just after several months of installation. Various responses distribution in pavements were compared and summarized for better understanding of pavement response to traffic loading.

For pavement health monitoring purpose, various sensors were displayed in the direction of the traffic to measure various mechanical responses at the same position. The ratio between collected vertical stress and longitudinal strain responses were used to represent and back calculate the modulus of the asphalt concrete layer. The MEPDG damage model of fatigue cracking and rutting were rewritten into the damage brought by single axle pass, and used for the damage prediction of pavement health status monitoring. The pavement health monitoring system was designed based on periodic testing runs and continuous monitoring. Pavement modulus could be obtained from periodic testing as the index of pavement structure strength. The distress induced by each passing vehicle could be accumulated in continuous streaming for pavement distress prediction.

For traffic monitoring purpose, the analysis of pavement responses were categorized into temporal distribution and spatial distribution based on the domain of data sets. Traffic volume, speed, number of axles and distance between axles were calculated based on the

pavement response distributions in time domain. The other parameters, such as wandering position, the distance between wheels, tire width and axle weight, were calculated from the strain response distributions on different offset distances. For the data analysis in spatial distribution, strain gauges were arranged across the transverse plane of the experimental section. A new Gaussian function based model was developed to characterize the strain distribution in pavements accurately, and the parameters of the model were set to match various loading conditions.

The effect of temperature and speed was studied based on viscoelasticity theory. The data points of strain response from the runs with similar temperature and speed were shifted by the back-calculated offset distance and integrated together. The effect of temperature and speed was revealed in numerical simulation and experimental measurements. However, the relationship between temperature and experimental measurement was not as clear as in the previous tests because many sensors were damaged from the harsh environment and the excessive traffic load.

In the Ohio experiments, test runs were finished with temperature, speed and wandering position variations, all of which might induce the variation of collected strain response. It was the biggest challenge in the comparisons of strain responses by different tire configurations to eliminate the effects of the uncontrollable environmental and loading conditions. A method was developed to adjust the strain measurement to a universal temperature, fixed speed and zero offset distance based on Laboratory viscoelastic tests and numerical simulation. The adjusted strain responses were compared to study the effect of tire configurations and inflation pressure. MEPDG damage models and shear

rutting model were used to calculate the damage brought by different tire configurations and inflation pressure based on the actual strain measurements.

Contributions and Findings

During the research process of this dissertation, the main contributions were summarized as the follows.

(1) The monitoring functions of traffic and infrastructure were combined together, and the concept of integrated transportation monitoring system was provided.

(2) The developments of sensing technologies and integrated monitoring system were summarized and tabulated.

(3) A comprehensive sensing network was designed with commercial sensing devices (strain gauge, load cell, thermo couple and moisture sensor) and data logger.

(4) Various involved sensors were checked and studied for their installation procedures and resistance to environment and traffic loads. CTL vertical strain gauges were proved to be very vulnerable and damaged very soon after the installation.

(5) Finite element method based software ABAQUS was used and proved to be effective in the simulation of loading process on pavements.

(6) MEPDG damage models of fatigue cracking and rutting were modified into the damage induced by each single axle pass and can be used to predict pavement distress from actual responses.

(7) A new distribution model based on Gaussian function was developed to characterize the distribution of horizontal longitudinal strain response in pavements.

(8) A complete pavement health monitoring system was designed based on structure and distresses monitoring, obtained separately from periodic testing and continuous streaming.

(9) A complete vehicle back-calculation method was developed to estimate various parameters of passing vehicles, including traffic counts, axle and wheel distribution, speed, wandering position, tire width and axle load.

(10) A novel integration method was developed to integrate data points from the runs of similar temperature and speed together. The integrated distribution of pavement response has more data points and can describe the strain distribution much more accurately.

(11) Temperature and vehicle's speed were both proved to have considerable effect on pavement's strain response, but the impact of temperature was much higher than that of speed.

(12) Another method for consistent comparison of variable field sensor data was developed. It was demonstrated that variation in field measurement was due to uncontrollable environmental and loading factors, which may be accounted for by using laboratory test and numerical simulation based corrections.

(13) The damage brought by different tire configuration and inflation pressure was studied, and newer version of wide-base tire with a width of 495 mm was proved to be road-friendly.

Conclusions

In this dissertation, the prototype of a transportation monitoring system was developed. This system can track the health status of the pavement and function for traffic statistics, weigh-in-motion and traffic classification purposes simultaneously in real-time monitoring. The feasibility of integrated transportation monitoring system was proved and its various advantages suggested high potential of being realized in the future.

The data analysis method used in the research, such as temperature adjustment, offset distance adjustment, shift method to integrate data points of testing runs were proved to be useful in the back-calculation and other data analysis of pavement. Gaussian model was provided in this research, which can simulate the spatial distribution of strain response in pavement, and was very valuable in the analysis of pavement responses and traffic back-calculation. The effect of temperature, vehicles' speed, tire configuration and inflation pressure was studied for the complement of the transportation monitoring system in future.

Recommendations

For the research with similar topics in the future, the recommendation were made as follows:

(1) More attention should be paid to the installation of CTL vertical strain gauges. At the same time, the installed depth of sensing devices should be revised to avoid excessive traffic load on sensors.

(2) Sensing network can be improved with more sensors installed to characterize the distribution of pavement responses.

(3) The instrumentation of the experimental section can be improved with more professional plan and enough preparation time.

(4) More test runs can be made to verify the efficiency of the monitoring system with various environmental and loading conditions.

(5) The anisotropy of pavement material, and the sizing of installed sensing devices might be good topics for this research field in future.

In conclusion, the ruggedness of integrated sensor systems, improved installation procedures, and integrated data-collection and analysis packaging will continue to be the major focus of research, and economic and feasible monitoring systems for large scope deployment will be become feasible in the next decade.

APPENDIX

Appendix A: Specifications of Devices

A1.Specifications of V-Link 2.4 GHz Wireless Voltage Node

Input channels	Up to 8 input channels: 4 full differential (350 Ω resistance or higher); 3 single ended input (0~3 volts maximum) 1 internal temperature sensor
Temperature sensor	-40°C to 70°C range, typical accuracy ±2°C (at 25°C)
Anti-aliasing filter bandwidth	-3 dB cutoff at 250 Hz
Measurement Accuracy	±0.1% full scale typical
Resolution	1 bit: 0.024%
DC bridge excitation	+3 volts DC at 50 mA maximum
Programmable gain	Software programmable for differential input channels from 210 to 4844
Programmable offset	Software programmable
Analog to digital (A/D) converter	Successive approximation type, 12 bit resolution
Data storage capacity	2 megabytes (approximately 1,000,000 data points)
Data logging mode	Log up to 1,000,000 data points (from 100 to 65,500 samples or continuous) at 32 Hz to 2048 Hz
Sensor event driven trigger	Commence datalogging when threshold exceeded
Real-time steaming mode	Transmit real time data from node to PC – rate depends on number of active channels: 1 channel – 4 KHz; 2 channel – 2 KHz; 3 channel – 1.33 KHz; 4 channel – 1 KHz; 5 channel – 800 Hz; 6 channel – 666 Hz; 7 channel – 570 Hz; 8 channel – 500 Hz;
Low duty-cycle mode	Supports multiple nodes on single RF channel from 1 sample per hour to 250 Hz
Synchronization between nodes	Datalogging ±4 µsec ±50 ppm, LDC mode time stamped at PC
Sample rate stability	±25 ppm for sample rates > 1 Hz, ±10% for sample rates ≤ 1 Hz
Wireless shunt calibration	Channels 1 to 4, internal shunt calibration resistor 499 KΩ
Radio frequency (RF) transceiver carrier	2.4 GHz direct sequence spread spectrum, license free worldwide (2.405 to 2.480 GHz) – 16 channels, radiated power 0 dBm (1 mW)
RF data packet standard	IEEE 802.15.4, open communication architecture
RF data downloading	8 minutes to download full memory
Range for bi-directional RF link	70 m line-of-sight, up to 300 m with optional high gain antenna
Internal Li-lon battery	3.7 volt lithium ion rechargeable battery, 740 mAh capacity; customer may supply external power from 3.2 to 9 volts
Power consumption	V-Link node only: real-time straming – 25 mA; datalogging – 25 mA; sleeping – 0.1 Ma. External sensors: 350 Ω strain gauge – 8 mA; 1000 Ω strain gauge – 3 mA.
Operating temperature	-20 °C to +60 °C with standard internal battery and enclosure, extended

	temperature range optional with custom battery and enclosure, -40 °C to +85 °C for electronics only
Maximum acceleration limit	500 g standard
Dimensions	88 mm × 72 mm × 26 mm (enclosure without antenna). 76 mm × 65 mm × 12 mm (circuit board assembly only).
Weight	97 g (with enclosure), 15 g (circuit board assembly only).
Enclosure material	ABS plastic
Software	Node Commander Windows XP/Vista compatible
Compatible base stations	USB, RS-232, Analog, WSDA

A2. Specifications of CTL Asphalt Strain Gage

General Specifications	
Bridge Completion	Full bridge
Gage Resistance	350 Ohm
Excitation	Up to 10 volts
Output	≈2 mV/V @ 1500 μstrain
Grid Area	0.133 cm^2
Gage Area	1.22 cm^2
Fatigue Life	<105 repetitions @ +/- 2000 μstrain
Modulus	340,000 psi
Cell Material	Black 6/6 nylon
Coating	Two-part polysulfide liquid polymer encapsulated in silicone with butyl rubber outer core
Quality Assurance	
Water Submersion	1 ft for 24 hours at 24 °C (75 °F)
Temperature	-34 °C (-30 °F) TO 204 °C (400 °F)
Lead Wire	30 ft of 22 AWG braided shield four wire

A3. Specifications of Load Cell KDE-PA

Capacity	2 MPa
Rated output	0.5 mV/V (1000 μstrain)
Non-linearity	2%RO
Temperature range	-20 ~ +60 °C
Input/Output resistance	350 Ohm
Recommended exciting voltage	Less than 3V
Allowable exciting voltage	10 V
Weight	160 g

A4. Specifications of Thermo Couple TMTSS-125-6

Length	6 inch
Sheath diameters	0.125 inch
Junction Type	Grounded
Wires	40 inch Teflon-Coated lead wires
Upper Temperature	260°C (500 °F)

A5. Specifications of Moisture Sensor VH400

Power consumption	<7 mA
Supply Voltage	3.3 V to 20 VDC
Output Impedance	100 K Ohm
Operational temperature	-40 °C to 85 °C
Frequency of operation	80 MHz
Accuracy	2%
Output	0~3 V related moisture content
Sensitive to volume	No
Sensitive to salt	No
Shell Color	Red

Appendix B: Statement of Asphalt Concrete in Virginia Route 114

TL-127 MC (11-05)

VIRGINIA DEPARTMENT OF TRANSPORTATION

MATERIALS DIVISION

STATEMENT OF ASPHALT CONCRETE OR CENTRAL-MIX AGGREGATE JOB-MIX FORMULA

Submit to the District Administrator, Virginia department of Transportation. Approval must be received by ther contractor from the Materials Division before work is begun. This job-mix design is approved for all projects of the Department for the type of mix and the calendar year shown below.

Contractor Design Mix No. 2007 201116 Design Lab No. S-1

Date 7/13/2011 Job Mix ID No. Calendar Yr. 2011 TSR Test No. 0%

Type Mix / Size Aggregate SM-9.5D HR

Producer Name & Plant Location Adams Construction Co. - Rockydale II Phone (540) 774-4419

Materials				Kind		Source
Approval Phase	A	B *	C			
Aggregate	49.0%	49.0%		#8	AMPHIBOLE	ROCKYDALE QUARRY - GLADE HILL, VA
Aggregate						
Aggregate						
Screening	8.0%	8.0%		#10	LIMESTONE	ROCKYDALE QUARRY - ROANOKE, VA
Sand	18.0%	18.0%		NATURAL		CASTLE SAND CO. - NEW CASTLE, VA
RAP	25.0%	25.0%		PROCESSED		ADAMS CONSTRUCTION CO. - ROANOKE, VA
Lime						
Asphalt Cement	5.5%	5.5%		PG 64-22		ASSOCIATED ASPHALT - ROANOKE, VA
Additives	0.5%	0.5%		ADHERE HP+		ARR-MAZ PRODUCTS - WINTER HAVEN, FL

Job-Mix Sieves	Total % Passing		Tolerance % + or -	Acceptance Range Average of 8 Tests		End of Year Average	Design/Spec. Range
	Lab JMF	Producton JMF					
Approval Phase	A	B *		A	B	C	
1/2"	100.0	100.0	0	100.0	100		100
3/8"	94.0	97.0	2.8	91.2 - 96.8	94.2 - 99.8		90 - 100
#4	55.0	58.0	2.8	52.2 - 57.8	55.2 - 60.8		80 MAX
#8	40.0	40.0	2.8	37.2 - 42.8	37.2 - 42.8		38 - 67
#200	5.7	5.7	0.7	5.0 - 6.4	5.0 - 6.4		2 - 10
Asphalt (%)	5.5	5.5	0.21	5.29 - 5.71	5.29 - 5.71		

Lay Down Temperatures	270 - 350	°F (°C)	Muffle Furnace Correction Factor:	0.04
			Field Correction Factor (Gse - Gsb):	0.019
Lab Compaction Temperatures	295 - 300	°F (°C)	Pill Weight:	5150
			SMA Mixes	
Producer Technician's Certification Number	M. WALLACE		VCA drc:	
			Gca:	

MATERIALS DIVISION USE ONLY 0

Calculated Mix PG Grade: 71.87

Remarks	VMA =	16.6	VFA =	78.7	F/A =	1.08	PERM	<80	Gse =	2.898	Pbe =	5.28
Nominal Max. Size Aggregate			Application Rates:		Min.		lb/yd^2			Max.		lb/yd^2
Mix Properties at the Job-Mix Asphalt Content:			Compacted Unit Weight	158.7	lb.ft^3		VTM:	3.5	Gmm:	2.635		

Checked By: Jeff Henderson *Potential VFA & F/A problems*

Approved tenetatively subject to the production of material meeting all other applicable requirements of the specification.

* Note: Part B "Production JMF" and corresponding Materials percentages will be filled out by the DME upon receipt of the additional requirements of the HMA producer within the first lot under Section 502.01(b).

Copies:		Approvals				
	State Materials Engineer		☑	Part A:	D. Clyde Landreth	Date: 7/14/2011
	District Materials Engineer		☑	Part B:	D. Clyde Landreth	Date: 10/26/2011
	Project Inspector		☐	Part C:		Date:
	Sub-Contractor and/or Producer					

Appendix C: Strains Induced by All the Test Series

			Tire Inflation Pressure (psi) / Speed (mph)								
			70/5	**70/25**	**70/55**	**100/5**	**100/25**	**100/55**	**120/5**	**120/25**	**120/55**
A. GOODYEAR WIDE-BASE TIRE	4 inch AC										
	ε_X	Top	250	173	260	148	224	537	345	619	731
		Bottom	620	663	658	1087	975	789	1056	1068	1068
	ε_Y	Top	84	61	75	126	75	205	137	232	302
		Bottom	267	220	247	289	313	274	377	283	373
	ε_Z	Top	362	152	143	386	183	333	366	423	1031
		Bottom	349	333	351	581	400	446	593	556	737
	γ_{XZ}	Top	618	339	450	539	681	979	790	1021	1726
		Bottom	346	406	341	699	394	210	1515	720	887
	γ_{YZ}	Top	96	101	80	154	193	179	195	323	336
		Bottom	691	523	692	760	321	386	904	851	1037
	8 inch AC										
	ε_X	Top	158	109	108	179	217	277	288	365	415
		Bottom	407	339	372	518	431	451	476	317	433
	ε_Y	Top	259	261	253	527	515	434	600	579	845
		Bottom	138	150	149	316	266	156	281	210	198
	ε_Z	Top	626	318	254	586	468	456	865	900	1750
		Bottom	968	747	750	1068	911	736	927	377	447
	γ_{XZ}	Top	245	148	196	314	252	328	536	671	987
		Bottom	808	675	781	1115	942	855	1001	667	832
	γ_{YZ}	Top	311	184	203	408	212	230	571	511	827
		Bottom	217	213	311	284	293	260	451	308	340
	Maximum		968	747	781	1115	975	979	1515	1068	1750
	Average		391	306	334	504	413	426	614	550	765
B. G	4 inch AC										
	ε_X	Top	690	785	783	360	672	693	650	688	702
		Bottom	898	716	679	1044	857	805	883	894	809

GOODYEAR DUAL TIRE	ε_Y	Top	283	260	231	165	203	227	218	185	200
		Bottom	218	139	164	263	233	159	277	208	140
	ε_Z	Top	328	243	188	207	169	230	301	217	120
		Bottom	781	610	634	791	633	584	785	577	636
	γ_{XZ}	Top	725	491	508	531	473	508	527	466	441
		Bottom	545	331	339	309	282	376	1027	499	232
	γ_{YZ}	Top	261	258	237	179	207	199	271	195	188
		Bottom	822	477	461	993	560	461	818	414	571
	8 inch AC										
	ε_X	Top	227	200	194	201	199	194	206	203	208
		Bottom	313	234	244	322	227	257	299	304	294
	ε_Y	Top	884	616	919	737	611	351	2003	1307	414
		Bottom	106	79	56	123	95	77	109	94	69
	ε_Z	Top	864	758	690	575	603	533	748	694	533
		Bottom	648	482	450	692	440	435	605	507	416
	γ_{XZ}	Top	433	370	380	355	275	292	391	310	288
		Bottom	589	480	463	613	459	489	578	529	500
	γ_{YZ}	Top	625	511	600	457	395	465	530	489	440
		Bottom	363	255	208	396	273	237	391	367	220
	Maximum		898	785	919	1044	857	805	2003	1307	809
	Average		530	415	421	466	393	379	581	457	371
C. MICHELIN WI	4 inch AC										
	ε_X	Top	916	857	789	682	579	722	556	616	795
		Bottom	856	620	509	518	573	548	562	476	485
	ε_Y	Top	387	375	304	315	341	268	217	319	529
		Bottom	162	144	155	126	138	169	132	197	180
	ε_Z	Top	277	528	262	272	208	213	234	316	210
		Bottom	373	356	301	399	287	297	361	283	318
	γ_{XZ}	Top	861	699	596	845	488	624	736	647	711
		Bottom	568	352	206	653	476	340	544	712	406
	γ_{YZ}	Top	386	303	309	405	319	288	355	342	314

D E - B A S E T I R E		Bottom	724	677	498	759	492	445	640	542	540
						8 inch AC					
	ε_X	Top	302	279	288	336	325	285	515	321	287
		Bottom	151	161	213	92	118	115	138	142	98
	ε_Y	Top	716	816	715	810	762	805	1203	896	723
		Bottom	58	55	38	44	46	46	78	36	57
	ε_Z	Top	1052	808	662	847	809	770	1405	747	875
		Bottom	286	261	214	240	191	178	293	214	139
	γ_{XZ}	Top	602	522	620	467	503	497	790	522	552
		Bottom	416	351	335	303	304	276	362	315	408
	γ_{YZ}	Top	700	606	378	451	456	484	901	559	604
		Bottom	145	175	192	138	125	120	198	169	184
	Maximum		1052	857	789	847	809	805	1405	896	875
	Average		497	447	379	435	377	375	511	419	421
						4 inch AC					
D. M I C H E L I N D U A L T I R E	ε_X	Top	899	720	703	986	690	669	823	798	751
		Bottom	608	551	629	652	565	549	693	569	563
	ε_Y	Top	297	250	273	298	235	195	282	202	265
		Bottom	372	258	188	284	228	202	145	194	223
	ε_Z	Top	494	435	355	442	370	389	359	283	341
		Bottom	559	446	638	664	419	516	697	532	507
	γ_{XZ}	Top	916	891	836	982	796	746	890	780	816
		Bottom	833	534	560	830	582	496	894	503	385
	γ_{YZ}	Top	406	318	325	456	372	289	465	452	308
		Bottom	621	529	663	976	526	474	981	420	486
						8 inch AC					
	ε_X	Top	237	222	160	304	257	224	233	277	235
		Bottom	228	196	188	201	186	179	161	142	166
	ε_Y	Top	727	680	448	764	714	602	641	912	628
		Bottom	55	75	62	79	54	56	75	51	47
	ε_Z	Top	1153	876	570	1253	986	863	758	915	1036

γ_{XZ}	Bottom	376	336	199	289	298	238	257	254	239
	Top	565	532	356	606	543	457	528	463	494
	Bottom	436	361	302	474	356	352	373	312	346
γ_{YZ}	Top	756	620	384	750	604	643	594	638	625
	Bottom	223	216	182	230	220	187	191	172	148
Maximum		1153	891	836	1253	986	863	981	915	1036
Average		538	452	401	576	450	416	502	443	430

Appendix D: Viscoelastic Tests of Asphalt Concrete in Virginia Route 114

D1. Dynamic Modulus of Test Sample

11-1021D

Temp. (°F)	Mixture $\|E^*\|$ (psi)						Shift factor
	0.1 Hz	0.5 Hz	1 Hz	5 Hz	10 Hz	25 Hz	log $\alpha(T)$
14	2215886	2511183	2637269	2911245	3024423	3153603	4.548
40	984999	1291851	1448492	1803640	1961200	2157387	2.005
70	285773	432454	537365	795193	929982	1115292	0.000
100	77508	128175	182893	321017	400836	517446	-1.502
130	30642	41374	62042	114667	143529	190870	-2.803

11-1024D

Temp. (°F)	Mixture $\|E^*\|$ (psi)						Shift factor
	0.1 Hz	0.5 Hz	1 Hz	5 Hz	10 Hz	25 Hz	log $\alpha(T)$
14	1947059	2282893	2413862	2734178	2867830	3385760	3.994
40	904648	1218897	1376988	1738035	1896223	2099372	1.978
70	247918	386719	488390	729250	857173	1031460	0.000
100	60679	96687	139947	249175	313378	402431	-1.692
130	27422	33576	46828	85393	106685	133749	-3.062

11-1028D

Temp. (°F)	Mixture $\|E^*\|$ (psi)						Shift factor
	0.1 Hz	0.5 Hz	1 Hz	5 Hz	10 Hz	25 Hz	log $\alpha(T)$

14	2156469	2530231	2693689	3060392	3216114	3664909	4.278
40	874771	1199849	1368044	1762740	1941475	2171746	2.027
70	216445	346543	452228	700629	832178	1020098	0.000
100	74815	109876	145188	252752	317004	415968	-1.501
130	31289	39832	54742	97833	121919	156969	-2.813

D2. Phase Angle of Test Sample

11-1021D

Frequency (Hz)	Temperature (°C)				
	-10	4	20	38	54
25	4.347	9.223	18.807	28.327	35.900
10	4.847	10.487	20.843	28.740	30.893
5	5.243	11.540	22.510	29.283	29.777
1	6.217	14.247	25.703	29.860	28.917
0.5	6.723	15.767	27.663	31.757	27.260
0.1	8.173	18.987	28.513	27.740	27.740

11-1024D

Frequency (Hz)	Temperature (°C)				
	-10	4	20	38	54
25	3.460	9.873	19.717	30.550	33.117
10	5.690	11.233	21.630	29.540	27.110
5	6.245	12.317	23.167	29.430	25.187
1	7.600	15.030	26.057	29.153	22.307
0.5	8.085	16.600	28.250	30.763	23.033
0.1	10.040	19.800	28.770	26.180	26.180

11-1028D

Frequency (Hz)	Temperature (°C)				
	-10	4	20	38	54
25	6.250	10.817	21.423	29.550	31.017
10	6.200	12.207	23.377	28.583	25.637
5	6.700	13.387	24.890	28.137	23.603

1	7.897	16.313	27.713	26.817	21.157
0.5	8.530	17.977	30.410	26.660	20.990
0.1	10.220	21.330	30.293	22.073	22.073

D3. RAP Content

Mix ID	RAP amount (%)	Asphalt content by weight (%)	NMAS (mm)
10-1021D	25	5.2	9.5
10-1024D	25	5.82	9.5
10-1028D	26	5.71	9.5

REFERENCES

1. Potter, J.F., H.C. Mayhew, and A.P. Mayo, *Instrumentation of the full scale experiment on A1 trunk road at Conington, Huntingdonshire*, in *Report LR296, Road Research Lab /UK/*1969. p. 41.
2. Sebaaly, P.E., et al., *Instrumentation for flexible pavements - field performance of selected sensors*, 1991, Federal Highway Administration: Washington D.C.
3. Sebaaly, P.E., N. Tabatabaee, and B. Kulakowski, *Evaluation of the Hall-effect sensor for pavement instrumentation.* Journal of Testing and Evaluation, 1995. **23**(3): p. 189-195.
4. Hipley, P. *Caltrans' current state-of-practice*. in *Instrumental Diagnostics of Seismic Response of Bridges and Dams*. 2001. University of California, Berkeley: Pacific Earthquake Engineering Research Center.
5. Huff, R., C. Berthelot, and B. Daku, *Continuous primary dynamic pavement response system using piezoelectric axle sensors.* Canadian Journal of Civil Engineering, 2005. **32**(1): p. 260-269.
6. Xue, W. and E. Weaver, *Pavement shear strain response to dual and wide-base tires.* Transportation Research Record, 2011(2225): p. 155-164.
7. Lajnef, N., et al., *Toward an integrated smart sensing system and data interpretation techniques for pavement fatigue monitoring.* Computer-Aided Civil and Infrastructure Engineering, 2011. **26**(7): p. 513-523.
8. Malla, R., A. Sen, and N. Garrick, *A special fiber optic sensor for measuring wheel loads of vehicles on highways.* Sensors, 2008. **8**(4): p. 2551-2568.
9. Li, H.N., D.S. Li, and G. Song, *Recent applications of fiber optic sensors to health monitoring in civil engineering.* Engineering Structures, 2004. **26**: p. 1647-1657.
10. Navarrete, M.C. and E. Bernabeu, *Fibre-optic weigh-in-motion sensor.* Sensors and Actuators A: Physical, 1994. **41**(1–3): p. 110-113.
11. Signore, J.M. and J.R. Roesler, *Using fiber-optic sensing techniques to monitor behavior of transportation materials.* Transportation Research Record: Journal of the Transportation Research Board, 1995. **1478**: p. 37-43.
12. Wang, J.N. and J.L. Tang, *Using fiber Bragg grating sensors to monitor pavement structures.* Transportation Research Record: Journal of the Transportation Research Board, 2005. **1913**: p. 165-176.
13. Zhou, Z., et al., *Optical fiber Bragg grating sensor assembly for 3D strain monitoring and its case study in highway pavement.* Mechanical Systems and Signal Processing, 2012. **28**: p. 36-49.

14. Timm, D.H., A.L. Priest, and T.V. McEwen, *Design and instrumentation of the structural pavement experiment at the NCAT test track*, 2004, National Center for Asphalt Technology, Auburn University.

15. Rollings, R.S. and D.W. Pittman, *Field instrumentation and performance monitoring of rigid pavements.* Journal of Transportation Engineering, 1992. **118**(3): p. 361-370.

16. Timm, D.H. and A.L. Priest, *Dynamic pavement response data collection and processing at the NCAT test track*, 2004, National Center for Asphalt Technology, Auburn University. .

17. Lukanen, E.O., *Load testing of instrumented pavement sections*, 2005, Minnesota Department of Transportation, Research Services Section.

18. Al-Qadi, I.L., et al., *The Virginia Smart Road: the impact of pavement instrumentation on understanding pavement performance.* The Journal of APPT, 2004. **73**: p. 427-465.

19. Loulizi, A., I. Al-Qadi, and M. Elseifi, *Difference between in situ flexible pavement measured and calculated stresses and strains.* Journal of Transportation Engineering, 2006. **132**(7): p. 574-579.

20. Lynch, J.P., et al., *Performance monitoring of the Geumdang Bridge using a dense network of high-resolution wireless sensors.* Smart Materials and Structures, 2006. **15**(6): p. 1561-1575.

21. Ko, J. and Y. Ni, *Structural health monitoring and intelligent vibration control of cable-supported bridges: Research and application.* KSCE Journal of Civil Engineering, 2003. **7**(6): p. 701-716.

22. Barrish, J.R.A., *Instrumented monitoring of the Commodore Barry Bridge.* Proceedings of SPIE, the international society for optical engineering, 2000. **3995**(1): p. 112-126.

23. Kim, J. and J.P. Lynch, *Experimental analysis of vehicle–bridge interaction using a wireless monitoring system and a two-stage system identification technique.* Mechanical Systems and Signal Processing, 2012. **28**(0): p. 3-19.

24. Norman, O. and R. Hopkins. *Weighing vehicles in motion*. in *31st Annual Meeting of Highway Research Board*. 1952. Washington D.C.: Highway Research Board.

25. George, Y. and C. Antoniou, *Integration of weigh-in-motion technologies in road infrastructure management.* ITE Journal, 2005. **75**(1): p. 39-43.

26. Lu, Q., et al., *Truck traffic analysis using weigh-in-motion (WIM) data in California*, 2002, University of California, Berkeley, Institute of Transportation Studies, Pavement Research Center.

27. Cheng, L., H. Zhang, and Q. Li, *Design of a capacitive flexible weighing sensor for vehicle WIM system.* Sensors, 2007. **7**: p. 1530-1544.

28. *Standard specification for highway weigh-in-motion (WIM) systems with user requirements and test methods*, in *ASTM Standard E1318-09*1994, American Society for Testing and Materials.

29. Stamatinos, G. and J. Wyatt, *Evaluation of IRD-WIM-5000 - a Canadian weigh-in-motion system.* Canadian journal of civil engineering, 1990. **17**(4): p. 514-520.

30. Yuan, S., et al., *Optic fiber-based dynamic pressure sensor for WIM system.* Sensors and Actuators A: Physical, 2005. **120**(1): p. 53-58.

31. Teral, S.R., et al., *Fiber optic weigh-in-motion sensor: correlation between modeling and practical characterization.* Proceedings of SPIE, the international society for optical engineering, 1996. **2718**(1): p. 417-426.

32. Muhs, J.D., et al., *Results of a portable fiber optic weigh-in-motion system.* Proceedings of SPIE - International Society for Optical Engineering 1991. **1584**: p. 374-386.

33. Kenneth W. Tobin, J. and J.D. Muhs, *Algorithm for a novel fiber optic weigh-in-motion sensor system.* Proceedings of SPIE - International Society for Optical Engineering 1991. **1589**: p. 102-109.

34. Cheng, L., H. Zhang, and Q. Li, *Design of a Capacitive Flexible Weighing Sensor for Vehicle WIM System.* Sensors, 2007. **7**(8): p. 1530-1544.

35. Zhang, W., C. Suo, and Q. Wang, *A novel sensor system for measuring wheel loads of vehicles on highways.* Sensors, 2008. **8**: p. 7671-7689.

36. Nash, D.D., *Alice: automatic length indication and classification equipment. an equipment for automatically classifying vehicles and measuring their speed.* Traffic Engineering and Control, 1976. **17**(12): p. 496-501.

37. Benekohal, R. and M. Girianna, *Technologies for truck classification and methodologies for estimating truck vehicle miles traveled.* Transportation Research Record: Journal of the Transportation Research Board, 2003. **1855**(-1): p. 1-13.

38. Gajda, J., et al. *A vehicle classification based on inductive loop detectors*. in *Instrumentation and Measurement Technology Conference, IMTC 2001. Proceedings of the 18th IEEE*. 2001.

39. Coifman, B. and S. Kim, *Speed estimation and length based vehicle classification from freeway single-loop detectors.* Transportation Research Part C: Emerging Technologies, 2009. **17**(4): p. 349-364.

40. Coifman, B., *Improved velocity estimation using single loop detectors.* Transportation Research Part A: Policy and Practice, 2001. **35**(10): p. 863-880.

41. Kwon, J., P. Varaiya, and A. Skabardonis, *Estimation of truck traffic volume from single loop detectors with lane-to-lane speed correlation.* Transportation Research Record: Journal of the Transportation Research Board, 2003. **1856**(-1): p. 106-117.

42. Yinhai, W. and N.L. Nihan, *Dynamic estimation of freeway large-truck volumes based on single-loop measurements.* Journal of Intelligent Transportation Systems, 2004. **8**(3): p. 133-141.

43. Udd, E., et al., *Fiber grating systems for traffic monitoring.* Proceedings of SPIE - International Society for Optical Engineering 2001. **4337**: p. 510-516.

44. Kunzler, M., et al., *Fiber grating traffic monitoring systems.* Proceedings of SPIE - International Society for Optical Engineering 2002. **4696**: p. 238-243.

45. Kunzler, M., et al., *Traffic monitoring using fiber optic grating sensors on the I-84 freeway and future uses in WIM.* Proceedings of SPIE - International Society for Optical Engineering 2003. **5278**: p. 122-127.

46. Kunzler, M., et al., *Second-generation fiber grating traffic monitoring systems on the I-84 freeway.* Proceedings of SPIE - International Society for Optical Engineering 2003. **5054**: p. 230-239.

47. Zhang, W., Q. Wang, and C. Suo, *A novel vehicle classification using embedded strain gauge sensors.* Sensors, 2008. **8**(11): p. 6952-6971.

48. *Traffic monitoring handbook*, 2007, Florida Department of Transportation.

49. Cosentino, P.J., W. von Eckroth, and B.G. Grossman, *Analysis of fiber optic traffic sensors in flexible pavements.* Journal of Transportation Engineering-Asce, 2003. **129**(5): p. 549-557.

50. Cosentino, P.J. and B.G. Grossman, *Development and implementation of a fiber optic vehicle detection and counter system: final report*, in *FDOT Final Report*1996, Florida Institute of Technology, Melbourne, Florida.

51. Cosentino, P.J. and B.G. Grossman, *Development of fiber optic dynamic weight-in-motion system*, in *FDOT Final Report*1997, Florida Institute of Technology, Melbourne, Florida.

52. Cosentino, P.J. and B.G. Grossman, *Optimization and implementation of fiber optic sensors for traffic classification and weigh-in-motion systems, phase 3*, in *FDOT Final Report*2000, Florida Institute of Technology, Melbourne, Florida.

53. Morgan, G.C.J.P., L. D.; Arraigada, M.; Partl, M. N.; Muff, R. , *In situ monitoring of pavement stresses on the A1 in Switzerland.* Journal of Testing and Evaluation 2008. **36**(4): p. 1-9.

54. Wenjing, X., W. Dong, and W. Linbing, *A review and perspective about pavement monitoring.* International Journal of Pavement Research & Technology, 2012. **5**(5): p. 295-302.

55. Goncalves, F.P., J.A.P. Ceratti, and A.V.D. Bica, *The use of embedded stress cells for monitoring pavement performance.* Geotechnical testing journal, 2003. **26**(4): p. 363-372.

56. Wong, K.-y., C.K. Lau, and A.R. Flint, *Planning and implementation of the structural health monitoring system for cable-supported bridges in Hong Kong*. Proceedings of SPIE - International Society for Optical Engineering 2000. **3995**: p. 266-275.

57. Straser, E.G. and A.S. Kiremidjian, *A modular, wireless damage monitoring system for structures*, in *Technical Report* 1998, John A. Blume Earthquake Engineering Center: Stanford, CA.

58. Lynch, J.P., et al., *Design and performance validation of a wireless sensing unit for structural monitoring applications.* Structural Engineering and Mechanics, 2004. **17**: p. 393-408.

59. Bonaquist, R., *An Assessment of the Increased Damaged Potential of Wide-Base Single Tires*, in *Proceedings of the 7th International Conference on Asphalt Pavements, Design and Performance*1992. p. 16.

60. Elseifi, M.A., et al., *Quantification of pavement damage caused by dual and wide-base tires*, in *Pavement Management; Monitoring, Evaluation, and Data Storage; and Accelerated Testing 2005*2005, Transportation Research Board Natl Research Council: Washington. p. 125-135.

61. Greene, J., et al., *Impact of wide-base single tires on pavement damage.* Transportation Research Record: Journal of the Transportation Research Board, 2010. **2155**(-1): p. 82-90.

62. Weaver, E.J. *Minutes*. in *International Workshop on the Use of Wide-Base Single Tires*. 2008. Turner-Fairbank Highway Research Center: Federal Highway Administration.

63. Routhier, B. *Wide-base tires - fleet experiences*. in *International Workshop on the Use of Wide-Base Tires*. 2007. Turner Fairbank Highway Research Center: Federal Highway Administration.

64. Bynum, C. *Improving heavy truck fuel consumption*. in *international workshop on the use of wide-base tires*. 2007. Turner-Fairbank Highway Research Center: Federal Highway Administration.

65. Goel, A. and A. Das, *Nondestructive testing of asphalt pavements for structural condition evaluation: a state of the art.* Nondestructive Testing and Evaluation, 2008. **23**(2): p. 121-140.

66. *Mechanistic-empirical design of new & rehabilitated pavement structures*, NCHRP.

67. Huang, Y.H., *Pavement analysis and design*2004, Upper Saddle River.

68. Gibson, N., et al., *Viscoelastic, Viscoplastic, and Damage Modeling of Asphalt Concrete in Unconfined Compression.* Transportation Research Record: Journal of the Transportation Research Board, 2003. **1860**(-1): p. 3-15.

69. Park, S.W. and R.A. Schapery, *Methods of interconversion between linear viscoelastic material functions. Part I—a numerical method based on Prony series.* International Journal of Solids and Structures, 1999. **36**(11): p. 1653-1675.

70. Sime, M. and S.C. Ashmore, *Tire pavement interface pressure patterns*, 1999, Federal Highway Administration.

71. Prowell, B.D., et al., *Validating the Fatigue endurance limits for hot mixed ashphalt.* National Cooperative Highway Research Program report, 2010.